Journal of
Photopolymer

Science and Technology
Volume 36   Number 3

2023

Information for Contributors

Submit Manuscripts to the SPST Homepage (Journal --> Submission of Papers --> Editorial Manager). Submission is a representation that the manuscript has not been published previously elsewhere. The manuscript should be accompanied by a statement transferring copyright from the authors (or their employers-whoever holds the copyright) to the Society of Photopolymer Science and Technology. A suitable form for copyright transfer is available from the SPST Homepage. This written transfer of copyright, which previously was assumed to be implicit in the act of submitting a manuscript, is necessary under the Japan copyright law. Further information may be obtained from the "Manual for Manuscript Writing" at the SPST Homepage.

Proofs and All Correspondence: Concerning papers in the process of publication should be addressed to the Editorial Office.

Manuscript Preparation: All the papers submitted are reproduced electronically as they were. For this reason, the manuscripts should be prepared according to the Manual for Manuscript Writings shown at the SPST Homepage.

Subscription Price (Airmail Postage included):
¥12,000 (in Japan), US$ 150.00 (for Foreign)

Subscriptions, renewals, and address changes should be addressed to the Editorial Office. For the address changes, please send both old and new addresses and, if possible, include a mailing label from the wrapper of recent issue. Requests from subscribers for missing journal issues will be honored without charge only if received within six months of the issue's actual date of publication; otherwise, the issue may be purchased at the single-copy price.

Publication Charge (Reprint Order): To support a part of the cost of publication of journal pages, the author's institution is requested to pay a page charge of ¥3,000 per page (with a one-page minimum) and an article charge of ¥12,000 per article. The page charge (if honored) entitles the author to 50 free reprints. For Errata the minimum page charge is ¥3,000, with no articles charge and no free reprints.

The cover designed by M. Tsuda and M. Morishita

Aggregation of Au Colloids using Surface Acoustic Waves

**Shunya Saegusa[1][*], Tsunemasa Saiki[2], Sho Amano[3], Takao Fukuoka[1],
Yukako Takizawa[2] , Masatoshi Takahashi[1], Keisuke Yoshiki[4], Kaito Fujitani[1],
Koji Sumitomo[4], Yuichi Utsumi[1] , and Akinobu Yamaguchi[1]**

[1] *Institute of Advanced Industrial Science and Technology, University of Hyogo,*
3-1-2, Koto, Kamigori, Ako-gun, Hyogo, 678-1205, JAPAN
[2] *Hyogo Prefectural Institute of Industrial Technology,*
3-1-12, Yukihira, Suma, Kobe, Hyogo, 654-0037, JAPAN
[3] *Department of Mechanical Engineering Graduate School of Engineering,*
The University of Tokyo,
7-3-1, Hongo, Bunkyo-ku, Tokyo, 113-0033, Japan
[4] *Graduate School of Engineering, University of Hyogo,*
2167 Shosha, Himeji, Hyogo 671-2201, JAPAN

* saesae54@lasti.u-hyogo.ac.jp

For the implementation of SERS in microfluidic devices, we propose a rotor structure using SAW as a simple aggregation mechanism. In this study, 45 nm gold nanoparticles were agglomerated in a rotor and evaluated. It was found that the aggregate size increased with increasing supply energy, indicating that this mechanism contributes to aggregate formation. SERS measurements using this mechanism were also successfully performed.
Keywords: Photopolymer resist, SERS, SAW, μ-TAS, Aggregation

1. Introduction

The μ-TAS (Micro Total Analysis System), which is based on microfabrication technology, is a resource-saving, short-time, highly sensitive, and highly efficient analysis system. This system is expected to be applied in various fields such as medicine, environment, chemistry, biochemistry, and food [1-4]. However, the fluorescence and absorption methods used as detection methods in μ-TAS have several problems. First, the fluorescence method requires pretreatment by immobilizing and labeling a fluorescent substance on an antibody, which is indispensable for measurement. In addition, the output signal lacks stability due to a decrease in fluorescence intensity caused by light fading. In the absorption method, detection sensitivity depends on the optical path length through the sample, which makes high-sensitivity detection difficult for microchemical analysis systems used in a limited microscopic space. This also causes the problem of limiting the shape and size of devices and chips due to the optical path length. Furthermore, since these two detection methods are generally performed in the visible light range, where noise is very large, even if a signal with very large light intensity is obtained, the S/N ratio, which is the contrast ratio between signal and noise, becomes small. And, the signal is disturbed by the large noise effect. To solve these problems, we focused on SERS (Surface Enhanced Raman Scattering) [5-16]. SERS is an analytical method that does not require antibody labeling or device limitations due to optical path length. This method is a combination of Raman spectroscopy and Localized Surface Plasmon Resonance (LSPR), in which the Raman scattering intensity of molecules adsorbed on noble metal nanostructures is significantly enhanced, and the signal is obtained. This method is expected to simplify the system because the measurement is performed by simply adsorbing a molecule on the noble metal nanostructure and irradiating it with a near-infrared laser. Ultimately, this method will enable measurement at the level of a single molecule, making it possible to fabricate ultra-sensitive sensors with higher sensitivity than those currently available. However, the fabrication of

noble metal nanostructures is essential for detection by SERS. To fabricate this structure in a channel, an aggregation mechanism of gold nanoparticles is necessary, and we need to prepare a complex channel structure [8.9]. In this study, we focused on surface acoustic waves (SAW) [17] as a method of agglomeration. SAW is a sound wave that propagates by concentrating its energy only on the surface of an elastic body [17-26]. This is a power source that can be easily integrated into devices because it is generated by applying an alternating current to IDT (interdigital transducer) [18] fabricated on a piezoelectric substrate such as $LiNbO_3$ [19] or $LiTaO_3$. In the past, our research group has fabricated and evaluated a SAW actuator [21-26] that drives a continuous fluid by SAW and a micro rotating mixer that applies SAW actuators [26]. On the other hand, we focused on shear fields as a method of agglomeration. Simulations in previous papers have shown that particles in a shear field tend to form chain-like structures [27,28]. We considered that agglomeration occurs when this chain-like structure grows. In this paper, we report on the evaluation of the agglomeration process by the shear field generated by SAW and the result of its application to SERS, as shown in Fig. 1.
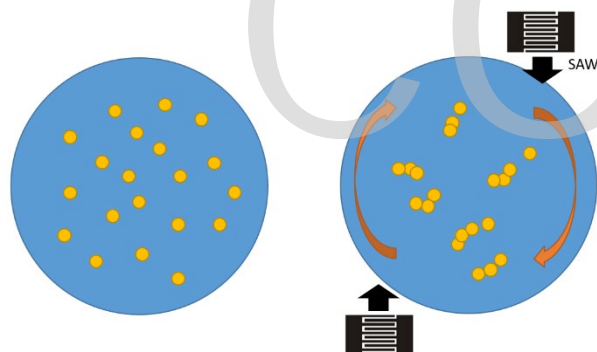
Fig. 1. Conceptual diagram of particle transfer

2. Experimental

2.1. Fabrication of SAW devices

A small liquid rotor was fabricated using SAW as a device to fabricate aggregate structures.

First, we fabricate IDT by lift-off method. In this method, we sputtered 20 nm of Cr and 1000 nm of Al on a $LiNbO_3$ substrate by DC sputtering. After sputtering, positive photopolymer resist (OFPR-800 from Tokyo Ohka Kogyo Co., Ltd.) is applied on the substrate and UV exposure is performed to transfer the IDT pattern drawn on a glass mask. Then, based on this pattern, IDTs were fabricated on the substrate by etching Al and Cr. Finally, an absorbing material was applied to reduce reflections from the edge surfaces [25]. The conceptual diagram of the fabricated device is shown in Fig. 2.

In this liquid rotor, the liquid is driven by SAW from two directions to produce rotation. The top of the IDT and the liquid reservoir are open to allow for SAW damping and to prevent the rotation of the liquid.
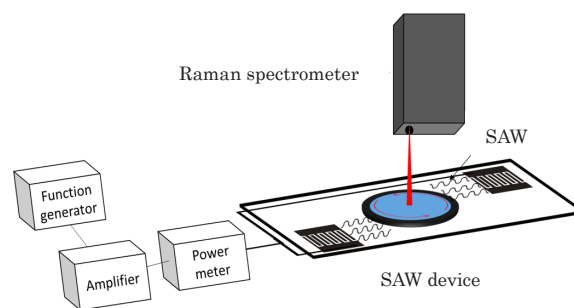
Fig. 2. Setup of SAW experiment

The experimental flow is as follows. First, a high-frequency voltage is generated by a signal generator (Tektronix AFG3252) and amplified by an amplifier (R&K ALM00110-2840FM). The amplified voltage is then applied to the IDT to generate SAW. To prevent damage to the piezoelectric substrate due to heat generation, a burst voltage waveform was used as the high-frequency voltage applied to the IDT. This waveform consists of a burst period followed by k cycles of sine waves and a pause period. By using such a burst waveform, the energy supplied to the IDT can be reduced to kf_b/f_{ib} compared to a continuous waveform. Here, fb is the frequency of the sine wave during the burst period, which is determined by the IDT shape and other factors. Also, f_i is the reciprocal of the burst interval from one sine wave to the next. In the experiment, instead of measuring the amplitude V_{pp} of the applied voltage to the IDT, the power P is measured by an RF power meter (Rohde & Schwarz NRP-291). In this experiment, we adjusted supply energy E_s by f_b.

2.2. Analysis of aggregation process by SAW

During the rotation of the rotor by SAW, a shear field is generated in the rotor. Simulations in previous papers have shown that particles form beads in the shear field [27, 28]. To verify the aggregation process, gold colloids (Tanaka Kikinzoku Kogyo K.K.) with a particle size of 45 nm were rotated in the rotor for 1 min. We measured the change in particle size of the gold nanoparticles using dynamic light scattering (DLS). The liquid samples rotated were 3.0 µl of pure water, 3.0 µL of 1M NaCl solution as a flocculant, and 44 µL of Au colloid. Since the sample obtained in one experiment is very small, the DLS measurements were made by mixing 150 µl of sample from three experiments and 300 µl of pure water.

2.3. Application to SERS

The SERS activity was confirmed by actually aggregating Au nanoparticles in the prepared liquid rotor. A sample of 1 mM 4,4'-Bipyridine (4bpy) was prepared. SERS measurements were performed by mixing 3.0 µl of the sample, 3.0 µL of 1M NaCl solution, and 44 µL of Au colloid with a SAW rotor. The SERS spectrum of 4bpy and the interactions corresponding to the peaks are shown in Fig.3. The RAMAN instrument used was the spectrometer module (C13560, Hamamatsu photonics).
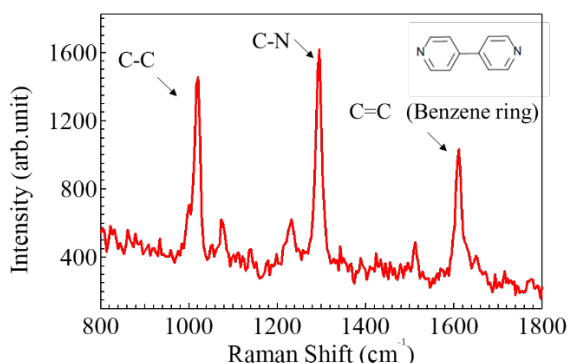
Fig. 3. The SERS spectrum of 4bpy

3. Results and discussion

3.1 Aggregation process by SAW

Fig. 4 shows the particle size after mixing for 1 minute, measured using DLS (dynamic light scattering). The gold nanoparticles before agglomeration have a diameter of 45 nm, indicating that agglomeration occurs under all conditions. The particle size also increases as the supply energy E_s increases. The curve fitted by this equation is the black line in Fig. 4. The frequency of particle collisions increases in the shear field due to SAW, which accelerates particle agglomeration.
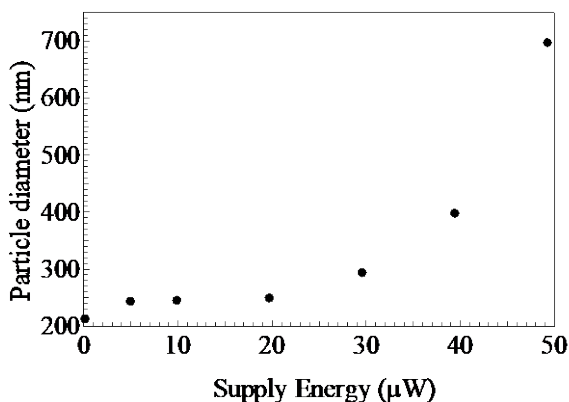
Fig. 4. Relationship between supply energy and diameter of Au agglomerates.

3.2. SERS Analysis

The SERS intensity increases with rotation, as shown in Fig. 5. However, there was no stability in the measurement results. The graphs in Fig. 6 show the change in Raman peak intensity around 1250 cm^{-1} when 49.2 µW of supply energy was applied.

This may be because high supply energy and high density of Au nanoparticles cause rapid agglomeration, resulting in variation in the size of
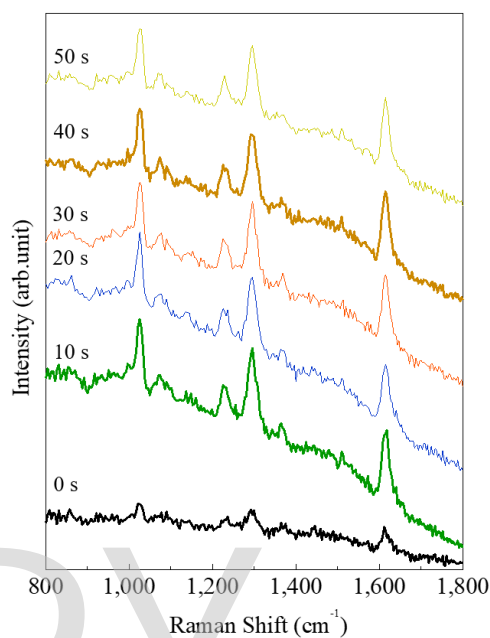
Fig. 5. Change in Raman spectra of 4bpy (E_s = 49.2 µW)
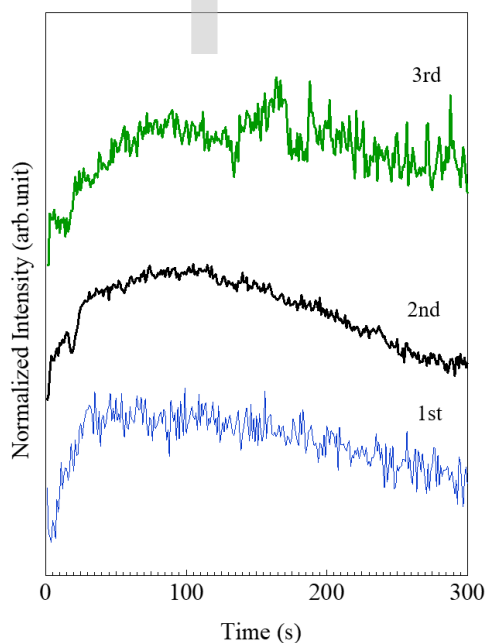
Fig. 6. Change in SERS intensity at 1250 cm^{-1} (E_s = 49.2 µW) .

the Au nanoparticle agglomerates as shown in Fig.

7. When the size of the agglomerates is unevenly distributed, there is a considerable difference in intensity between when the large agglomerates are hit by the laser and when they are not.

Gold agglomerates
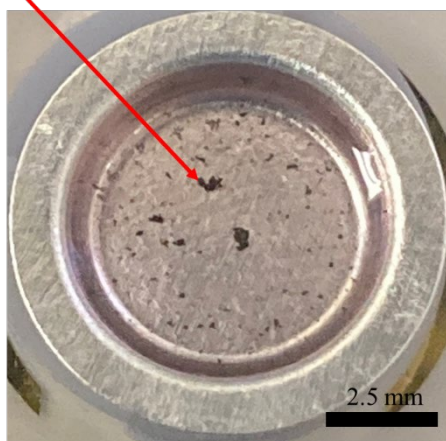
Fig. 7.   Rapid agglomeration of Au particles

To solve this problem, the concentration of gold nanoparticles was reduced. The mixing ratio of the new sample is 3.0 µl of measurement sample, 3.0 µL of 0.5 M NaCl solution, 10µL of Au colloid, and 44 µl pure water. Fig. 8 compares the SERS intensity for the new sample with a supply energy of 39.4 µW. The intensity after saturation is more stable than in Fig. 6. From Fig.9, the formation of large agglomerates as shown in Fig.7 was not observed. Fig. 10 shows the data processed; the five data were normalized with respect to the maximum peak intensity and then averaged. the red line indicates the SERS measurement results. The time to saturation becomes shorter as the number of cycles increases. To determine this saturation time, a verification by relaxation time analysis is performed. The relaxation time is a measure of the time required for a system to change from non-equilibrium to equilibrium. In this case, this time is the time until saturation occurs. The relaxation times were compared by fitting Equation 1 to a graph.

$$I = I_0 + A \exp\left(-\frac{t}{\tau}\right) \qquad (1)$$

The relationship between relaxation time and supplied energy is shown in Fig. 11. As shown in Figure 4, higher supply energy causes rapid particle growth, which also results in more hot spots. The reason why the relaxation time is lower on the high supply energy side in Fig. 11 is that the number of hot spots easily saturates.These results indicate that mixing by SAW is useful for the fabrication of SERS structures.
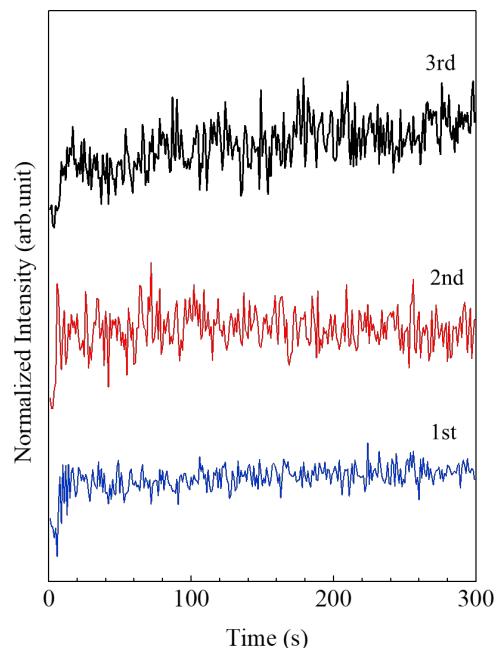
Fig. 8. Change in SERS intensity at 1250 cm^{-1} when measuring new sample. (E_s = 39.4 µW) .
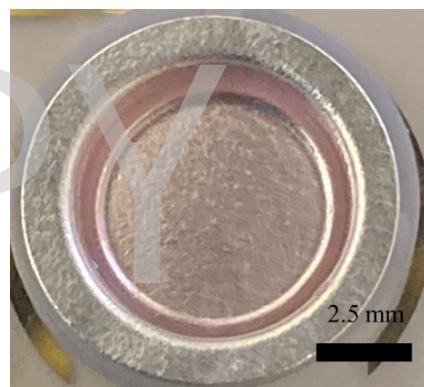
Fig. 9. Photograph after 5 min of rotation with a new sample.(Es= 39.4 µW)
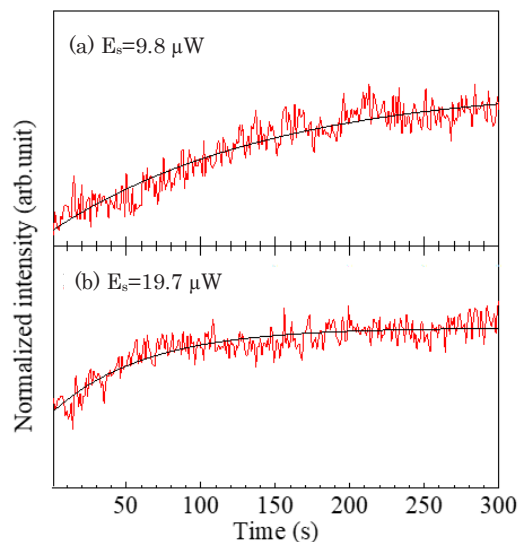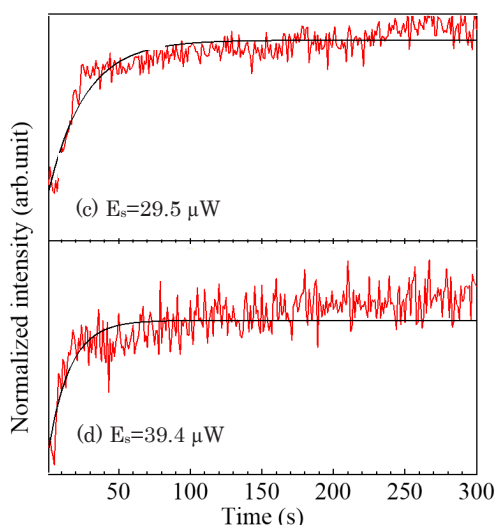
Fig. 10. Change in SERS intensity at 1250 cm^{-1}
(E_s = (a) 9.8 μW, (b) 19.7 μW, (c) 29.5 μW, (d) 39.4 μW)
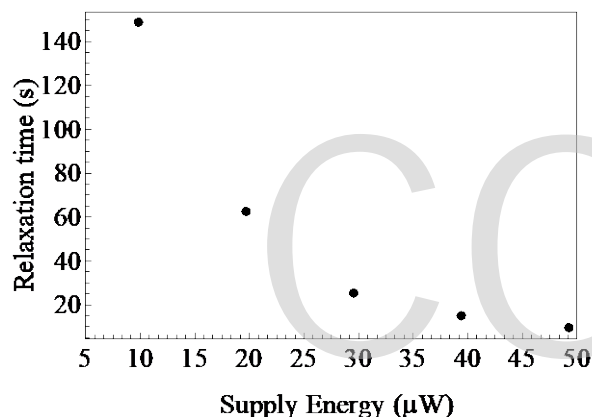
Fig. 11. Relationship between relaxation time and
supply energy.

4. Conclusion

The aggregation of Au nanoparticles by the SAW rotor was evaluated. The volume of agglomerated particles increased with increasing feed energy. This is thought to be due to the increase in the velocity of the nanoparticles and the increase in the collision frequency of the nanoparticles due to the increase in the supply energy. On the other hand, as an application of the agglomeration structure, the SERS intensity was evaluated using 4bpy. The SERS intensity showed a trend of decreasing saturation time with increasing supply energy of SAW. This corresponds to the experiment on agglomeration and is due to the increase of hot spots with the progress of agglomeration. Based on these results, the SAW rotor system is helpful for nanoparticle aggregation and is expected to be applied to SERS measurements in microfluidic devices. In the future, we will confirm the effect by other measurement molecules and construct the system by combining it with the flow channel structure.

References

1. S. J. Lee and S. Y. Lee, Applied Microbiology and Biotechnology, **64** (2004) 3, 289-299.
2. H. Becker and W. Dietz, Microfluidic Devices and Systems, (1998) 177.
3. S. Balslev, A. M. Jorgensen, B. Bilenberg, K. B. Mogensen, D. Snakenborg, O. Geschke, J. P. Kutter, and A. Kristensen, The Royal Society of Chemistry, (2006), 213-217
4. H. A. Stone, A. D. Stroock, and A. Ajdari, Annual Review of Fluid Mechanics, **36**, (2004) 381-411.
5. K. Kneipp, Y. Wang, H. Kneipp, and L. T. Perelman, I. Itzkan, R. R. Dasari, and M. S. Feld, Phys. Rev. Lett. **78** (1997) 1667.
6. W. Xua, X. Linga, J. Xiaoa, M. S. Dresselhausb, J. Kongb, H. Xud, Z. Liua, and J. Zhanga, PNAS, **109** (2012) 9281-9286.
7. C. Zong, M. Xu, L. Xu, T. Wei, X. Ma, X. Zheng, R. Hu, and B. Ren, ,Chem. Rev. , **118** (2018) 4946−4980.
8. J. Jeon, N. Choi, H. Chen, J. Moon, L. Chen, and Jaebum Choo,,Lab Chip, **19** (2019) 674.
9. S. Yue and J. Fang, Z. Xu, **198** (2022) 113822.
10. T. Tanaka, S. Saegusa, M. Naya, T. Fukuoka, S. Amano, Y. Utsumi, and A. Yamaguchi, Journal of Photopolymer Science and Technology, in printing.
11. A. Yamaguchi, T. Fukuoka, and Y. Utsumi, Electron Comm. Jpn. **101** (2018) 38 - 44.
12. A. Yamaguchi, Y. Utsumi, and T. Fukuoka, Applied Surface Science, 465 (2019) 405 – 412.
13. A. Yamaguchi, T. Fukuoka, K. Kuroda, R. Hara, and Y. Utsumi, Colloids and Surfaces A: Physicochemical and Engineering Aspects, **507** (2016) 118-123.
14. A. Yamaguchi, R. Takahashi, T. Fukuoka, R. Hara, and Y. Utsumi, Sensors & Actuator B: Chemical, **230** (2016) 94 – 100.
15. T. Fukuoka, Y. Mori, T. Yasunaga, K. Namura, M. Suzuki, and A. Yamaguchi, Scientific

Reports **12** (2022) 985.

16. S. Saegusa, T. Tanaka, M. Naya, T. Fukuoka, S. Amano, Y. Utsumi, and A. Yamaguchi, IEEJ Transactions on E, in printing.

17. Lord Rayleigh, Proc. London Math. Soc., **17** (1885) 4.

18. E.K Sitting, U.S. Patent **3**, 360, 749 (Filed Dec, Dec. 9 1964)

19. A. Renaudin, K. Chuda, V. Zhang, X. Coqueret, J-C. Camart, P. Tabourier, and C. Druon, Proc. μTAS 2005, (2005) 599-601.

20. K. Sritharan, C. J. Strobl, M. F. Schneider, A. Wixforth, and Z. Guttenberg, Appl. Phys. Lett., **88** (2004) 54102.

21. M. Kurosawa, M. Takashi, and T. Higuchi, IEEE Trans. Ultrason. Ferroelectr. Freq. Control **43** (1996) 901

22. A. Wixforth, Superlattices and Microstruct., **33** (2003) 389-396.

23. K. Chono, N. Shimizu, Y. Matsui, J. Kondoh, and S. Shiokawa, Jpn. J. Appl. Phys. **43**, 5B (2004) 2987-2991.

24. D. Fukuoka and Y.Utsumi, Microsyst. Technol., **14** , 9-11 (2008) 1395-1398.

25. T. Saiki, K. Okada, and Y.Utsumi, International Microprocesses and Nanotechnology Conference (MNC2007), **20** (2007) 332-333.

26. M. Takahashi, A. Yamaguchi, Y. Utsumi, M. Takeo, S. Amaya, H. Sakamoto, and T. Saiki, Journal of Photopolymer Science and Technology, in printing.

27. H.Tanaka and T.Araki, T. Phys. Rev. Lett. **85**, (2000) 1338.

28. A. Barbot and T. Araki, SoftMatter, **13** (2017) 5911.

Hybrid Bonding Technology Utilizing
Molding Compound and Photo Imageable Dielectric Systems

Yuki Imazu[1]*and Kazuyuki Mitsukura[2]

[1] *Resonac Co., Ltd.*
7-7 Shin-Kawasaki, Saiwai-ku, Kawasaki-shi, Kanagawa, 212-0032, Japan
[2] *Resonac America Inc.*
2150 N First St #350, San Jose, CA 95131
*imazu.yuki.xickk@resonac.com

Currently, high-density semiconductor packages have been required to satisfy the demands of realizing high-performance computing network systems. Hybrid bonding is one of the promising processes for 3D-IC package utilizing WoW (wafer on wafer), CoW (chip on wafer) to realize fine vertical interconnection by die stacking. However, the current fabrication processes and materials for hybrid bonding are based on the front-end based technology such as dry processes and Si-based inorganic materials. In this paper, we demonstrated a novel hybrid bonding system using organic materials especially for Epoxy Molding Compound (EMC) and Photo Imageable Dielectric (PID) which are frequently applied to Fan-Out WLP (Wafer Level Package) and PLP (Panel Level Package) with CMP, UV modification and thermal annealing processes.
Keywords: Hybrid bonding, PID, EMC, Surface treatment, UV modification

1. Introduction

Currently, high-density semiconductor packages have been required to satisfy the demand of realizing high-performance computing network system. The structures and assembly processes in 2.xD and 3D-IC package tend to be more and more complicated. Under the situation, logic chips (such as GPU (Graphics Processing Unit), CPU (Central Processing Unit), AI (Artificial Intelligence) accelerator, ASIC (Application Specific Integrated Circuit)) and 3D memory cubes (such as 3D cache and HBM (High Bandwidth Memory)) are usually integrated via chiplet dies with interposer layer. In order to achieve low latency communication, high density interconnections between chiplet die and interposer are required fine via and μ-bumping which is high-yields, low cost and good process window for thermal management. On the other hand, it is usually difficult to narrow the μ-bumping pitches less than 20 μm because of the bump bridge between micro-solder joints [1-17].

For approaching these technical issues, hybrid bonding process is proposed. Hybrid bonding is the concept of Cu-Cu bonding directly without the solder joint without neighbor bridging. Currently, SiO_2, SiN and SiCN are applied for the insulation layers of dies. However, the fabrication cost of inorganic insulation layer tend to be high due to using dry processes for deposition and activating the die surface. In addition, the particle adhesion for the bonding surfaces cause the yield loss. Here, we proposed a novel hybrid bonding system utilizing organic materials such as Epoxy Molding Compound (EMC) and Photo Imageable Dielectric (PID) which are applied to fan-out WLP (Wafer Level Package) and PLP (Panel Level Package) with CMP, UV modification and thermal annealing processes [18-24].

The organic materials for insulation layer of bonding dies needed to be stable during the Cu-Cu diffusion bonding process under the temperature of more than 300 °C. Furthermore, the mechanical strength is required to for planarization by CMP and the pressure of bonding process for the organic insulation materials. Thus, we estimated that PID and EMC are suitable to the hybrid bonding process because these materials have favourable reliabilities against the various reliability tests [25-26].

In addition, for activating the surface of insulation layer, the surface treatment is one of the most important process in hybrid bonding. In general, O_2 plasma treatment using by dry ashing equipment improves wettability for the surface. In this paper, we also focused on the UV modification as an alternative reasonable candidate for the surface treatment. In general, it is known that the UV modification process by low pressure mercury lamp can remove organic dirt and is applied to LCD manufacturing for glass panel cleaning. We compared the treatment effects between O_2 plasma ashing and UV modification for the surface of the organic insulation materials. In this paper, we proposed the novel hybrid bonding systems with EMC and PID materials and reported the experimental results of thermal bonding test, including the UV modification process [27-28].

2. Experimental

2.1 EMC and PID preparation

Here, we fabricated the EMC chips and the PID wafers in 12 inch wafer size, respectively. The fabrication processes of TEGs for organic hybrid bonding are shown in Fig. 1. and Fig. 2. First, we implemented the compression molding granule-type EMC on the 12 inch Si wafer. The thickness of EMC on the wafer was 200 μm. Then, after PMC (Post-Mold-Cure), we grinded EMC surface smoothly by using a wafer grinder (DISCO, DAG810). The thickness of EMC after grinding was 50 μm. After that, CMP (Chemical-Mechanical-Polishing) was conducted to planarize the EMC surface. The thickness of EMC after CMP was 20 μm. In addition, the EMC wafer was singulated into 5.0 mm x 5.0 mm chips with a dicing saw.

Next, we coated the PID varnish on 12 inch Si wafer. The thickness of PID film on the wafer was 10 μm after curing at 230°C. After that, CMP was carried out for the surface of PID to obtain more planar.
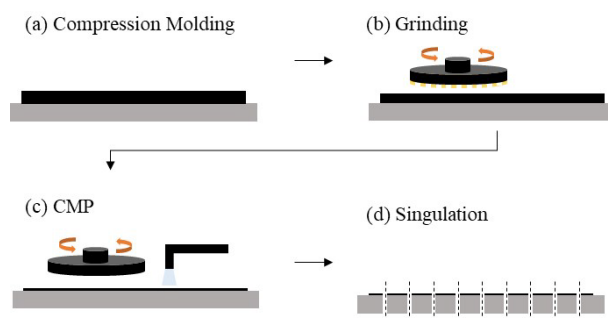
Fig. 1. Fabrication process of EMC chips

Fig. 2. Fabrication process of PID wafer

2.2 Observation of the EMC and PID surface

The surface conditions of EMC and PID before and after CMP were analyzed by using Field Emission Scanning Electron Microscope (FE-SEM) (Hitachi High-Tech, Regulus-8230).

2.3 Surface treatment

As the surface treatment, O_2 plasma ashing and UV modification were conducted. O_2 plasma ashing was conducted under the O_2 atmosphere by using plasma cleaner (Nordson Advanced technology, AP-1000). And that, UV modification was conducted by using UV/Ozone processor (Sen-lights, SSM-16). UV light included wavelengths of 184 nm and 254 nm.

2.4 Surface roughness of EMC and PID

We evaluated the arithmetic average roughness (Ra) and the surface roughness (Rz) for the EMC and PID surface after O_2 plasma ashing or UV modification by using an Atomic Force Microscopy (AFM).

2.5 Wettability and Surface Energy of EMC and PID

We evaluated static contact angle for the dielectric surface after O_2 plasma ashing or UV modification using a contact angle meter (Kyowa, DMo-501). The solvents for evaluating static contact angle were ultrapure water and formamide. The dispersive and polar parts of surface energy were calculated using Kaelble-Uy theory, shown as equation (1).

$$\gamma_L(1 + \cos\theta) = 2\left(\gamma_S^d \gamma_L^d\right)^{0.5} + 2\left(\gamma_S^p \gamma_L^p\right)^{0.5} \quad (1)$$

γ_L : The surface energy of liquid

γ_S: The surface energy of solid

θ : The static contact angle

γ_S^d : The dispersive parts of surface energy

γ_S^p : The polar parts of surface energy

2.6 Elemental analysis of the PID surface

To evaluate the treatment effects of O_2 plasma ashing or UV modification, elemental analysis of the PID surface was conducted by an X-ray Photoelectron Spectroscopy (XPS) (ULVAC-PHI, PHI5000 VersaProbe II). We compared the intensity of spectra of C-H bond, C-C bond, C-O bond, C=O bond and COO bond between two surface treatment processes.

2.7 Thermal bonding using EMC and PID

Fig. 3. shows the process flow scheme of the thermal bonding using EMC and PID by Chip on Wafer (CoW) process. First, the two kinds of surface treatments, namely, O_2 plasma ashing and UV modification were conducted onto the surface of PID wafer. Next, the pre-bonding process was conducted using Flip Chip Bonder (Toray Engineering, MD-4000). After that, the coupons were bonded under a nitrogen atmosphere at 300°C, 5 MPa for 5 min by gang bonder (ALPHA DESIGN, THB-MM). Finally, the annealing was carried out under a nitrogen atmosphere at 250°C, 2 h by inert gas oven (KOYO THERMO, CLH-35CD (III)-S).
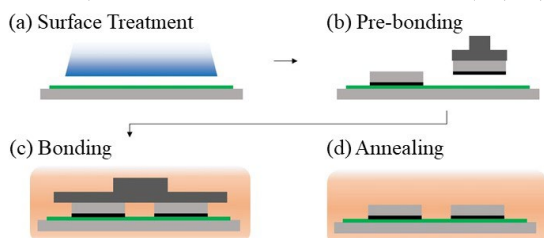
Fig. 3. Thermal bonding process using EMC and PID

2.8 Evaluation of bonding strength between EMC and PID

After the thermal bonding process, shear strength was evaluated by using a bond tester (ROYCE Instruments, ROYCE650) at room temperature.

3. Results and discussion
3.1 Fabrication of EMC chips and PID wafer

We fabricated EMC chips and PID wafer to evaluate hybrid bonding. Fig. 4. (a) and (b) show the SEM images of the EMC and PID surface after CMP.

From these pictures, both of EMC and PID had good flatness after CMP. Especially, the SEM image of EMC shows that cross-section of various size silica filler were exposed in whole.
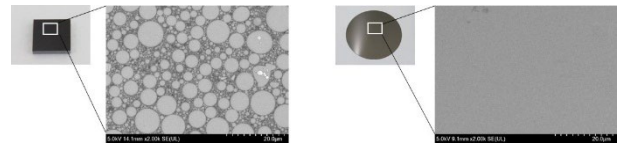
Fig. 4. The SEM images of (a) the EMC chip and (b) the PID wafer after CMP

3.2 The effects of surface treatment on EMC and PI

For the surface treatment, O_2 plasma ashing and UV modification were conducted for the surfaces of EMC and PID. We evaluated the surface roughness trends through the O_2 plasma ashing and UV modification as shown in Fig. 5. (a) and (b), respectively. Fig. 5. (a) showed that the roughness increased by O_2 plasma ashing. On the contrary, as shown in Fig. 5. (b), there were little changes in the roughness by UV modification.
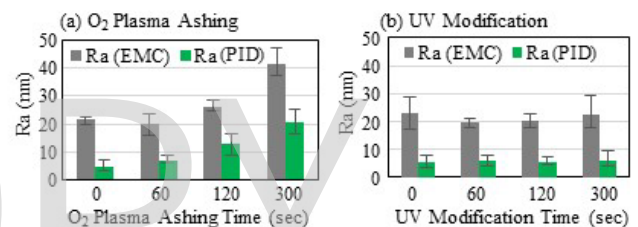
Fig. 5. Roughness Ra on EMC and PI (a) by O_2 plasma ashing and (b) by UV modification

In addition, in order to analyze the effects of O_2 plasma ashing and UV modification for the surfaces of EMC and PID, we evaluated the surface free energy utilizing the static contact angles of ultrapure water and formamide. The polar and dispersive parts of surface free energy were calculated by equation (1) described in experimental section. By surface treatments, the summation of surface free energy was increased as compared to initial values. Especially, the polar parts of surface free energy were increased significantly. These results indicate that surface polarity was improved by O_2 plasma ashing and UV modification.
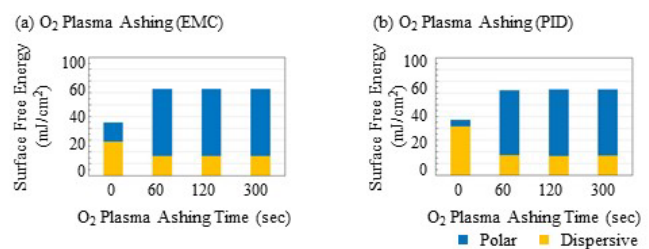
Fig. 6. Relationships between O_2 plasma ashing time and surface free energy (a) EMC and (b) PID
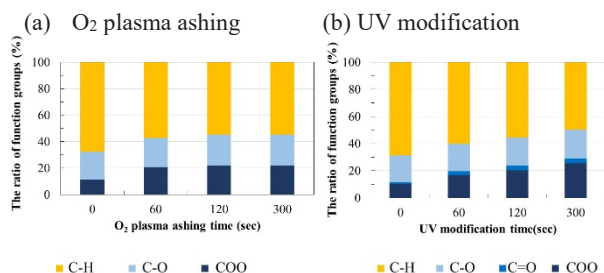
Fig. 7. Relationships between UV modification time and surface free energy (a) EMC and (b) PID

3.3 Elemental Analysis of the PID surface

In order to evaluate the treatment effects of O_2 plasma ashing and UV modification against the PID surface, elemental analysis was carried out by XPS. Fig. 8. showed the results of measurement C1s spectra. In both cases of O_2 plasma ashing and UV modification, the peak of 288.5 eV raised as the treatment time increased. However, there was a difference in the behavior of the peak transition between O_2 plasma ashing and UV modification. In the case of O_2 plasma ashing, the intensity of peak of 288.5 eV jumped up at 60 s, and after 120 s the intensity of this peak little changed. These results suggested that the effect of surface roughening by O_2 plasma ashing blocked the growth the peak of 288.5 eV. On the other hand, in UV modification, the intensity of the same peak grew steadily as the treatment time increased. These results suggest that UV modification can modify chemical bonds without damaging PID surface.
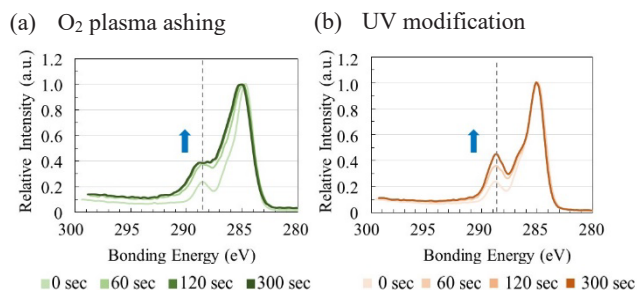
Fig. 8. The relation between C1s spectrum and surface treatment time, (a) O_2 plasma ashing, (b) UV modification

In addition, we analyzed the peak of 288.5 eV shown in Fig. 9. The part of COO bond having polarity increased by O_2 plasma ashing. Whereas the part of C-H bond having dispersibility decreased. Similar to the results of O_2 plasma ashing, the part of COO bond grew and that of C-H bond decreased, as the UV modification time increased. However, for UV modification, C=O bond also increased. These results indicated that the effect of UV

modification was different from the one of O_2 plasma ashing against the PID material.
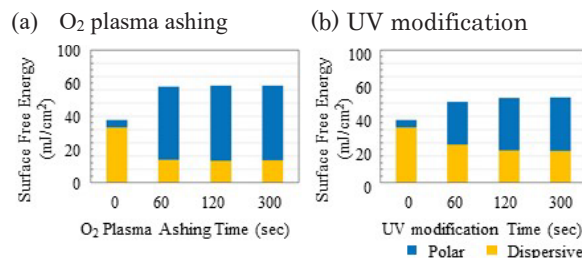
Fig. 9. The ratio of elements of function groups as the PID surface treatment time, (a) O_2 plasma ashing, (b) UV modification.

3.4 Thermal bonding test

Thermal bonding test by using EMC and PID by CoW process was described in Chapter II. As shown in Fig. 10., assembled coupon was obtained after pre-bonding by flip chip bonder. The 5mm x 5mm square size EMC chips were lined up at a pitch of 10mm on PID wafer.

Fig. 10. A photo of an assembled coupon using the EMC/PID system after pre-bonding

Next, the bonding was conducted by gang bonder at 300 °C. After that, the annealing was carried out at 250 °C under nitrogen atmosphere. Fig. 11. shows the cross-sectional SEM image of an assembled coupon. There were no voids or gaps at the interface between EMC and PID. This result indicated that the novel system utilizing EMC and PID is suitable for the hybrid bonding process.
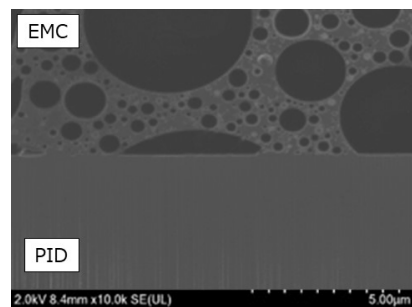
Fig. 11. The cross-sectional SEM image of a thermal bonded coupon using EMC and PID

3.5 Evaluation of shear strength

In order to evaluate the effects of O_2 plasma ashing and UV modification for bonding strength between EMC and PID, we measured shear strength by using a bond tester. The results of shear test with two kinds of the surface treatment were shown in Fig. 12. These results showed that the shear strength little changed by any treatment conditions of O_2 plasma ashing. On the other hand, UV modification improved the shear strength drastically. Especially, after UV modification for 120 s, the shear strength increased five times stronger as compared to no treated coupons. These results indicated that UV modification accomplished an excellent shear strength with the EMC and PID system.
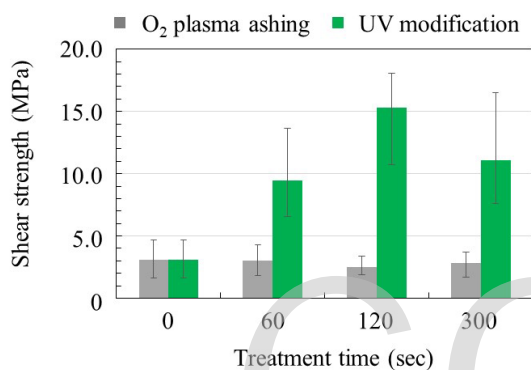
Fig. 12. The results of shear test of coupons treated by O_2 plasma ashing and UV modification

Furthermore, we compared the bonding condition of the PID/EMC interface treated by O_2 plasma ashing and UV modification. The SEM images of the surfaces of PID after shearing EMC chips were shown in Fig. 13. As shown in Fig. 13. (a), there was little EMC residue on the PID surface treated by O_2 plasma ashing. Whereas, as shown in Fig. 13. (b), there was a large amount of EMC residue on the PID surface treated by UV modification. As these results, after O_2 plasma ashing, the interface between PID and EMC was fractured, while after UV modification, the bulk of EMC was fractured.

(a) O_2 plasma ashing   (b) UV modification
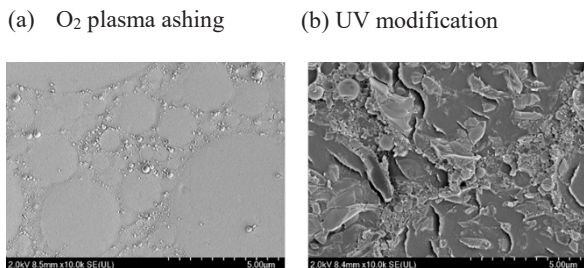
Fig. 13. The SEM image of PID surface after shearing the EMC chip (a) treated by O_2 plasma ashing, (b) treated by UV modification

Finally, we compared the shear strength between the EMC/PID system and the Polyimide/Polyimide (PI/PI) system as shown in Fig. 14. From these results, the shear strength of the EMC/PID system were a little smaller level of the PI/PI system referred from [23] indicating that the adhesion strength of EMC and PID was strong adequately for hybrid bonding. In the future, we will investigate the hybrid bonding with Cu-Cu junction using the EMC and PID system.
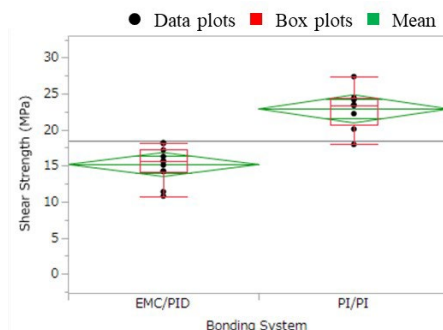
Fig. 14. The results of shear test using the EMC/PID system and PI/PI system.

4. Conclusion

In order to propose the novel hybrid bonding systems by using organic materials such as EMC and PID, we achieved thermal bonding between those materials by using UV modification process. It can be indicated that UV modification is the excellent way of surface treatment to increase the adhesion strength of EMC and PID. As compared to O_2 plasma ashing, UV modification is superior process to improve wettability and the polarity part of surface free energy for EMC and PID surfaces without roughening them. UV modification can improve the shear strength between EMC and PID five times more than untreated coupons.

Reference
1. J. H. Lau, *IEEE. Transactions on Components Packaging and Manufacturing Technology.*, **12** (2022) 228.
2. J H. Lau, *IEEE. Transactions on Components, Packaging and Manufacturing Technology*, **11** (2021) 1301.
3. C. C. Lee, *IEEE 66nd Electron. Compon. Technol. Conf. (ECTC).*, (2016) pp. 1439–1444
4. R. Mahajan, *IEEE 66nd Electron. Compon. Technol. Conf. (ECTC)*, (2016) 557.
5. G. E. Moore, *Electronics.*, **38(8)** (1965)
6. S. Pal, *IEEE. International Symposium on High Performance Computer Architecture,* (2018) 466.
7. C. H. Yu, *IEEE Transactions on Electron*

Devices., **69** (2022) 258.

8. R. Chaware, *in Proc. IEEE 62nd Electron. Compon. Technol. Conf. (ECTC)*, (2022), 279.

9. S. Y. Hou, *IEEE. Transactions on Electron Devices.*, **64** (2017) 4071.

10. J. H. Lau, *IEEE. Transactions on Components, Packaging and Manufacturing Technology.*, **12** (2022) 1271.

11. K. Oi, *IEEE 64th Electron. Compon. Technol. Conf. (ECTC)*, (2014) 348.

12. N. Shimizu, *in Proc. International Symposium on Microelectronics (IMAPS)*, (2012) 414.

13. M. F. Chen, C. H. Tsai, T. Ku, W. C. Chiou, C. T. Wang, and D. Yu, *IEEE. Trans. Electron Devices.*, **67** (2020) 5343.

14. C. H. Yu, *in IEDM Tech. Dig.*, (2021) 75.

15. C. T. Wang, *IEEE. Symposium on VLSI Technology and Circuits Digest of Technical Papers*, (2022) 258.

16. M. Mariappan, *IEEE. 72nd Electron. Compon. Technol. Conf. (ECTC),* (2022) 1138.

17. K. Wang, *IEEE. 19th International Conference on Thermal, Mechanical and Multi-Physics Simulation and Experiments in Microelectronics and Microsystems (EuroSimE)*, (2018) 1/5.

18. A. Phommahaxay, *IEEE. 69th Electron. Compon. Technol. Conf. (ECTC)*, (2019) 607.

19. K. Onishi, *IEEE. International Conference on Electronics Packaging (ICEP)*, **TC1-3**, (2022) 59.

20. E. Beyne, *IEEE. International Electron Devices Meeting (IEDM)*, (2017), 32.4.1.

21. A. P. Lujan, *IEEE. International Conference on Electronics Packaging (ICEP)*, (2022) 129.

22. H. Ren, *IEEE. 72nd Electron. Compon. Technol. Conf. (ECTC)*, (2022) 149.

23. T. Shirasaka, *IEEE. 72nd Electron. Compon. Technol. Conf. (ECTC)*, (2022) 317.

24. Y. Kurita, *IEEE 3rd Electronics System Integration Technology Conference (ESTC)*, (2010) 1.

25. L. Mirkarimi, *IEEE. 72nd Electron. Compon. Technol. Conf. (ECTC)*, (2022) 162.

26. T. S. Widodo, *IEEE. 72nd Electron. Compon. Technol. Conf. (ECTC)*, (2022) 1271.

27. S. P. S. Lim, *IEEE. 71st Electron. Compon. Technol. Conf. (ECTC)*, (2022) 438.

28. M. Toba, *53rd International Symposium on Microelectronics (IMAPS)*, (2020) 174.

Photo-thermal Dual Cured Blends of TiO$_2$/diarylfluorene Films with High Refractive Indices

Haruyuki Okamura[1]*, Keiko Minokami[2], Hirotsugu Kuratani[2], and Shinsuke Miyauchi[2]

[1] *Department of Applied Chemistry, Graduate School of Engineering, Osaka Metropolitan University,*
1-1 Gakuen-cho, Naka-ku, Sakai, Osaka 599-8531, Japan
[2] *Frontier Materials Laboratories, Osaka Gas Chemicals Co., Ltd.,*
5-11-61, Torishima, Konohana-ku, Osaka 544-0051, Japan
*okamura@omu.ac.jp

We developed photocured films from a blend of TiO$_2$ nanoparticles and dinaphthylfluorene derivatives having acryl and mercapt groups and a photoinitiator by a photo-thermal dual curing technique. The curing properties of the blends were strongly affected by the photo-thermal dual curing conditions. We successfully fabricated films with high refractive indices (1.693 at 589 nm) and a high thermal stability (5% weight loss temperature: 266 ℃).
Keywords: Photo-thermal dual curing, Fluorene, Acryl, TiO$_2$, High thermal stability, High refractive index

1. Introduction

Organic-inorganic hybrid nanocomposite materials have attracted much attention to improve the physical and chemical properties of organic materials [1]. Based on this point of view, Matsukawa et al. reported the preparation of organic-inorganic hybrid films having high refractive indices [2-4]. They used TiO$_2$ and ZnO$_2$ as inorganic compounds which have high refractive indices. We also reported the fabrication of photocured films of diphenyl- or dinaphthylfluorene having acryl, epoxy, and oxetane moieties and polysilanes blends [5-8]. We have successfully fabricated the films with high refractive indices (n_D: 1.62) and the decrease of about a 0.03 refractive index was observed after the photodecomposition at 254 nm with a dose of 18 J/cm^2 [7]. The prepared films have a high thermal stability (temperature for 5% weight loss, T_{d5}: 300 ℃) [7].

In this study, we employed TiO$_2$ nanoparticles as an inorganic compound. We developed the photocured films of a blend of TiO$_2$ nanoparticles and dinaphthylfluorene derivatives having acryl and thiol groups and a photoinitiator by the photo-thermal dual curing technique. The optical and thermal properties of the photocured films were investigated. The photocuring mechanism was also discussed.

2. Experimental

The structures of the used chemicals are shown in Fig. 1. Diphenyl(2,4,6-trimethyl-benzoyl)phosphine oxide (TPO), a photoinitiator, was used as received. A hexafunctional acrylate dipentaerythritol hexaacrylate (DPHA) was kindly donated by Shin-Nakamura Chemical Co., Ltd., and used without further purification. 9,9-Bis[6-(3-acryloyloxy-2-hydroxypropoxy)-2-naphthyl]-fluorene (BNFGA), 9*H*-fluoren-9-ylidenebis(6,2-naphthyleneoxy-2,1-ethanediyl) 3-mercaptbutyrate (BNEFMB), and a TiO$_2$ dispersion in *N*-methylpyrrolidone were obtained from Osaka Gas Chemicals Co., Ltd.

Solvent exchange of the TiO$_2$ dispersion was carried out by dialyzing the obtained dispersion against acetylacetone for 1 day using a Spectra/Por 7 dialysis membrane (cutoff molecular weight: 3500). The concentration of TiO$_2$ after dialysis was determined by thermogravimetry at 500 ℃.

Sample films (ca. 1 μm) were prepared by spin-

casting from the mixture of fluorene derivatives, TiO_2, a photoinitiator, and acetylacetone onto a silicon wafer.

Photo-thermal dual curing was performed by irradiation at 405 nm using an LED laser (Ball Semiconductor, BP300, 300 mW, 48 mW/cm^2) along with baking using a conventional hot plate. The intensity of the light was measured by an Orc Light Measure UV-M02 and an Ushio USR-45VA. The irradiated films were soaked in tetrahydrofuran and the insoluble fraction was determined by comparing the film thickness before and after soaking in tetrahydrofuran for 1 min. The thickness of the films was measured by interferometry (Nanometrics Nanospec M3000).

The UV-vis spectra were obtained by a Shimadzu UV-2450. The FT-IR measurements were carried out using a JASCO FT/IR-4600. The refractive indices of the films were measured using a spectroscopic ellipsometer (J. A. Woollam M-2000UL). Thermal decomposition behavior was investigated by a Shimadzu DTG 60 simultaneous thermogravimetry and differential thermal analyzer (TG-DTA) under flowing nitrogen. The heating rate was 10 °C/min.

Fig. 1. Chemical structures of the used chemicals.

3. Results and discussion

3.1. Photo-thermal dual curing

Incorporation of TiO_2 in organic films produced a high thermal stability and high refractive indices [2,3]. Thus, we prepared blended films of TiO_2 and DPHA, a hexafunctional acrylate which gave a high reactivity by photo-induced radical polymerization in the presence of a photoinitiator. When a DPHA/TiO_2/TPO (67/33/1, wt/wt/wt) blended film was irradiated at 405 nm for 5 min with a dose of 14.4 J/cm^2 under ambient conditions, a low insoluble fraction (33%) was observed. A photo-thermal dual curing technique [7,9] enhanced the reactivity. The insoluble fraction increased with the irradiation temperature. When the irradiation was carried out at 100 °C for 5 min, a 96% insolubilization was observed. On the other hand, insolubilization was not observed without irradiation.

The incorporation of fluorene moieties into the films enhanced the refractive indices [2-8]. BNFGA, a diacrylate having naphthyl and fluorenyl moieties was used instead of DPHA. When a BNFGA/TiO_2/TPO (67/33/1, wt/wt/wt) film was irradiated at 405 nm for 5 min with a dose of 14.4 J/cm^2 under ambient conditions, insolubilization was not observed after the irradiation. When irradiation was performed at 100 °C for 5 min, a 46% insolubilization was observed. A longer irradiation time was effective to increase the insoluble fraction. When irradiation was performed at 100 °C for 15 min, a 94% insolubilization was observed. On the other hand, insolubilization was not observed without irradiation.

The TiO_2 content affected the insolubilization. When a BNFGA/TiO_2/TPO (50/50/1, wt/wt/wt) film was irradiated at 405 nm for 15 min with a dose of 43.2 J/cm^2 at 80 °C, a 94% insolubilization was observed. Without irradiation, no insolubilization was observed. When the temperature was increased to 100 °C, insolubilization was observed regardless of the irradiation. Thus, the optimum conditions to fabricate the cured BNFGA/TiO_2/TPO (50/50/1, wt/wt/wt) blended film was determined to be a 15-min irradiation at 80 °C.

The thiol-ene reaction [7,10] was used to enhanced the reactivity. BNEFMB, a dimercapt derivative having naphthyl and fluorenyl moieties, was added in the system. When a BNFGA /BNEFMB/TiO_2/TPO (44/22/33/1, wt/wt/wt/wt) blended film was irradiated at 100 °C for 5 min, insolubilization was observed. The value (81%)
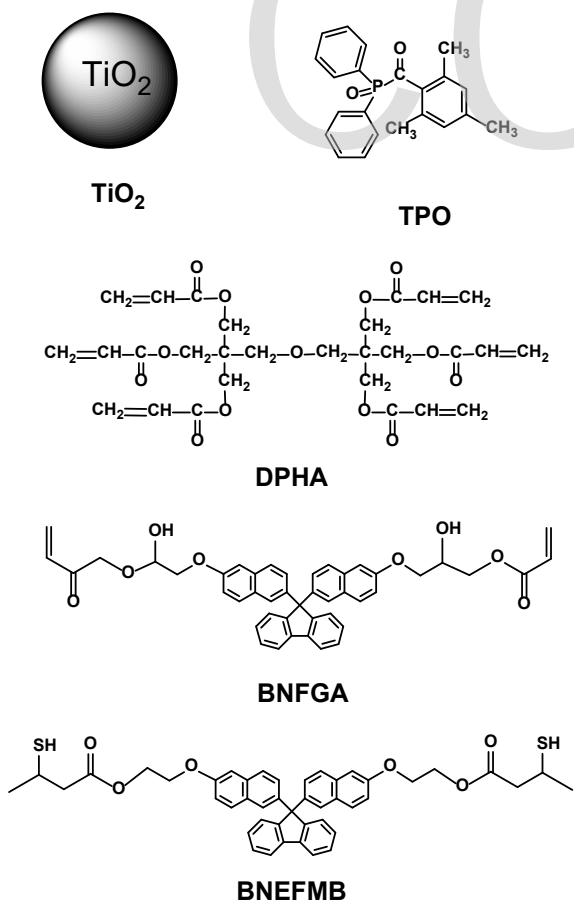
was higher than that when the BNFGA/TiO$_2$/TPO (66/33/1, wt/wt/wt) blended film was used (46%). The optimum condition to fabricate the cured BNFGA/BNEFMB/TiO$_2$/TPO (44/22/33/1, wt/wt/wt/wt) blended film was determined to be a 15-min irradiation at 80 °C, which gave an 89%-insoluble fraction.

3.2. Reaction mechanism

The FT-IR spectral changes revealed the reaction mechanism of the blended films. Figure 2 shows the FT-IR spectral changes of the BNFGA/TiO$_2$/TPO (50/50/1, wt/wt/wt) and BNFGA/BNEFMB/TiO$_2$/TPO (44/22/33/1, wt/wt/wt/wt) blended films. After irradiation, the peak at around 1630 cm^{-1} ascribed to the C=C stretching of the acryl groups decreased. After additional baking at 200 °C for 1 min, the peak above 3000 cm^{-1} ascribed to the hydroxy groups in TiO$_2$ decreased.
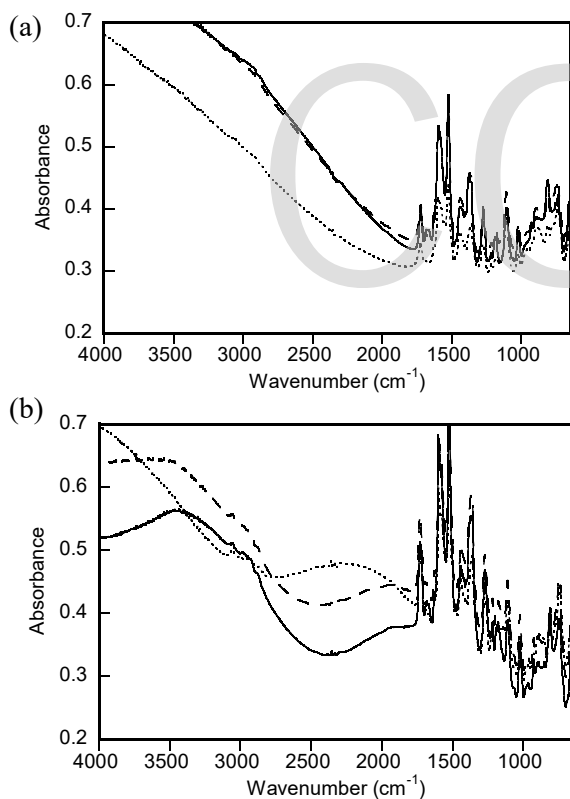
Fig. 2. FT-IR spectral changes of (a) BNFGA/TiO$_2$/TPO (50/50/1, wt/wt/wt) and (b) BNFGA/BNEFMB/TiO$_2$/TPO (44/22/33/1, wt/wt/wt/wt) blended films containing 1 wt% TPO. Solid line: no irradiation. Dashed line: irradiated at 405 nm for 15 min with heating at 80 °C. Irradiation intensity: 48 mW/cm^2. Dotted line: additional baking at 200 °C for 1 min after irradiation. Film thickness: 0.81 μm.

Scheme 1 shows a plausible reaction mechanism of the BNFGA/BNEFMB/TiO$_2$/TPO blended system. Upon irradiation, the photoinitiator TPO was photolyzed to produce radicals. The generated radicals promote the polymerization of BNFGA in addition to the crosslinking reactions of the acryl groups in the BNFGA and mercapt groups of BNEFMB. The reactions induced the insolubilization of the films due to the nature of the difunctional compounds of BNFGA and BNEFMB. As minor reactions, dehydration of the hydroxy groups on TiO$_2$, the hydroxy groups in BNFGA, and the mercapt groups in BNEFMB proceeded. We consider the baking treatment accelerates the minor reactions.
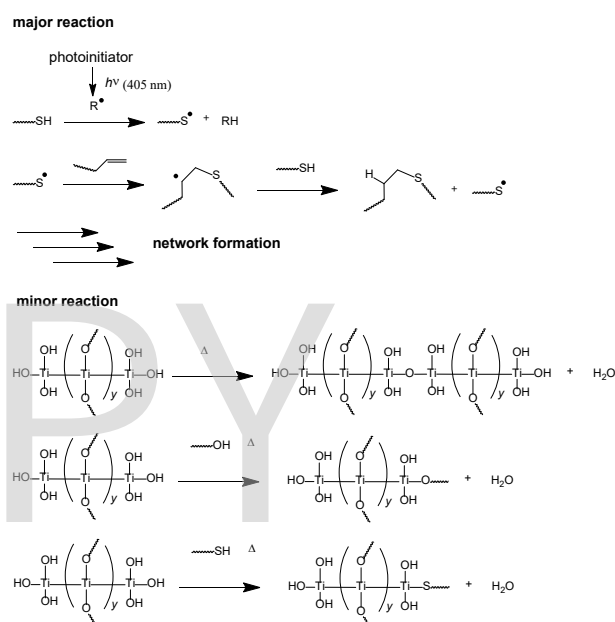
Scheme 1. Plausible reaction mechanism.

3.3. Thermal and optical properties

The TGA analyses of the photocured and baked BNFGA/TiO$_2$/TPO (50/50/1, wt/wt/wt) and BNFGA/BNEFMB/TiO$_2$/TPO (44/22/33/1, wt/wt/wt/wt) blended films were carried out. The films were prepared by irradiation at 405 nm for 15 min with heating at 80 °C and additional baking at 200 °C for 1 min after the irradiation. The 5% weight loss temperature (T_{d5}) of the BNFGA/TiO$_2$/TPO (50/50/1, wt/wt/wt) and BNFGA/BNEFMB/TiO$_2$/TPO (44/22/33/1, wt/wt/wt/wt) blended films were 266 and 197 °C, respectively.

The UV-vis spectral changes of the BNFGA/TiO$_2$/TPO (50/50/1, wt/wt/wt) and BNFGA/BNEFMB/TiO$_2$/TPO (44/22/33/1, wt/wt/wt/wt) blended films were observed (Fig. 3). When the films were irradiated at 405 nm for 15 min

with heating at 80 ºC, an increase in the absorption above 400 nm was observed in both films. The increase was enhanced by additional baking at 200 ºC for 1 min.
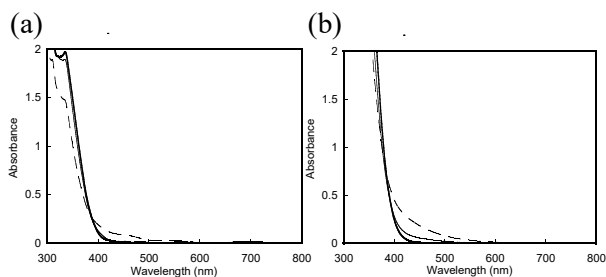
Fig. 3. UV-vis spectral changes of (a) BNFGA/TiO$_2$/TPO (50/50/1, wt/wt/wt) and (b) BNFGA/BNEFMB/TiO$_2$/TPO (44/22/33/1, wt/wt/wt/wt) blended films containing 1 wt% TPO. Bold line: no irradiation. Solid line: irradiated at 405 nm for 15 min with heating at 80 ºC. Irradiation intensity: 48 mW/cm^2. Dashed line: additional baking at 200 ºC for 1 min after irradiation. Film thickness: (a) 0.77 μm, (b) 2.0 μm.
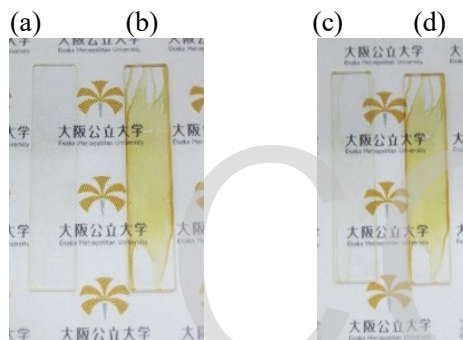
Fig. 4. Optical images of (a,c) BNFGA/TiO$_2$/TPO (50/50/1, wt/wt/wt) and (b,d) BNFGA/BNEFMB/TiO$_2$/TPO (44/22/33/1, wt/wt/wt/wt) blended films containing 1 wt% TPO. Curing condition: (a,b) irradiated at 405 nm for 15 min with heating at 80 ºC. Irradiation intensity: 48 mW/cm^2. (c,d) additional baking at 200 ºC for 1 min after irradiation. Film thickness: (a) 0.77 μm, (b) 2.0 μm.

Figure 4 shows the optical images of the BNFGA/TiO$_2$/TPO (50/50/1, wt/wt/wt) and BNFGA/BNEFMB/TiO$_2$/TPO (44/22/33/1, wt/wt/wt/wt) blended films before and after baking at 200 ºC for 1 min. Strong coloring was observed in the BNFGA/BNEFMB/TiO$_2$/TPO (44/22/33/1, wt/wt/wt/wt) blended film. The oxidation of the sulfur atoms in BNEFMB may cause the color change.

The refractive indices of the cured BNFGA/TiO$_2$/TPO (50/50/1, wt/wt/wt) and BNFGA/BNEFMB/TiO$_2$/TPO (44/22/33/1, wt/wt/wt/wt) blended films were investigated (Table 1). The n_D values ranged from 1.677 to 1.693. The baking treatment increased the refractive indices.

Table 1. Curing conditions and refractive indices of TiO$_2$/diarylfluorene blended films.

Formulation (weight ratio)				Curing condition	n_F[a]	n_D[b]	n_C[c]	ν_d[d]
BNFGA	BNEFMB	TiO$_2$	TPO					
50		50	1	dual cured[e]	1.709	1.677	1.666	16
50		50	1	dual cured and baked[f]	1.726	1.693	1.681	15
44	22	33	1	dual cured[e]	1.715	1.686	1.675	17
44	22	33	1	dual cured and baked[f]	1.720	1.690	1.678	17

[a]Measured at 486 nm. [b]Measured at 589 nm. [c]Measured at 656 nm. [d]Abbe number: $(n_D-1)/(n_F-n_C)$. [e]80 ºC, 15 min, 43.2 J/cm^2. [f]80 ºC, 15 min, 43.2 J/cm^2 + 200 ºC, 1 min.

4. Conclusion

We developed photocured films from a blend of TiO$_2$ nanoparticles and dinaphthylfluorene derivatives having acryl and mercapt groups and a photoinitiator by a photo-thermal dual curing technique. The curing properties of the blends were strongly affected by the photo-thermal dual curing conditions. A cured BNFGA/TiO$_2$/TPO (50/50/1, wt/wt/wt) film had high refractive indices (1.693 at 589 nm) and a high thermal stability (5% weight loss temperature: 266 ºC).

Acknowledgement

References

1. B. M. Novac, *Adv. Mater.*, **5** (1993) 422.
2. K. Matsukawa, Y. Matsuura, A. Nakamura, N. Nishioka, T. Motokawa, and H. Murase, *J. Photopolym. Sci. Technol.*, **19** (2006) 89.
3. K. Matsukawa, Y. Matsuura, A. Nakamura, N. Nishioka, H. Murase, and S. Kawasaki, *J. Photopolym. Sci. Technol.*, **20** (2007) 307.
4. Y. Minami, K. Murata, S. Watase, A. Matsumoto, and K. Matsukawa, *J. Photopolym. Sci. Technol.*, **26** (2013) 491.
5. H. Okamura, K. Funamoto, M. Matsumoto, K. Minokami, and S. Miyauchi, *J. Photopolym. Sci. Technol.*, **27** (2014) 525.
6. H. Okamura, M. Iseki, K. Degawa, A. Matsumoto, K. Minokami, and S. Miyauchi, *J. Photopolym. Sci. Technol.*, **30** (2017) 683.
7. H. Okamura, A. Matsumoto, K. Minokami, and S. Miyauchi, *J. Photopolym. Sci. Technol.*, **31** (2018) 503.
8. H. Okamura, K. Minokami, and S. Miyauchi, *J. Photopolym. Sci. Technol.*, **33** (2020) 279.
9. H. Okamura, T. Matoba, K. Takada, M. Yamashita, M. Shirai, and A. Matsumoto, *Proc. Org. Coat.*, **100** (2016) 47.
10. C. E. Hoyle, T. Y. Lee, and T. Roper, *J. Polym. Sci. Part A: Polym. Chem.*, **42** (2004) 5301.

Photo-reactivity of 2,4,6-Tris(benzylthio)-1,3,5-triazines and Accompanying Refractive Index Change

Akira Takahashi, Takeshi Maehara, and Atsushi Kameyama*

Department of Chemistry, Kanagawa University,
3-27-1 Rokkakubashi, Kanagawa-ku, Yokohama City, Kanagawa 221-8686, Japan
*kameya01@kanagawa-u.ac.jp

The photo-isomerization reaction of 2,4,6-tris(benzylthio)-1,3,5-triazine (TBT) structure was investigated for the first time. Pristine TBT was prepared as the model compound. TBT showed good thermal inertness up to 200 °C without any thermal isomerization. The photoreaction of TBT under 254 nm irradiation was investigated with UV/vis and FT-IR spectroscopy using the TBT film in poly(methyl methacrylate) (PMMA) matrix. Detailed analysis of the spectra using density functional theory (DFT) calculation revealed that the single enol-keto isomerization at one benzylthio moiety in TBT dominantly proceeded. The refractive index change along with the photo-isomerization of TBT was evaluated with ellipsometry technique, which showed the refractive index increase of +0.0050 at 633 nm.
Keywords: Thiocyanurate, Photo-isomerization, Refractive index change, PMMA film

1. Introduction

The molecules with modulable refractive index (*n*) are important functional materials for many optical devices [1]. Such function has often been realized by designing the photo-reactive molecules, which enable on-demand patterning of the refractive index of materials. To this end, many molecular units with selective photo reactivity have been explored such as nitrones [2–4], cinnamates [5], norbornadiene [6–8], azobenzene [8], and thiocyanates [9]. Recent examples involve photo-Fries rearrangement of aromatic esters [10–14], amides [15], and urethanes [16]. The photo reactions of these molecules induce the changes in molecular refraction (*R*) and molecular volume (*V*), and the concomitant changes of R/V lead to the refractive index changes according to Lorentz–Lorenz equation (1) [17].

$$\frac{n^2 - 1}{n^2 + 2} = \frac{[R]}{V} \quad (1)$$

While a variety of examples of the refractive index modulation of organic molecules including polymers has been reported to date, little has been reported for the polymers with high refractive index. Such high refractive index is one of the important parameters for high performance optical devices such as microlens and light emitting diodes [18]. The high refractive index molecules can be generally designed by incorporation of the molecular units with heavy atoms and/or aromatic rings, which contribute to high molecular refraction *R* and thus high refractive index. Among them, the aromatic polymers with thiotriazines (thiocyanurates) and its derivatives have been reported to show high refractive index over 1.7 [18–20]. Meanwhile, our group has previously revealed that the thermal rearrangement of cyanurates to isocyanurates in polymer backbone afford the refractive index increase up to 0.051, which is attributed to the formation of C=O group with high molar refractions [21]. Because C=S group possesses even higher molar refractions [22], the rearrangement of thiocyanurates to isothiocyanurates could also afford the refractive index increase. In other words, thiocyanurate-containing polymers can be a promising candidate for the optical polymers with both high refractive index and its adjustability. However, such rearrangement reaction of thiocyanurate has yet to be reported. On the other hand, thiobenzothiazole derivatives with the common N=C–S–R substructure have been reported to undergo photo-rearrangement to

N(S)–C–R [23], supporting the feasibility of the targeted photo-rearrangement of thiocyanurates. In this work, we designed 2,4,6-tris(benzylthio)-1,3,5-triazine (TBT) with photolytically cleavable benzylthio groups, and investigated the photo-rearrangement reaction and concomitant refractive index change.

2. Experimental

2.1. Materials and measurements

All the reagents and solvents were purchased from TCI, Wako Pure Chemical Industries, Kanto Chemical, or Sigma-Aldrich and used as received, unless otherwise noted. FT-IR spectra were measured with JASCO Inc. FT/IR4600 spectrometer. UV/vis spectra were measured with JASCO Inc. FT/IR4600 spectrometer. ^{1}H NMR measurements were carried out at 25 °C with DMSO-d_6 as the solvent and tetramethylsilane (0.00 ppm) as the internal standard on a JEOL ECA-500 instrument. Differential scanning calorimetry (DSC) analysis was performed on a Seiko EXSTAR DSC 6200 at heating and cooling rate of 10 °C/min under N$_2$ flow. Density functional theory (DFT) calculation was performed with Wavefunction Inc. Spartan '18 software at the B3LYP/6-311+G(d,p) level. The refractive index and thickness of polymer films were determined by ellipsometry (DHA-OLX/S4, 633 nm, Mizojiri Optical Co. Ltd.).

2.2. Synthesis of TBT (Scheme 1)

In a 100 mL flask, triethylamine (TEA, 7.29 g, 72.0 mmol) was added to thiocyanuric acid (3.76 g, 20.0 mmol) in DMAc (20 mL). The flask was immersed in an ice bath, and benzyl bromide (16.4 g, 90.0 mmol) was added dropwise to the solution over 15 minutes. The solution was stirred for 4.5 h until the consumption of thiocyanuric acid was confirmed by thin layer chromatography. The reaction solution was poured into 600 mL of water, and the formed precipitate was collected by filtration, washed twice with 80 mL of methanol, and then dried under reduced pressure. The crude product was purified by recrystallization from methanol to give TBT as a colorless needle crystal (7.25 g, 76% yield).

^{1}H-NMR (500 MHz, DMSO-d_6, 25 °C) δ (ppm) : 7.36 (d, $J = 7.5$ Hz, 6H), 7.31 (t, $J = 7.5$ Hz, 6H), 7.26 (t, $J = 7.5$ Hz, 3H), 4.40 (s, 6H); ^{13}C-NMR (126 MHz, DMSO-d_6, 25 °C) δ (ppm): 178.68, 136.69, 128.89, 128.56, 127.38, 33.64; FT-IR (KBr, cm^{-1}) : 3022 ($\nu_{C-H, aryl}$), 2926 ($\nu_{C-H, alkyl}$), 1472 ($\nu_{C=N}$),

1267 ($\nu_{C=N}$), 1239 ($\nu_{C=N}$), 786 (ν_{C-S}); ESI-TOF MS (m/z) calcd. for [M+Na$^+$] = 448.10, found: 448.13; m.p. = 85.0–85.3 °C.

2.3. Photo-irradiation experiments of TBT

Typically, TBT films were prepared by spin-coating of the solution of TBT with PMMA matrix (20 wt%) in 1,2-dicholoroethane on a quartz plate for UV/vis, KBr plate for FT-IR, or Si plate for ellipsometry. The films were irradiated with a Xe lamp (Asahi Spectra MAX-302) equipped with a band-pass filter at 254 nm with the intensity of 1.12 mW/cm^2.

3. Results and discussion

3.1. Synthesis and characterization of TBT

TBT was first synthesized as the model compound by the condensation of thiocyanuric acid and benzyl bromide in the presence of triethylamine (TEA) in N,N-dimethylacetoamide (DMAc) at r.t. for 4.5 h (Scheme 1). TLC analysis of the reaction mixture suggested the selective conversion of thiocyanuric acid to a single product. The FT-IR spectrum of the product showed the peaks attributed to C–H groups at 2900–3100 cm^{-1}, triazine ring at 1473 cm^{-1}, and C–S groups at 839 cm^{-1}. The ^{1}H and ^{13}C NMR spectra of the product indicated the presence of a single benzyl structure, as consistent to the trigonal structure of TBT. ESI-TOF MS measurement confirmed the mass peaks corresponding to the H$^+$ and Na$^+$ adducts of TBT.

Our group has previously reported the thermal rearrangement of triphenyl cyanurates in the presence of tetrabutylammonium bromide as the catalyst [21]. We have also reported the thermal rearrangement of 2-(benzoylthio)benzoxazole to 3-benzoylbenzoxazoline-2-thione without any catalyst, which involves the structural change from N=C–S–R to N(S)–C–R [24]. Based on these examples, we briefly examined the thermal reactivity of TBT by differential scanning calorimetry (DSC). As the result, only one endothermic peak attributed to the melting point was observed at 86 °C during the heating up to 200 °C (Fig. 1), indicative of the thermal inertness of TBT. In fact, the ^{1}H NMR spectrum of the DSC
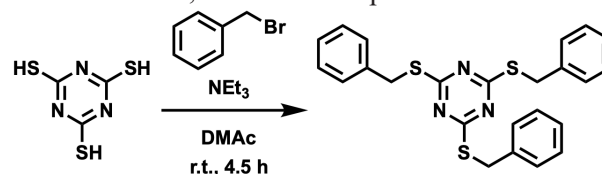
Scheme 1. Synthesis of TBT from thiocyanuric acid.

sample after the heating was comparable to the pristine one, supporting the good thermal stability of TBT in contrast to the 2-(benzoylthio)-benzoxazoles.

3.2. Photoreaction of TBT

The photoreactivity of TBT was next investigated. Herein, the targeted photoreaction was expected to proceed via the homolytic cleavage of the C–S bond between the benzyl and triazine groups. Such reactions have been known to be generally disturbed by the intermediate diffusion particularly in a solution [25]. According to these backgrounds, we carried out the photo experiments in the thin film state using poly(methyl methacrylate) (PMMA) as the film-forming matrix, where the molecular mobility should be more suppressed than in a solution. The photoreaction of TBT was first investigated by UV/vis spectroscopy using the film of TBT prepared on a quartz substrate, which was irradiated at 254 nm (1.12 mW/cm^2). The original absorption peak at 265 nm decreased while new peaks appeared at 288 nm and further longer wavelength region up to *ca.* 400 nm (Fig. 2). This result is in accordance with other reports on the UV/vis spectral changes along with the enol–keto isomerization of thioamide derivatives [23,26], and the newly appeared peaks are attributed to the $n\rightarrow\pi^*$ transition of the C=S group. The observed UV/vis spectral change accompanied an isosbestic point at 280 nm up to 13 min, suggesting that a single photoreaction proceeded within the timescale. On the other hand, the absorption at the longer wavelength turned to decrease by the prolonged irradiation, suggesting that the formed C=S chromophore was lost due to some side reactions such as desulfurization as observed with the analogous photo-isomerization of alkylthio-

Fig. 2. UV/vis spectral change of TBT in PMMA film under 254 nm irradiation.

benzothiazole [23]. These results show that the photo-irradiation at 254 nm selectively induced the enol–keto isomerization of the thioamide group in TBT to an extent within the proper irradiation time.

The structural change along with the photoreaction of TBT was investigated in more detail by FT-IR spectroscopy (Fig. 3). Herein, the TBT concentration in the PMMA matrix was set to be higher (43 wt%) than the UV/vis study (20 wt%) for the clearness of the spectra. The TBT film was prepared on a KBr substrate and irradiated at 254 nm (1.12 mW/cm^2) for 13 min. The peak of the C=N stretching of the triazine ring at 1477 cm^{-1} significantly decreased during the irradiation, further supporting the proceeding of the enol– keto isomerization reaction. The decrease of the C–S peak at 838 cm^{-1} also supported the

Fig. 1. DSC profile of TBT (10 °C/min, 1st heating, under N$_2$ flow).
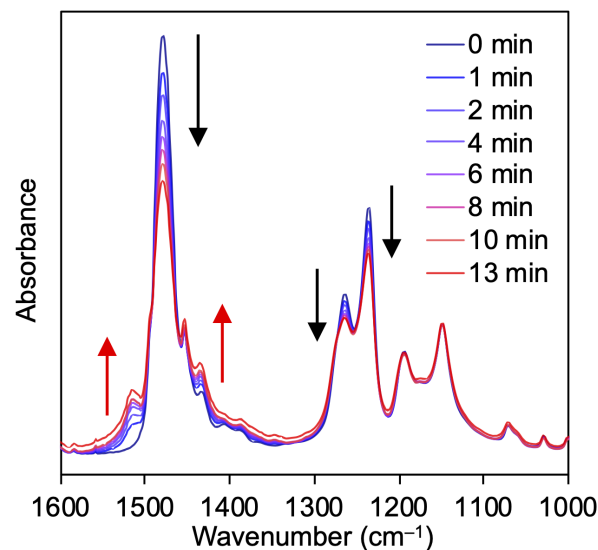
Fig. 3. FT-IR spectral change of TBT in PMMA film under 254 nm irradiation.

isomerization reaction. Meanwhile, there were observed several new peaks and absorption increase after the irradiation, which are attributed to the photo-isomerization products.

3.3. Detailed analysis of the FT-IR and UV/vis spectra with DFT calculation

To characterize these spectral changes, the FT-IR spectra of TBT and its three possible triazine-thione isomers were simulated by density functional theory (DFT) calculation at B3LYP/6-311+G(d,p) level. The calculated UV/vis spectrum of TBT (Fig. 4, left column, black line) well reproduced the experimental one with a peak top at 265 nm (calcd.: 264 nm). Among the calculated UV/vis spectra of the three possible isomerization products, the one of the monothione isomer with its peak top at 293 nm and 345 nm was the most comparable to the experimentally observed absorption increases at 288 nm and 336 nm during the photo-irradiation of TBT. We next

carried out the DFT study on the FT-IR spectra. The spectrum of TBT was again reproduced well with the deviation less than 11 cm^{-1} (Fig. 4, right column, black line) with the scaling factor of 0.983 [27]. Consistent to the previously described DFT study on the UV/vis spectra, the most apparent absorption increases observed at 1510 and 1434 cm^{-1} in the experiment were reproduced by the calculated spectrum of the monothione isomer, which shows the C=N stretching peak at 1535 cm^{-1} and C–N at 1441 cm^{-1}. On the other hand, a little increase observed around 1390 cm^{-1} in the experiment corresponded not to the monothione but to the dithione and trithione with the S=C–N vibration, suggesting the little formation of these isomers in addition to the monothione. The overall reaction ratio was calculated to be 28% from the decrease ratio of the C–S stretching peak at 838 cm^{-1}, which is attributed only to TBT according to the DFT calculation. Based on these results, it was concluded that the photoreaction of TBT mainly
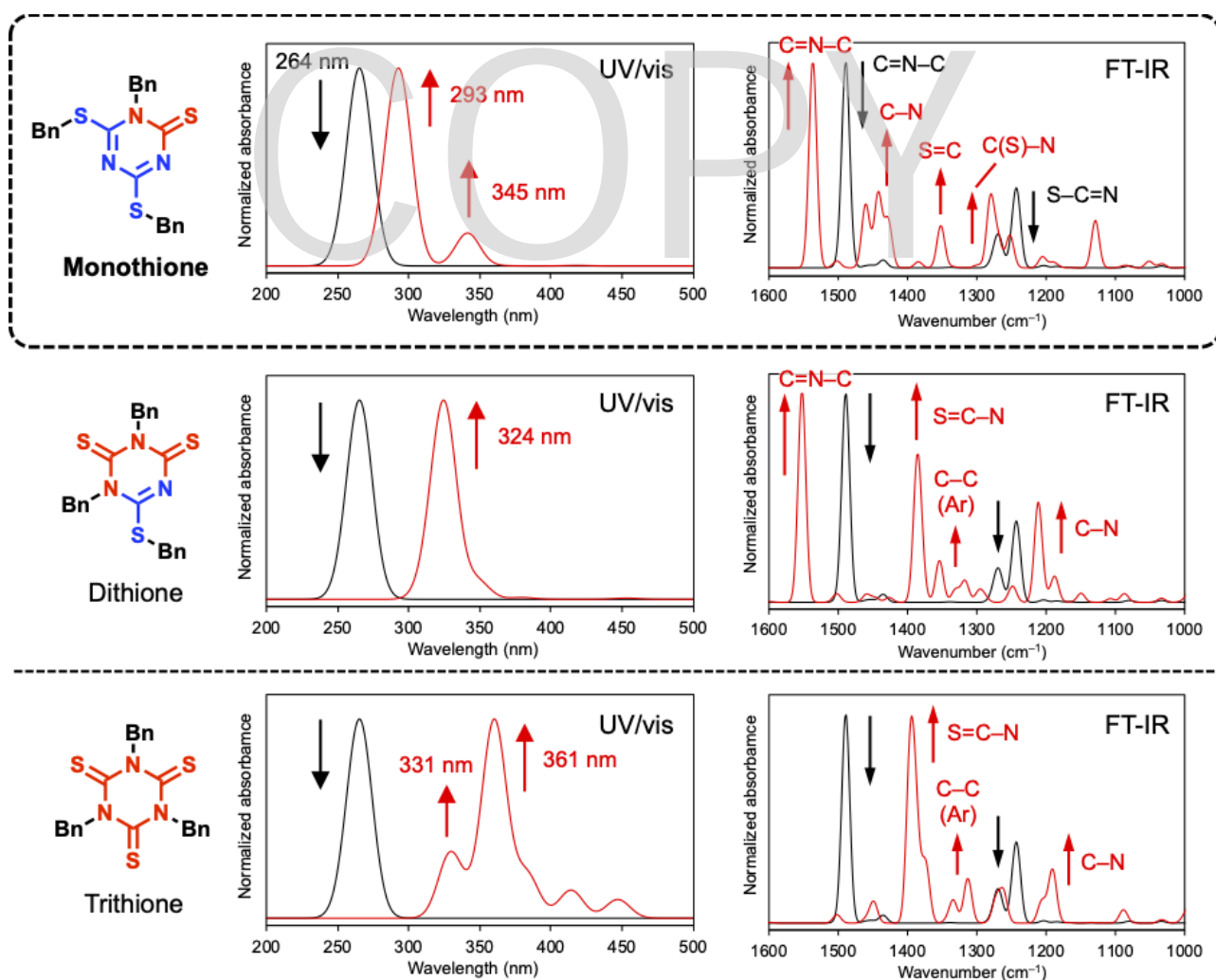
Fig. 4. Calculated UV/vis and FT-IR spectra before (black line) and after (red line) the photo-isomerization of TBT to either of its three possible thione isomers given by DFT calculation at B3LYP/6-311+G(d,p) level.
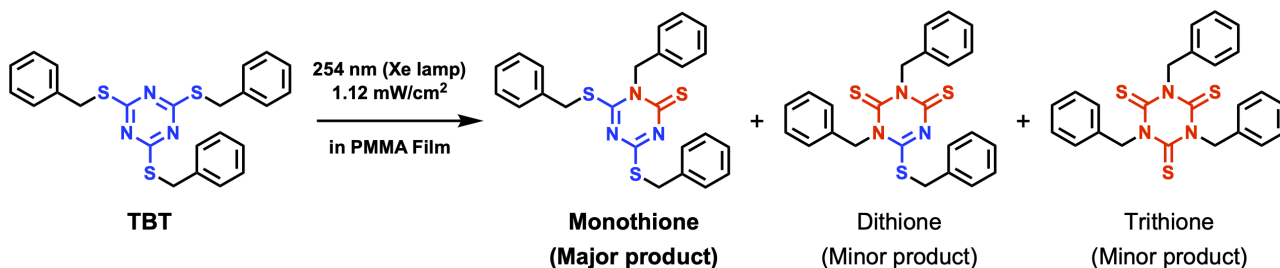
Scheme 2. Photoreaction of TBT under 254 nm irradiation in PMMA film.

afforded the monothione isomer while the further isomerization to the dithione and trithione also partially proceeded in the herein employed conditions (Scheme 2).

3.4. Investigation of photo-induced refractive index change by the photo-isomerization of TBT

The refractive index change along with the photo-isomerization of TBT was investigated with ellipsometry. TBT film with PMMA matrix (TBT: 20 wt%) was prepared on a Si plate with the thickness of *ca.* 0.1 μm and irradiated at 254 nm. The ellipsometry showed the increase of refractive index from 1.5876 to 1.5926 (Δn = + 0.0050) after 180 sec. The observed refractive index increase would be attributed to the formation of polar C=S functionality to increase the refractive index as has been observed in our previous study [24]. We also observed a little decrease of the film thickness from 1.04 nm to 0.999 nm (4% decrease), suggesting the decrease of *V* of the film which contributes to the refractive index increase according to the Lorentz–Lorenz equation (1).

4. Conclusion

We investigated the photo-isomerization reaction of TBT molecule for the first time. TBT showed good thermal stability for its isomerization reaction up to 200 °C in contrast to the previously reported 2-(benzoylthio)benzoxazole analogue. UV/vis and FT-IR spectroscopy of the TBT film in PMMA matrix revealed the enol-keto isomerization at one benzylthio moiety in TBT under 254 nm irradiation, which was supported by a detailed analysis using DFT calculation. Ellipsometry of the TBT films before and after the 254 nm irradiation revealed the refractive index increase of +0.0050 through the photo-isomerization reaction. Herein obtained knowledge would contribute to the development of novel optical materials with modulable refractive index based on thiotriazine structures with high molar refraction.

References

1. H. Ma, A. K.-Y. Jen, and L. R. Dalton, *Adv. Mater.*, **14** (2002) 1339.
2. T. Kada, A. Obara, and K. Kiso, *J. Appl. Phys.*, **87** (2000) 638.
3. K. Tanaka, H. Shiraishi, E. Takayanagi, A. Korechika, T. Igarashi, and T. Sakurai, *J. Photochem. Photobiol. A*, **174** (2005) 199.
4. K. Tanaka, M. Fukuda, T. Igarashi, T. Sakurai, *Polym. J.*, **10** (2005) 776.
5. S. Murase, K. Kinoshita, K. Horie, and S. Miyamoto, *Macromolecules*, **30** (1997) 8088.
6. Y. Kato, H. Muta, S. Takahashi, K. Horie, and T. Nagai, *Polym. J.*, **33** (2001) 868.
7. H. Kudo, W. Ueda, K. Sejimo, K. Mitani, T. Nishikubo, and T. Anada, *Bull. Chem. Soc. Jpn.*, **77** (2004) 1415.
8. H. Kudo, M. Yamamoto, and T. Nishikubo, *Macromolecules*, **39** (2006) 1759.
9. G. Langer, T. Kavc, W. Kern, G. Kranzelbinder, and E. Toussaere, *Macromol. Chem. Phys.*, **202** (2001) 3459.
10. U. Daschiel, T. Höfler, G. Jakopic, V. Schmidt, and W. Kern, *Macromol. Chem. Phys.*, **208** (2007) 1190.
11. T. Höfler, T. Grießer, X. Gstrein, G. Trimmel, G. Jakopic, and W. Kern, *Polymer*, **48** (2007) 1930.
12. T. Griesser, T. Höfler, G. Jakopic, M. Belzik, W. Kern, and G. Trimmel, *J. Mater. Chem.*, **19** (2009) 4557.
13. T. Köpplmayr, M. Cardinale, G. Jakopic, G. Trimmel, W. Kern, and T. Griesser, *J. Mater. Chem.*, **21** (2011) 2965.
14. M. Edler, S. Mayrbrugger, A. Fian, G. Trimmel, S. Radl, W. Kern, and T. Griesser, *J. Mater. Chem. C*, **1** (2013) 3931.
15. T. Griesser, J.–C. Kuhlmann, M. Wieser, W. Kern, and G. Trimmel, *Macromolecules*, **42** (2009) 725.
16. A. Takahashi, T. Watanabe, S. Ando, and A. Kameyama, *J. Photopolym. Sci. Technol.*, **32** (2019) 243.

17. G. H. Meeten, "*Optical Properties of Polymers*", Elsevier Applied Science, London, 1989.

18. J. Liu and M. Ueda, *J. Mater. Chem.*, **19** (2009) 8907.

19. N. Nishimura, Y. Shibasaki, M. Ozawa, and Y. Ohishi, *J. Photopolym. Sci. Technol.*, **25** (2012) 355.

20. S. Shi, Y. Onodera, T. Tsukamono, Y. Shibasaki, and Y. Ohishi, *J. Photopolym. Sci. Technol.*, **34** (2021) 251.

21. K. Tsuchiya, Y. Ishida, T. Higashihara, A. Kameyama, and M. Ueda, *Chem. Lett.*, **44** (2015) 1110.

22. B. F. Hanley, *Mater. Today Commun.*, **25** (2020) 101644.

23. A. Gáplovský, R. Hercek, and P. Kuráň, *Chem. Pap.*, **55** (2001) 45.

24. M. Miyasaka, A. Higurashi, and A. Kameyama, *Chem. Lett.*, **40** (2011) 1363.

25. S. Koodanjeri, A. R. Pradhan, L. S. Kaanumalle, and V. Ramamurthy, *Tetrahedron Lett.*, **44** (2003) 3207.

26. M. Yamato, Y. Takeuchi, K. Hashigaki, K. Hattori, E. Muroga, and T. Hirota, *Chem. Pharm. Bull.*, **31** (1983) 1733.

27. M. Prabhaharan, A. R. Prabakaran, S. Srinivasan, and S. Gunasekaran, *Spectrochim. Acta A Mol. Biomol. Spectrosc.*, **138** (2015) 711.

Networked Polyphthalaldehydes Linked with Oxime Ether and Urethane Units and Their Photo-induced Depolymerization

Kanji Suyama[1*], Hirokazu Hayashi[2], and Hideki Tachi[3]

[1]*Faculty of Liberal Arts, Sciences and Global Education, Osaka Metropolitan University,*
1-1 Gakuencho, Nakaku, Sakai, Osaka 599-8531, Japan
[2]*Research Division of Applied Material Chemistry, Izumi Center, Osaka Research Institute of*
Industrial Science and Technology (ORIST),
[3]*Research Division of Polymer Functional Materials, Izumi Center, Osaka Research Institute of*
Industrial Science and Technology (ORIST),
7-1 Ayumino-2, Izumi, Osaka 594-1157, Japan
**suyamakanji@omu.ac.jp*

Photo-induced depolymerization is a useful technique in designing functional materials and polymer recycling.   Polyphthalaldehyde (PPA) has been known to be depolymerizable even in solid state.   In this study, networked PPAs linked with oxime ether and urethane units have been prepared, and their photo-induced depolymerization was attempted.   The networked structure of PPAs was prepared by anionic polymerization of phthalaldehyde monomer (*o*-PA) initiated with trifunctional oxime and 1,8-diazabicyclo[5.4.0]undec-7-ene to form truxene core bearing three PPA chains, followed by termination with difunctional isocyanates.   We could obtain networked PPAs from 1,5-naphthalene diisocyanate, although could not from hexamethylene diisocyanate.   Obtained networked polymers were pressed in neat pellets and UV-irradiated with Hg-Xe lamp (>310 nm).   By repeated irradiation in solid state and dispersed state in chloroform, almost of the PPAs became soluble in chloroform.   In ^{1}H NMR spectra of the soluble fractions, peaks due to *o*-PA and phthalide were observed, suggesting the proceeding of almost complete decrosslinking and depolymerization.   Trace amount of insoluble powder finally remained and discussed based on its IR spectrum.   We also compared the scanning microscope images of PPAs before and after irradiation.

Keywords: Polyphthalaldehyde, Anionic polymerization, Photo-degradation, Isocyanate, Depolymerization, Networked polymer

1. Introduction

Controlled degradation of polymers provides many approaches in polymer recycling and functional materials [1,2].   Polyphthalaldehyde (PPA) is a well-known polymer that can be degradable by heat, acid, and photo-irradiation even in solid state [3].   Due to their excellent degradability, PPAs have been utilized as a thermal sacrificial layer [4], and photoresists for laser beam lithography [5] and EUV [6-8] recently.

PPAs are obtained by both cationic and anionic polymerization.   While the former often leads to the formation of cyclic PPAs, the latter affords linear chains whose terminals contain fragments of initiator and terminator.   Thus, easy introduction

of desired functional groups into the PPAs is possible by anionic polymerization [3].   Several attempts have been reported to introduce terminals that can trigger the depolymerization of PPA chains [6,9,10].   Crosslinked PPAs have also been proposed as copolymers of PPA bearing allyl group with stimuli-responsible endcaps, and their depolymerization has been demonstrated [11].

We have already explored the preparation and photoreaction of PPAs with oxime ether terminals [12-14].   In these studies, we have accomplished the photolysis of oxime ether units and following depolymerization [12], the introduction of methacryl units by terminating with methacryloyloxyethylisocyanate [13], and the
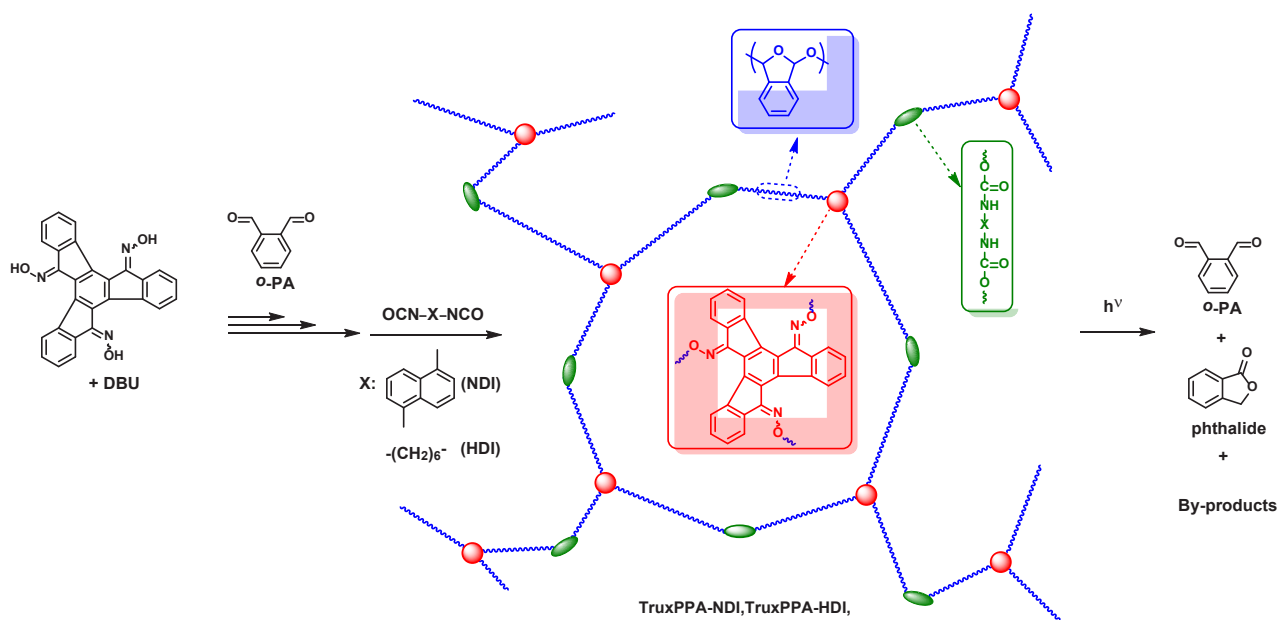
Fig. 1. Preparation and photo-induced degradation of networked PPAs in this work.

formation and photodegradation of polymers bearing two and three PPA chains [14].

Based on the above results, this paper describes the preparation and photodegradation of networked PPAs as shown in Fig. 1. Herein the networked structure was obtained by the anionic polymerization of phthalaldehyde (*o*-PA) initiated with truxenone trioxime and terminated with molecular diisocyanates. Resulting polymers would be composed of long PPA chains linked with short oxime ether and urethane units, and most of the networked structure can be degraded into small molecules.

2. Experimental
2.1. General

IR and UV spectra were recorded on Jasco FT-IR4200, and UV630 spectrometers, respectively. NMR spectra were measured by a JEOL JNM-ECX400 spectrometer.

Truxenone trioxime was obtained as described previously [15]. 1,5-Naphthalene diisocyanate (NDI) was obtained from Tokyo Chemical Industry and recrystallized from toluene / hexane mixture. *o*-PA was obtained from Nacalai Tesque (Kyoto, Japan) as SP grade for fluorometry, recrystallized grade. Dehydrated grade of dichloromethane and pyridine were received from Nacalai and Wako, Chemical (Osaka, Japan), respectively, and used for polymerization reactions. Hexamethylene diisocyanate (HDI) was used as received from Nacalai.

2.2. Polymerization

Typical polymerization was carried out as follows under yellow light: in a flask, 960 mg (7.16 mmol) of *o*-PA was placed, and the flask was purged with argon gas after equipment of a three-way cock with a septum and a balloon. Then, 5 mL of argon-purged CH_2Cl_2 was added through a syringe to the flask and cooled to −80 °C in an aluminum block cryostat PSL-2500 A (EYELA, Tokyo, Japan). In other flask, truxenone trioxime and 1,8-diazabicyclo[5.4.0]undec-7-ene (DBU) were dissolved in toluene and pyridine and rotavapped under reduced pressure. The flask was equipped with a septum, purged with argon, and added 0.05 mL of pyridine and 1.0 mL of CH_2Cl_2. Then, 0.5 mL of the oxime solution was taken out with a syringe, added to the monomer solution, and kept stirring at −80 °C for 30 min. The polymerization was quenched by adding a CH_2Cl_2 solution containing a diisocyanate, and the flask was taken out from the cryostat bath. After a given time, the mixture was once rotavapped, added 50 mL of methanol, and filtered. Obtained powder was reprecipitated from methanol after dissolving in chloroform, or just washed in chloroform.

2.3. Photo-irradiation of PPAs

Photo-irradiation was performed in air with a Hayashi Watch-Works LA410 Xe-Hg lamp (Tokyo, Japan) whose light intensity was 200 mW/cm^2 at 365 nm, which was measured by an Orc UV-M03 illuminometer (Tokyo, Japan). The solid samples were irradiated via 50 μm PET film to cut the shorter

wavelength light completely.

Neat polymer powder (ca. 6 mg) was pressed into to 5 mm$^\phi$ diameter pellets using a Jasco MP-1 hand press. KBr pellets containing PPAs were prepared by mixing PPA : KBr = 1 : 4 (wt/wt). The irradiation of powder in chloroform was performed in Pyrex 5 mm$^\phi$ NMR tubes.

Scanning electron microscope (SEM) was performed with a Hitachi High-technologies Regulus 8230 FE-SEM at 10 keV. As a pretreatment, samples were fixed to conductive carbon adhesive tape, and platinum deposition was performed at 10 mA for 90 s.

3. Results and discussion

3.1. Preparation of PPA networks

PPAs were prepared by anionic polymerization of *o*-PA and terminated with difunctional isocyanates to form networked structure. In a similar polymerization condition, we have already obtained three-PPA armed star polymer of 12.3 kDa of number average molecular weight in 15 % conversion after separation of two-armed PPAs using a recycle SEC system [14]. Because we did not remove in the present study, obtained polymers would involve the two-armed PPAs. Table 1 summarizes the polymerization conditions and conversion in this study. All PPAs were light tan colored due to truxene core. When the polymerization was terminated with NDI, the reaction mixture became gelatinous immediately (entries 1, 2). After the flask was taken out from the cold bath and warmed to room temperature, the mixture became homogeneous solutions. During stirring at ambient temperature, precipitates began to deposit gradually, and finally the mixture became slurry. Finally, 120 and 46 mg of insoluble

fractions in chloroform were obtained in entries 1 and 2, respectively. These results clearly show the proceeding of crosslinking by NDI to form
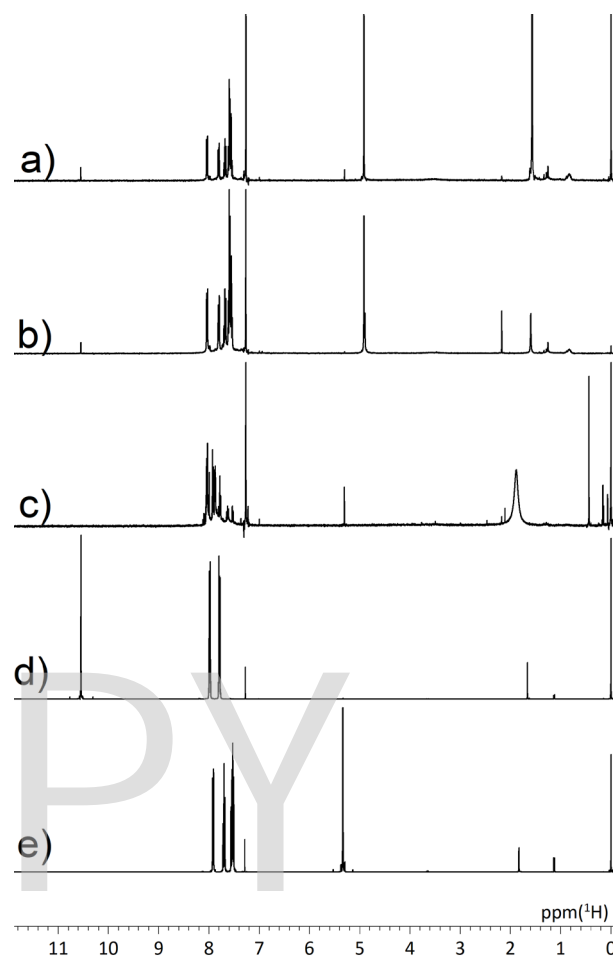
Fig. 2. ^{1}H NMR (CDCl$_3$) spectra of soluble fraction recovered from irradiated TruxPPA-NDI and related molecules. After irradiation for a) 3 h in neat pellet, b) 4 h in KBr, and c) 6 h in neat pellet and 9 h in CDCl$_3$. Authentic samples of d) *o*-PA and e) phthalide.

Table 1. Polymerization condition[a] and conversion of PPAs.

Entry	Abbreviation	Diiso-cyanate	Trioxime / *o*-PA / diisocyanate in feed (mmol)	Time after polymerization[c]	Recovered polymer (mg)[d]	Insoluble fraction[f] (mg)
1	TruxPPA-NDI	NDI	0.099 / 7.16 / 0.411	7 d	-[e]	120
2		NDI	0.031 / 7.16 / 0.137	7 d	-[e]	46
3	TruxPPA-HDI	HDI	0.093 / 7.16 / 0.207	7 d	563	0
4		HDI	0.031 / 7.16 / 0.074	7 d	342	0
5		HDI	0.093 / 7.16 / 0.207 × 2 [b]	48 h	493	0
6		HDI	0.032 / 7.16 / 0.076 × 2 [b]	48 h	413	0

a) Polymerization in 5 mL of CH$_2$Cl$_2$ at −80 °C for 30 min. DBU : trioxime = 1 : 1 (mol/mol) .

b) After the first addition of HDI, the mixture was stirred for 40 min at ambient temperature, condensed to ~ 1 mL under reduced pressure, and added HDI solution again.

c) After diisocyanate addition at room temperature.

d) After reprecipitation from chloroform / methanol system.

e) Not measured.

f) In chloroform.

networked structure.

However, we could not obtain insoluble fraction from HDI (entries 3-6). In these cases, the formation of gelatinous material was not observed after addition of HDI. Additional reaction of HDI in condensed condition was also ineffective (entries 5 and 6). The difference might be due the lower reactivity of aliphatic isocyanates compared to aromatic ones, as often observed in many addition reactions of isocyanates [16].

3.2. Photoreactions of PPAs

We have attempted to irradiated a PPA terminated with NDI (TruxPPA-NDI, entry 1 in Table 1) in the form of pressed pellets (5 mm$^\phi$). After irradiation for 3 h with Hg-Xe lamp in air, the pellets were soaked in CDCl$_3$, and 43 wt% was recovered as insoluble powder. ^{1}H NMR spectrum of soluble fraction is shown in Fig. 2a, where no broad band due to PPA remains, and peaks assignable to *o*-PA and phthalide are found. It is known that UV irradiation of *o*-PA leads to the formation of both phthalide and its dimer depending on the solvent in varying yield ratio, and the former is preferential in chlorinated solvents [17,18]. These results indicated that partly decrosslinking and depolymerization for TruxPPA-NDI proceeded in solid state. The surface morphology changes of TruxPPA-NDI powder on irradiation in Fig. 3 was consistent with the degradation behavior, where sharpness of powder edge reduced on irradiation.

In the next step, we irradiated TruxPPA-NDI dispersed in KBr pellets to penetrate more light. During the irradiation, IR spectral changes of the pellet are shown in Fig. 4a, where remarkable increase is found at 1770, 1470, 1440 cm^{-1} assignable to phthalide. Similar increase in the peak at 1770 cm^{-1} is also shown for TruxPPA-HDI (entry 3 in Table 1) as shown in Fig. 4b. After irradiation for 4 h, the KBr pellets were soaked into D$_2$O and extracted in CDCl$_3$. Although soluble fraction involved peaks due to *o*-PA and phthalide as shown in Fig. 2b, insoluble fraction in both D$_2$O and CDCl$_3$ remained, suggesting insufficient degradation of networked structure.
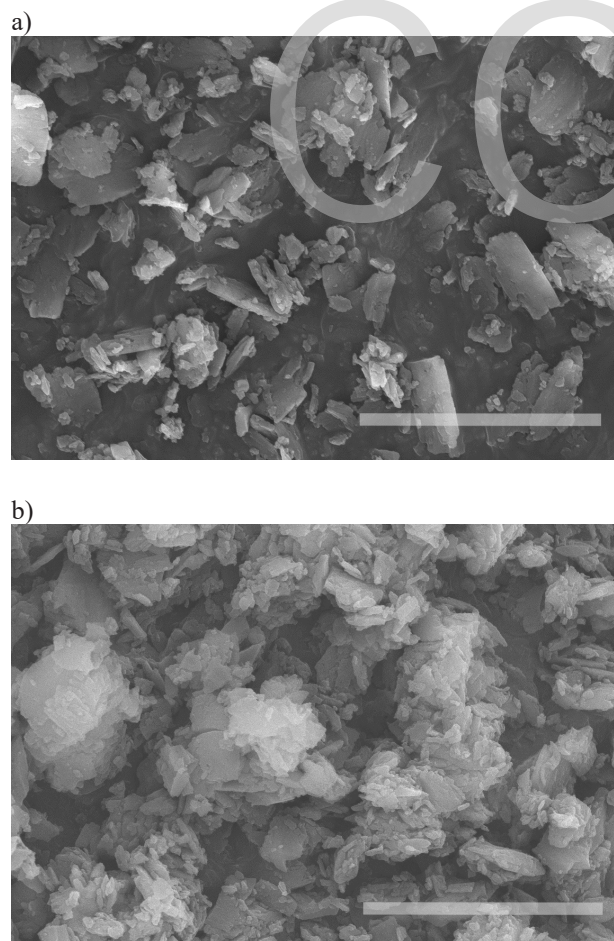
Fig. 3. SEM images of TruxPPA-NDI a) before and b) after irradiation for 5 h. Scale bars: 5 μm.
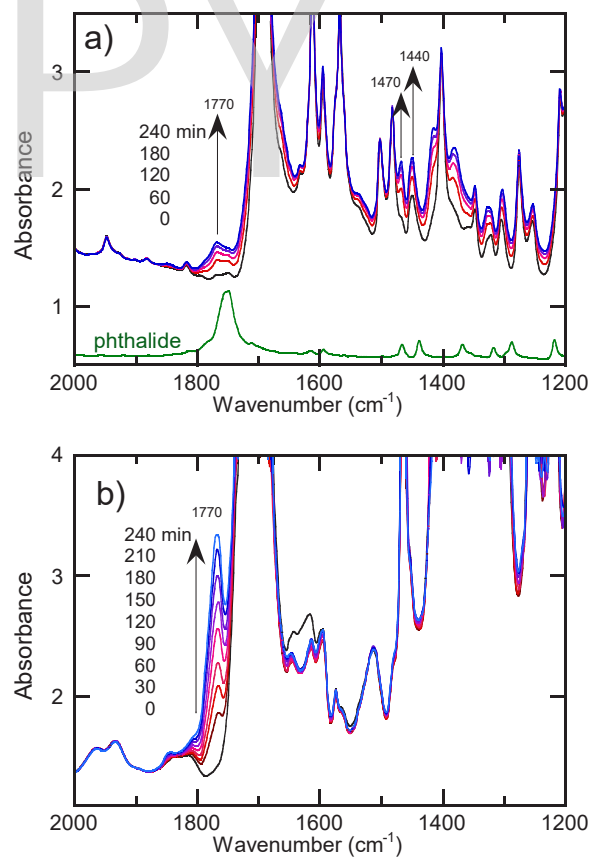
Fig. 4. IR spectral changes of a) TruxPPA-NDI (KBr) with authentic phthalide, and b) TruxPPA-HDI (neat) on irradiation. Numbers in the figures show total irradiation time and wavenumbers of peak tops.

The above behavior of solubility and changes in spectral and SEM was almost identical for another PPA terminated with NDI (entry 2 in Table 1), which will have longer PPA chains than that in entry 1. These results show that the effect of PPA chain length was not observed in this study.

In order to accomplish the entire degradation of TruxPPA-NDI, we tried to continue the irradiation for longer time in solid and solvent. Three neat PPA pellets were irradiated for 3 h, soaked in CHCl₃. Then, recovered insoluble powder was pressed in two pellets, irradiated for additional 3 h, and soaked in CHCl₃. The weight of the insoluble fraction was 22 wt% against the starting PPA. Then, the insoluble powder was dispersed in CDCl₃ and irradiated in a 5 mm$^\phi$ NMR tube for 9 h to afford trace amount of dark brown powder. As shown in Fig. 2c, the soluble fraction afforded similar ^{1}H NMR spectrum to Figs. 2a and 2b, suggesting the
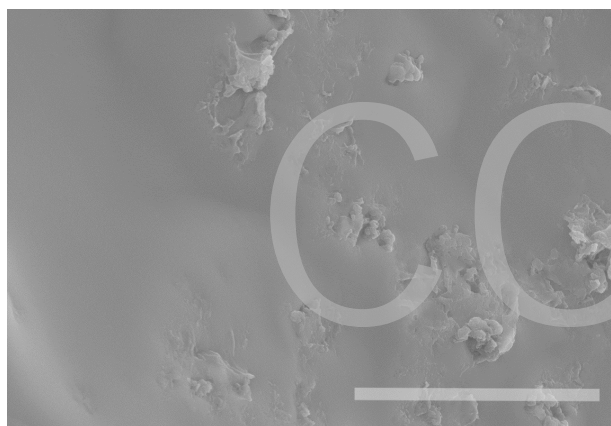
Fig. 5. SEM image of insoluble powder obtained from TruxPPA-NDI after irradiation for 6 h in neat pellet and 9 h in CDCl₃. Scale bar: 5 μm.
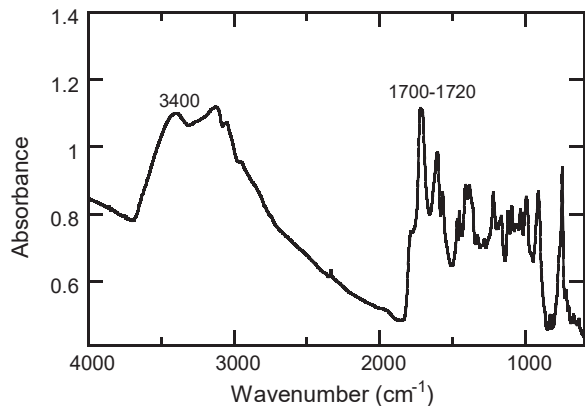
Fig. 6. IR spectrum (KBr) of insoluble powder obtained from TruxPPA-HDI after irradiation for 6 h in neat pellet and 9 h in CDCl₃. Numbers in the figures show wavenumbers of peak tops.
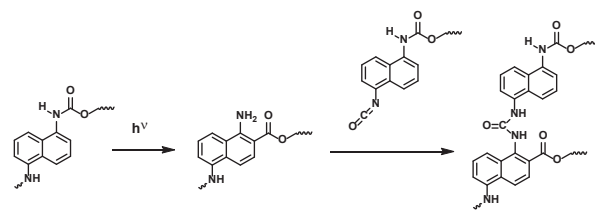
Scheme 1. Photo-Fries rearrangement and plausible further reaction with unreacted isocyanato end groups.

formation of phthalide or its further reaction products such as dimer.

Considering that no such insoluble fraction was observed for non-crosslinked PPAs initiated from truxenone trioxime [14], the insoluble powder would be attributed to naphthalene diisocyanate units. Figure 5 shows SEM images of the insoluble polymer whose surface morphology was different from PPA before irradiation. For aromatic urethane unit, the proceeding of photo-Fries rearrangement is often observed [19-22]. Plausible photoreaction is seen as shown in Scheme 1, where resulting aromatic amino groups can react with unreacted isocyanato groups to form new covalent bonds. IR spectrum of the final insoluble powder from TruxPPA-NDI in Fig. 6 is consistent with the formation of aromatic ester and urea units, where peaks due to N-H and C=O stretching bands around 3400 and 1700-1720 cm^{-1}, respectively, appeared.

4. Conclusions

We have polymerized *o*-PA initiated with truxenone trioxime and DBU, and terminated with diisocyanates. When terminated with NDI, resulting TruxPPA-NDI afforded insoluble fractions and succeeded in the formation of networked structure, although TruxPPA-HDI did not. TruxPPA-NDI was irradiated in solid state and in chloroform, and almost became soluble in chloroform, suggesting the proceeding of almost complete decrosslinking and depolymerization. ^{1}H NMR and IR spectral changes supported the depolymerization. The effect of PPA chain length was not observed in this study. Trace amount of insoluble powder would be attributed to NDI units.

References

1. T. Chen, H. Wang, Y. Chu, C. Boyer, J. Liu, and J. Xu, *ChemPhotoChem.*, **3** (2019) 1059.

2. R. E. Yardley, A. R. Kenaree, and E. R. Gillies, *Macromolecules*, **52** (2019) 6342.
3. F. Wang and C. E. Diesendruck, *Macromol. Rapid Commun.*, **39** (2018) 1700519.
4. M. Garg, A. C. Ladd, J. E. Aw, X. Zhang, and N. R. Sottos, *ACS Appl. Polym. Mater.*, **4** (2022) 479.
5. A. Kafri, D. Dutta, S. Mukherjee, P. K. Mohapatra, A. Ismach, and E. Koren, *ACS Appl. Mater. Interfaces*, **13** (2021) 5399.
6. J. Deng, S. Bailey, R. Ai, A. Delmonico, G. Denbeaux, S. Jiang, and C. K. Ober, *ACS Macro Lett*., **11** (2022) 1049.
7. J. Deng, S. Bailey, S. Jiang, and C. K. Ober, *Chem. Mater.*, **34** (2022) 6170.
8. J. Deng, S. Bailey, S. Jiang, and C. K. Ober, *J. Am. Chem. Soc*., **144** (2022) 19508.
9. W. Seo and S. T. Phillips, *J. Am. Chem. Soc*., **132** (2010) 9234.
10. A. M. DiLauro, J. S. Robbins, and S. T. Phillips, *Macromolecules*, **46** (2013) 2963.
11. S. Soars, J. Kamps, B. Fairbanks, and C. Bowman, *Macromol. Chem. Phys*, **222** (2021) 2100111.
12. H. Hayashi, H. Tachi, and K. Suyama, *J. Photopolym. Sci. Technol*., **33** (2020) 269.
13. H. Hayashi, H. Tachi, and K. Suyama, *J. Photopolym. Sci. Technol*., **34** (2021) 219.
14. K. Suyama, H. Hayashi, and H. Tachi, *J. Photopolym. Sci. Technol*., **35** (2022) 171.
15. K. Suyama and H. Tachi, *J. Photopolym. Sci. Technol*., **30** (2017) 247.
16. E. Delebecq, J. -P. Pascault, B. Boutevin, and F. Ganachaud, *Chem. Rev.*, **113** (2013) 80.
17. J. Kagan, *Tetrahedron Lett.*, **49** (1966) 6097.
18. J. C. Scaiano, M. V. Encinas, and M. V. George *J. Chem. Soc. Perkin II*, **1980** (1980) 724.
19. K. Schwetlick, J. Stumpe, and R. Noack, *Tetrahedron* **35** (1979) 63.
20. C. Wilhelm, A. Rivaton, and J. -L. Gardette, *Polymer*, **39** (1998) 1223.
21. A. Takahashi, T. Watanabe, S. Ando, and A. Kameyama, *J. Photopolym. Sci. Technol*., **32** (2019) 243.
22. F. Xie, T. Zhang, P. Bryant, V. Kurusingal, J. M. Colwell, and B. Laycock, *Prog. Polym. Sci.*, **90** (2019) 211.

Communication

Synthesis of Pyrene-Substituted Azobenzene Derivatives and Their Assembly into Flat Structures for Stimuli-Induced Switching

Pyae Thu[1,2] and Mina Han[1]*

[1]Department of Chemistry Education, [2]Department of Chemistry,
Kongju National University, 56 Gongjudaehak-ro, Gongju-si, Chungnam 32588, Korea
*hanmin@kongju.ac.kr

We report the design of pyrene-substituted azobenzene chromophores and their assembly into flat aggregates capable of repeated switching of their absorption and emission properties in response to light and heat. The introduction of a relatively longer butoxy linker between the pyrene and azobenzene (AzBuPy) resulted in the production of more than 90% of *cis*-azobenzene at the photostationary state of ultraviolet (UV) light, as determined by UV-visible absorption and ^{1}H NMR spectral data. Flat petal-shaped micrometer-sized structures formed in highly polar DMF-H$_2$O mixtures did not experience severe disassembly even after sufficient UV light irradiation, and showed excellent photoswitching performance. In addition, we investigated light and heat responses of DPA@AzBuPy aggregates assembled from hydrophobic fluorophore (9,10-diphenylanthracene: DPA) and AzBuPy mixtures.
Keywords: Molecular assembly, Pyrene-substituted azobenzene chromophores, Repeated switching, Stimuli-responsive

1. Introduction

External stimuli-responsive fluorescent materials are of great interest because of their promising utilization in optoelectronic devices, sensors, photopatterning, biomedical delivery, and therapy systems [1-13]. A number of studies have been reported on the design of organic, inorganic, and organic-inorganic hybrid systems that respond to external or internal stimuli such as light, heat, force, magnet, electricity, specific chemicals, etc [5,14-22]. For instance, chemical combination of photochromic compounds and organic fluorophores can be extended to the development of photoluminescent organic materials capable of responding to various stimuli (such as light wavelength, temperature, etc) [23-28]. In particular, photochromic compounds, which are sensitive to light and heat, such as diarylethene, spiropyran, fulgide, stilbene, spirooxazine, and azobenzene are good candidates for repeatedly photoswitchable nano-, micro- and macro-scale systems [29-35].

To develop light-responsive self-assembled nano/microstructures that involve light-induced structural transformation of constituent molecules and resulting changes in color and emission characteristics, we recently introduced a new type of chromophore in which azobenzene and pyrene units are linked by a short methoxy linker (AzMePy, Fig. 1 and Table 1) [36]. The chromopohore exhibited aggregation-induced emission enhancement (AIE/AIEE) characteristics and underwent repeated *trans↔cis* isomerization in dilute solutions, while the formation of self-assembled micrometer-sized sheets significantly inhibited their light response ability.

To resolve this problem, we have attempted to synthesize pyrene-substituted azobenzene derivatives capable of excellent repeated photoswitching in assembled states as well as in dilute solutions. AzBuPy, in which a longer butoxy linker is introduced between azobenzene and pyrene moieties (Scheme 1), was converted to >90% of the *cis* form upon ultraviolet (UV) light irradiation. Alternating irradiation with UV and visible light gave rise to reversible changes in the absorption (color) and emission spectra of AzBuPy DMF-H$_2$O
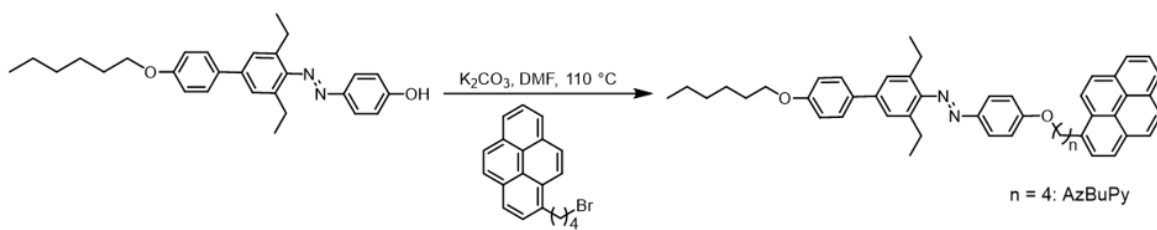
Scheme 1. Synthesis
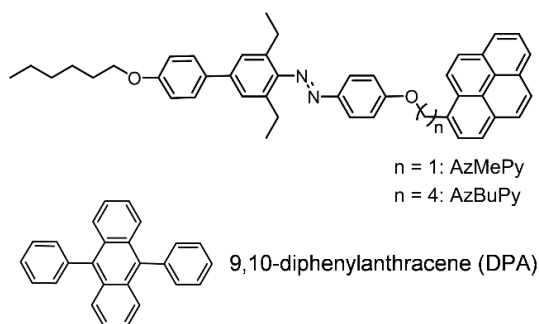
Fig. 1. Chemical structures

mixtures containing flat petal-shaped aggregates. Furthermore, light and heat responses of the assembled aggregates (DPA@AzBuPy) obtained from mixtures of hydrophobic fluorophore (9,10-diphenylanthracene: DPA) and pyrene-substituted azobenzene dye (AzBuPy) were examined.

2. Experimental
2.1. Synthesis

The precursor (AzOH) (0.11 g, 0.26 mmol), which was dissolved in N,N-dimethylformamide (DMF, 15 mL), was reacted with 1-bromobutylpyrene (0.15 g, 0.43 mmol) in the presence of K_2CO_3 (0.11 g, 0.77 mmol). The reaction proceeded at 110 °C for 24 h and the mixture was cooled to room temperature. Chloroform and water were added and the collected residue was purified by silica gel column chromatography (*n*-hexane:chloroform, *v/v* = 1/3).

(0.10 g, yield: 63%). ¹H NMR (400 MHz, CDCl₃) δ 8.34 (d, 1H, Py*H*, J=9.27 Hz), 8.14-8.22 (m, 4H, Py*H*), 8.01-8.07 (m, 3H, Py*H*), 7.93 (t, 3H, Ar*H* and Py*H*), 7.59 (d, 2H, Ar*H*), 7.36 (s, 2H, Ar*H*), 7.03 (dd, 4H, Ar*H*, J= 18.2 Hz, J= 8.88 Hz), 4.15 (t, 2H, ArOC*H*₂(CH₂)₃Py), 4.04 (t, 2H, ArOC*H*₂(CH₂)₄CH₃), 3.49 (t, 2H, ArO(CH₂)₃C*H*₂Py), 2.78 (q, 4H, ArC*H*₂CH₃), 2.01-2.17 (m, 4H, ArOCH₂(C*H*₂)₂CH₂Py), 1.84 (quin, 2H, ArOCH₂C*H*₂(CH₂)₃CH₃), 1.52 (quin, 2H, ArO(CH₂)₂C*H*₂(CH₂)₂CH₃), 1.37-1.41 (m, 4H, ArO(CH₂)₃(C*H*₂)₂CH₃, 1.23 (t, 6H, ArCH₂C*H*₃), 0.950 (t, 3H, ArO(CH₂)₅C*H*₃. ¹³C NMR (400 MHz, CDCl₃) δ 161.6, 158.8, 149.9, 147.3, 140.3, 137.1, 136.4, 133.3, 131.5, 130.9, 129.9, 128.1, 127.5, 127.3, 127.2, 126.7, 125.9, 125.8, 124.9, 124.8, 124.7, 124.4, 123.4, 114.8, 114.7, 68.1, 33.2, 31.6, 29.3, 29.2, 28.2, 25.8, 25.5, 22.6, 15.7, 14.1. FAB-MS (*m/z*): [M+H]⁺ found, 687.3950 (=M+1), calcd for $C_{48}H_{51}N_2O_2$ = 687.3951.

2.2. Instrumentation

Spectroscopic grade DMF and ultrapure water purified to reach a minimum resistivity of 18.0 MΩ·cm (25 °C) using a Romax µPure HIQ water purification system (Hanam, Republic of Korea) were used for optical measurements. The prepared solution was placed in a quartz cell, purged for 30 s with nitrogen gas, and sealed with Parafilm® for further optical measurements. UV-visible absorption and emission spectroscopic

Table 1. Spectroscopic data and repeated photoswitching behaviors of AzBuPy and AzMePy in dilute solutions and in aggregated states.

Compound	Solvent	λ_{max}^{Abs} (nm)	λ_{max}^{Fluo} (nm)	Photoswitching
AzBuPy	DMF	315.0, 328.5, 344.5	377.5, 397.0, 418.5	○
	DMF-H₂O	322.0, 334.5, 351.5	377.5, 400.5, 420.5	○
AzMePy[36]	DMF	316.0, 329.5, 345.5	379.0, 398.0, 418.5, 460.5	○
	DMF-H₂O	339.0, 354.0	376.5, 396.0, 400–650	×

measurements were carried out with a Shimadzu UV-2600 UV-visible spectrophotometer and a Horiba FluoroMax-4 spectrofluorometer. Toshiba color filters, UV-35+UV-D36A and Y-43+V-44, were used to generate UV light (365 nm) and visible light (436 nm) combined with Supercure-204S, Tokina, for *trans*-to-*cis* and *cis*-to-*trans* photoisomerization experiments. ^{1}H and ^{13}C NMR spectroscopic measurements were performed with a Bruker 400 MHz NMR spectrometer. Field-emission scanning electron microscopy (FE-SEM) images were recorded using a TESKAN-MIRA3-LM microscope, after placing a few drops of turbid suspensions on a quartz (and glass) substrate and coating it with platinum layer in a Hitachi E-1030 ion sputtering system.

3. Results and Discussion

UV-visible absorption, ^{1}H NMR, and fluorescence spectroscopy measurements were performed to investigate the degree of *trans↔cis* molecular conformation changes caused by UV (365-nm) and blue (436-nm) light irradiation and the resulting spectroscopic information. Three intense absorption bands at 315.0, 328.5, and 344.5 nm correspond to the pyrene unit and a broad absorption band appearing in the 360-400 nm region is likely due to the π-π* transition of the typical azobenzene unit (Fig. 2a) [36-38]. Upon exposure of the AzBuPy DMF solution to UV light, a drastic reduction of the π–π* band near 370 nm was observed as a result of the *trans*-to-*cis* photoisomerization. Light irradiation for 150 seconds was sufficient to reach a *cis*-rich photostationary state. In addition, ^{1}H NMR spectral data taken before and after UV light irradiation revealed noticeable appearance of both doublet signals (δ 8.27, 7.13, 6.75 ppm) attributable to aromatic protons around the azo (−N=N−) group and multiplet signals (3.42, 2.38, 2.22 ppm) corresponding to protons attached to the alkyl group (Fig. 2b). The ratio of the *trans* to *cis* forms present in the photostationary state was estimated to be approximately 6/94, which was roughly consistent with that of the absorption spectral data. The dilute AzBuPy DMF (20 μM) solution displayed characteristic monomer emission in the 370–450 nm region, and no excimer-like emission was found
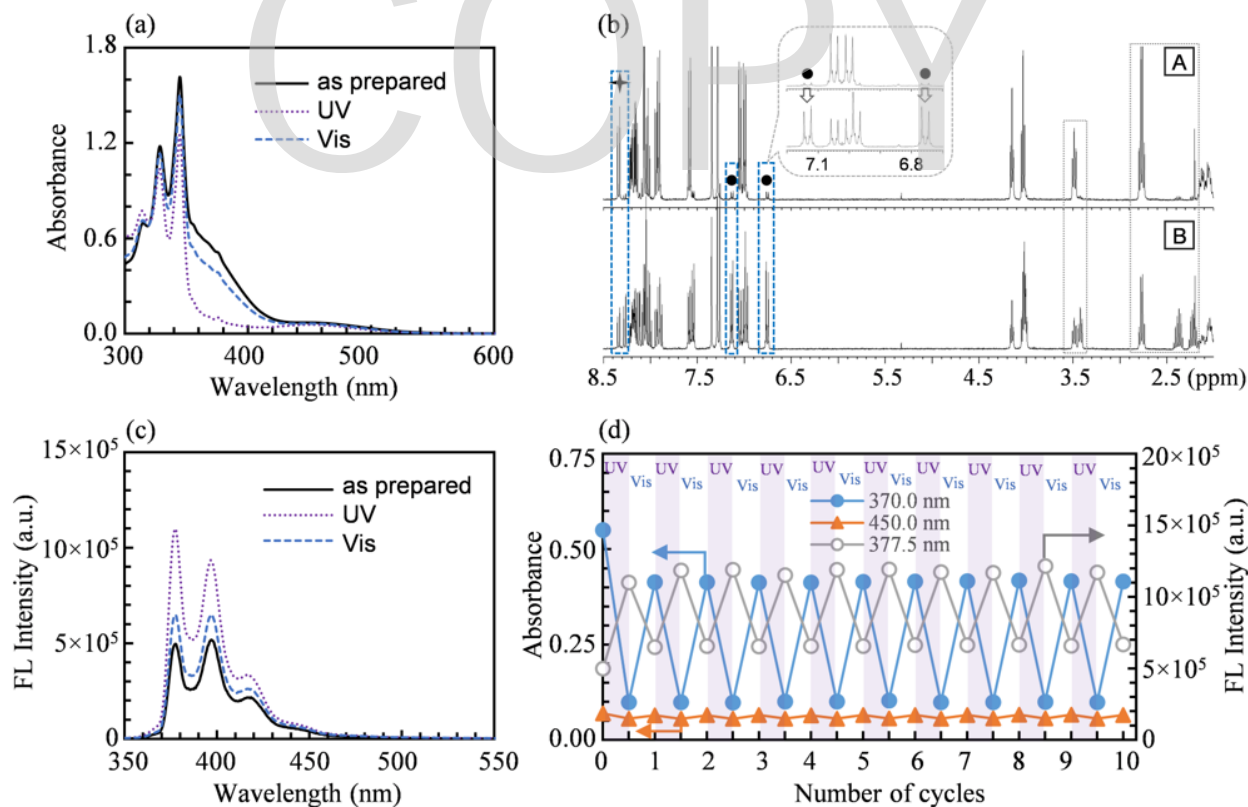
Fig. 2. (a) UV-visible absorption spectral changes of AzBuPy in 20 μM DMF upon UV (365 nm, ~1.1 mW/cm²) and subsequent visible (436 nm, ~1.1 mW/cm²) light irradiation. (b) ^{1}H NMR spectral changes in CDCl₃: (A) as-prepared and (B) after exposure to UV light (*trans*:*cis* ≈ 6:94). (c) Fluorescence spectral changes (λ_{ex}= 330 nm) and (d) repeated switching of absorption and fluorescence properties by alternating UV and visible light irradiation.

in the long wavelength region (Fig. 2c). This is in contrast to AzMePy, which exhibited pyrene excimer-like emission at around 440–570 nm even in a dilute solution [36]. Exposure to UV light increased the monomer emission intensities to some extent, and subsequent exposure to blue light restored them close to their original values. Fig. 2d shows that alternating exposure to UV and visible light led to repeated absorption and fluorescence spectral fluctuations without gradual declines. Such excellent photoswitching behaviors can be interpreted as a significant reduction in interference between the azobenzene and pyrene moieties due to the introduction of the longer butoxy linker [39].

To examine molecular assembly and the resulting absorption and emission spectroscopic features, AzBuPy aggregates were prepared by adding water to an AzBuPy DMF solution under gentle shaking conditions. The resulting DMF-H_2O mixture was turbid yellow and maintained stable turbidity at ambient temperature. SEM measurements indicated the formation of long, flat petal-shaped aggregates with lengths and widths of ≥2 μm and <1 μm,

respectively (Fig. 3b). The absorption spectrum had three characteristic absorption bands attributable to the pyrene unit in the 300–355 nm region, which were red-shifted by 6–7 nm, compared to the dilute solution (Fig. 3a and Table 1). Considerably broad absorption bands appearing in the 360–550 nm region are attributed to azobenzene. As the exposure time to UV light increased, the broad bands gradually decreased as a result of *trans*-to-*cis* isomerization. Light irradiation for ~200 seconds was sufficient to reach the *cis*-rich photostationary state. Interestingly, even after UV light exposure for 600 seconds, the turbidity remained constant with little decrease. This can be interpreted as follows. The relatively polar *cis*-azobenzene would be directed toward the polar solvents (outer layer), while nonpolar and flat pyrene units would be stacked through intermolecular π–π stacking interactions and would be located inside the flat microstructures.

Fig. 3c shows emission spectral changes before and after self-assembly. The formation of flat aggregates greatly reduced the monomer emission
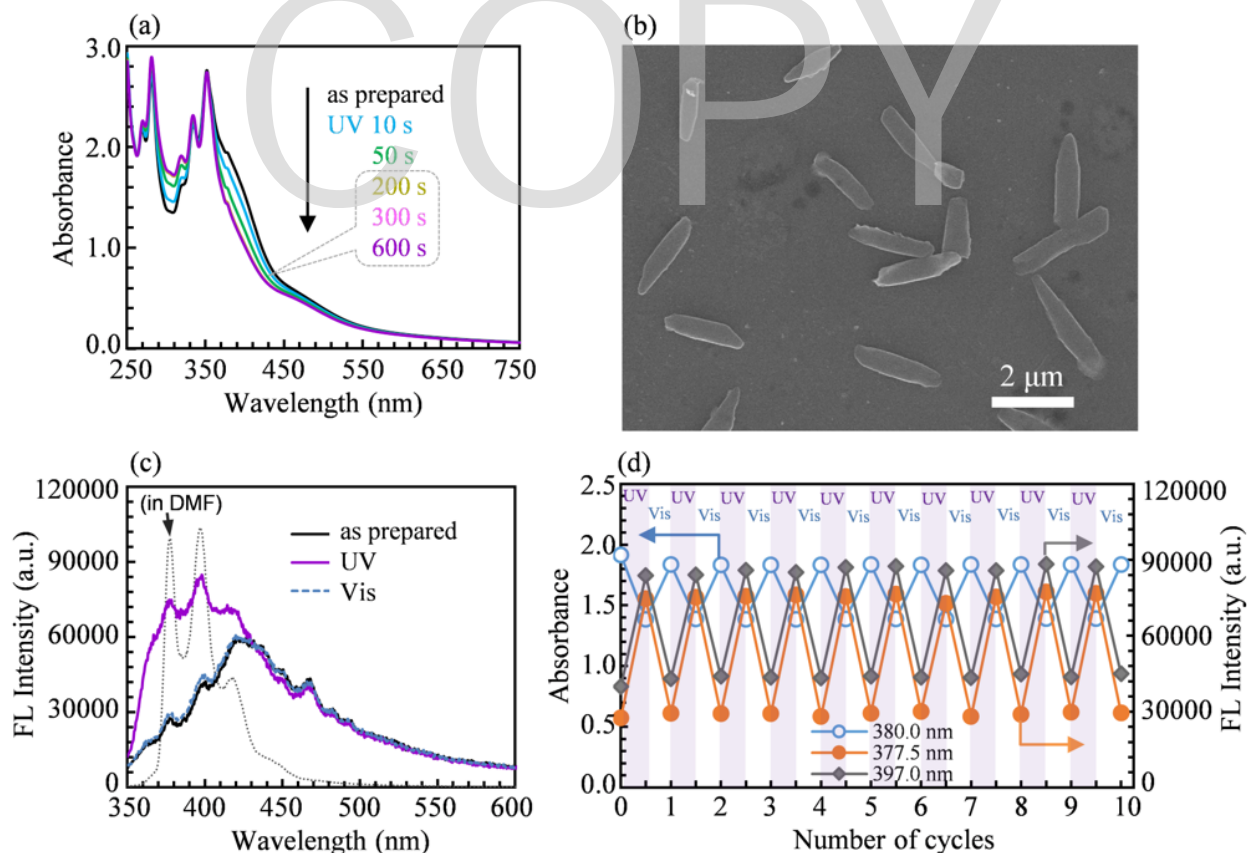
Fig. 3. (a) UV-visible absorption spectral changes of 50 μM DMF-H_2O (1/3, v/v) as a function of UV light irradiation time. (b) SEM image and (c) fluorescence spectra (λ_{ex}= 330 nm) of DMF and 50 μM DMF-H_2O (1/3, v/v) upon UV and subsequent visible light irradiation. (d) Changes in absorption and fluorescence intensity depending on the irradiation of UV light (365 nm, ~2.5 mW/cm^2) and subsequent visible light (436 nm, ~2.5 mW/cm^2).

of the pyrene unit, but weak emission centered at around 425 nm appeared instead. Upon exposure to UV light, weak monomer emission emerged in the 370–450 nm region. Subsequent visible light irradiation restored the shape of the emission spectrum to its initial state. Surprisingly, constant and repeated photoswitching of more than 10 times was possible while maintaining the turbidity of the AzBuPy DMF-H$_2$O mixtures (Fig. 3d).

We next examined the delivery functions of a guest fluorescent dye (9,10-diphenylanthracene: DPA) in the AzBuPy aggregates using the degree of intermolecular interactions between the nonpolar fluorophore and AzBuPy chromophores. AzBuPy and DPA were mixed in equal amounts to form blue fluorescent aggregates using a simple reprecipitation method. Fig. 4 shows UV-visible absorption and fluorescence spectral changes of the turbid DPA@AzBuPy suspension before and after light and thermal treatment at 90 °C. The monomer emission was rarely found in the fluorescence spectrum of the suspension containing the DPA@AzBuPy aggregates. Interestingly, UV light irradiation to induce *trans*-to-*cis* isomerization of the azobenzene moiety significantly reduced the absorption bands corresponding to DPA (at 380.0 and 401.5 nm), together with a decrease in the π-π* absorption band of *trans*-azobenzene. Simultaneously, the blue emission intensity was also reduced.

These absorption and emission spectral results can be interpreted as follows. The relatively polar *cis*-azobenzene would be directed toward the polar solvents and, instead, the nonpolar DPA dyes would exist inside AzBuPy aggregates through favorable intermolecular interaction with the nonpolar pyrene units. Conversely, thermal treatment at 90 °C to induce rapid *cis*-to-*trans* isomerization resulted in recovery of the absorption bands due to the DPA dye, and also increased the blue fluorescence intensity. Therefore, it is considered that when intermolecular interactions between the *trans*-azobenzene units are restored, some of the DPA dye or its aggregates could intervene between the azobenzenes, forming an outer layer of DPA@AzBuPy aggregates.

4. Conclusion

We synthesized a light-responsive pyrene-based azobenzene dye by introducing a butoxy linker between the azobenzene and pyrene moieties, and demonstrated excellent switching behaviors in response to light before and after self-assembly.
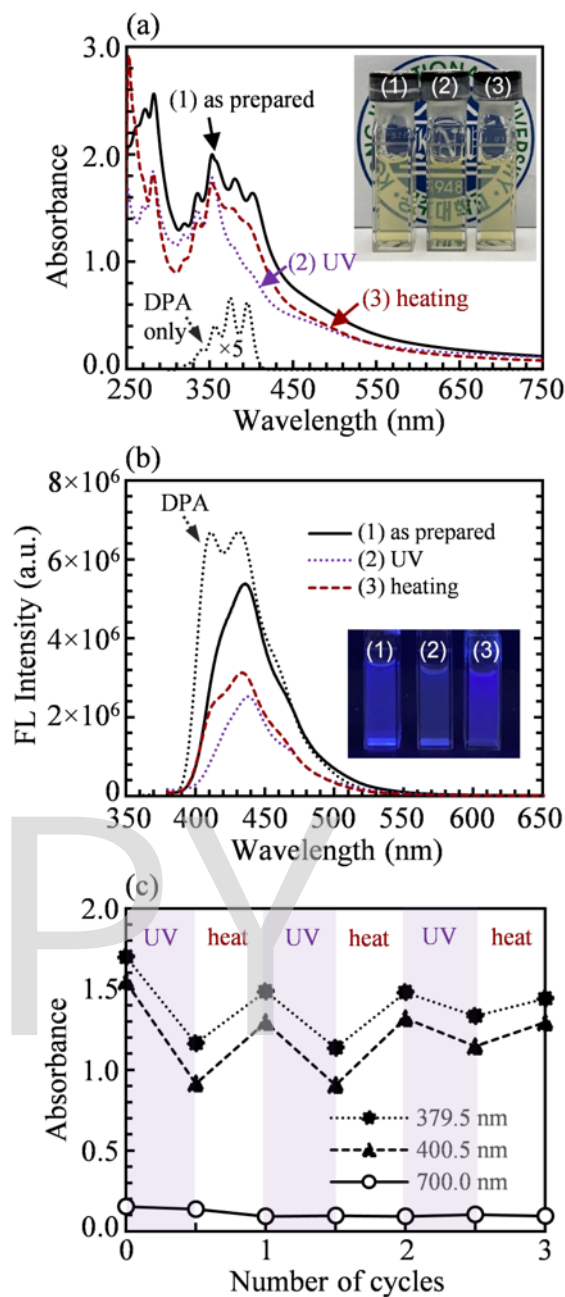
Fig. 4. (a) Absorption and (b) fluorescence spectra of turbid suspension containing AzBuPy and DPA (DPA@AzBuPy suspension). (1) As-prepared 100 μM AzBuPy DMF-H$_2$O (1/2, v/v) containing 100 μM DPA. (2) Spectral changes after UV light irradiation. (3) Spectral recovery after subsequent thermal treatment (90 ˚C). (c) Reversible absorption spectral changes of the DPA@AzBuPy suspension based on the UV light irradiation and subsequent heating at 90 ˚C.

This is in contrast to AzMePy (with a shorter methoxy linker), which did not show light-induced molecular switching in the aggregated states. Exploiting the repeated photoswitching

performance, the delivery functions of conventional hydrophobic fluorophores were investigated. Stimuli-induced *trans↔cis* isomerization of the azobenzene unit caused changes in spectroscopic characteristics of fluorescent dyes.

Acknowledgements

References

1. G. A. Leith, C. R. Martin, A. Mathur, P. Kittikhunnatham, K. C. Park, and N. B. Shustova, *Adv. Energy Mater.,* **12** (2022) 2100441.
2. W. Wu, K. Chen, T. Wang, N. Wang, X. Huang, L. Zhou, Z. Wang, and H. Hao, *J. Mater. Chem. C.,* **11** (2023) 2026.
3. C. Jia, A. Migliore, N. Xin, S. Huang, J. Wang, Q. Yang, S. Wang, H. Chen, D. Wang, B. Feng, Z. Liu, G. Zhang, D. Qu, H. Tian, M. A. Ratner, H. Q. Xu, A. Nitzan, and X. Guo, *Science.,* **352** (2016) 1443.
4. M. Gon, K. Tanaka, and Y. Chujo, *Chem. Asian J.,* **17** (2022) 144.
5. L. Fu, M. Wei, K. Liao, M. Qianli, M. Shao, F. Gu, Y. Fan, L. Longjie, and H. Yanfeng, *J. Pet. Sci. Eng.,* **219** (2022) 111088.
6. A. Singh, A. K. Kar, D. Singh, R. Verma, N. Shraogi, A. Zehra, K. Gautam, S. Anbumani, D. Ghosh, and S. Patnaik, *Chem. Eng. J.,* **427** (2022) 131215.
7. A. Abdollahi, K. Sahandi-Zangabad, and H. Roghani-Mamaqani, *ACS Appl. Mater. Interfaces.,* **10** (2018) 39279.
8. Z. Ni, X. Zheng, B. Bai, H. Wang, J. Wei, and M. Li, *Dyes Pigm.,* **212** (2023) 111135.
9. S. Li, F. Wang, Z. Yang, J. Xu, H. Liu, L. Zhang, and W. Xu, *Powder Technol.,* **359** (2020) 17.
10. D. Moldenhauer, J. P. Fuenzalida Werner, C. A. Strassert, and F. Gröhn, *Biomacromolecules.,* **20** (2019) 979.
11. S. Yang, W. Qin, X. Zhao, F. He, H. Gong, Y. Liu, Y. Feng, Y. Zhou, G. Yu, and J. Li, *Carbohydr. Polym.,* **266** (2021) 118121.
12. Y. Xue, J. Tian, L. Xu, Z. Liu, Y. Shen, and W. Zhang, *Eur. Polym. J.,* **110** (2019) 344.
13. Z. Zeng, D. Qi, L. Yang, J. Liu, Y. Tang, H. Chen, and X. Feng, *J. Controlled Release.,* **315** (2019) 206.
14. X. Wang, M. Shan, S. Zhang, X. Chen, W. Liu, J. Chen, and X. Liu, *Adv. Sci.,* **9** (2022) 2104843.
15. Y. Zhou, J. Song, Y. Hu, J. Cao, Y. Fu, and X. Ma, *Dyes Pigm.,* **215** (2023) 111272.
16. S. M. M., S. Veeranarayanan, T. Maekawa, and S. K. D., *Adv. Drug Deliv. Rev.,* **138** (2019) 18.
17. Z. Shariatinia, *J. Drug Deliv. Sci. Technol.,* **66** (2021) 102790.
18. K. Shikinaka, *Polym. J.,* **48** (2016) 689.
19. E. Cariati, E. Lucenti, C. Botta, U. Giovanella, D. Marinotto, and S. Righetto, *Coord. Chem. Rev.,* **306** (2016) 566.
20. W. Lee, D. Kim, S. Lee, J. Park, S. Oh, G. Kim, J. Lim, and J. Kim, *Nano Today.,* **23** (2018) 97.
21. Z. Wang and X. Huang, *Chem. Eur. J.,* **28** (2022) 609.
22. Z. Gou, A. Wang, M. Tian, and Y. Zuo, *Mater. Chem. Front.,* **6** (2022) 607.
23. O. El-Kadri, T. Tessema, R. M. Almotawa, R. K. Arvapally, M. Al-Sayah, M. A. Omary, and H. El-Kaderi, *ACS Omega.,* **3** (2018) 15510.
24. X. Guo, D. Zhang, T. Wang, and D. Zhu, *Chem. Commun.,* (2003) 914.
25. G. Liu, L. Wang, Y. Zhou, N. Li, H. Zhang, J. Zhu, P. Mao, and X. Xu, *Dyes Pigm.,* **172** (2020) 107800.
26. J. Lv, G. Liu, C. Fan, and S. Pu, *Spectrochim. Acta A Mol. Biomol. Spectrosc.,* **227** (2020) 117581.
27. J. Moreno, F. Schweighöfer, J. Wachtveitl, and S. Hecht, *Chem. Eur. J.,* **22** (2016) 1070.
28. X. Su, Y. Ji, W. Pan, S. Chen, Y. Zhang, T. Lin, L. Liu, M. Li, Y. Liu, and S. X. Zhang, *J. Mater. Chem. C.,* **6** (2018) 6940.
29. S. Ludwanowski, M. Ari, K. Parison, S. Kalthoum, P. Straub, N. Pompe, S. Weber, M. Walter, and A. Walther, *Chem. Eur. J.,* **26** (2020) 13203.
30. Y. Kage, H. Karasaki, S. Mori, H. Furuta, and S. Shimizu, *ChemPlusChem.,* **84** (2019) 1648.
31. He Tian, J. Z., *"Photochromic Materials: Preparation, Properties and Applications",* 2016.
32. P. L. Gentili, M. S. Giubila, R. Germani, and B. M. Heron, *Dyes Pigm.,* **156** (2018) 149.
33. M. Irie, T. Fukaminato, K. Matsuda, and S. Kobatake, *Chem. Rev.,* **114** (2014) 12174.
34. M. Irie, *Chem. Rev.,* **100** (2000) 1683.
35. J. Cusido, E. Deniz, and F. M. Raymo, *Eur. J. Org. Chem.,* **2009** (2009) 2031.
36. P. Thu and M. Han, *Int. J. Mol. Sci.,* **24** (2023) 4504.
37. Y. Okui and M. Han, *Chem. Commun.,* **48** (2012) 11763.
38. M. Han, Y. Okui, and T. Hirade, *J. Mater. Chem. C*, 1 (2013) 3448.
39. L. Q. Zheng, S. Yang, S. Krähenbühl, V. V. Rybkin, J. Lan, I. Aprahamian, and R. Zenobi, *Mater. Today Chem.,* **24** (2022) 100797.

Stabilization of Spontaneous Orientation Polarization by Preventing Charge Injection from Electrodes

Wei-Chih Wang[1,2,3], Kyohei Nakano[1], Yuya Tanaka[4], Hisao Ishii[5,6], Chain-Shu Hsu[2,3], Keisuke Tajima[1*]

[1]*RIKEN Center for Emergent Matter Science (CEMS), 2-1 Hirosawa, Wako, Saitama 351-0198, Japan.*
[2]*Department of Applied Chemistry, National Yang Ming Chiao Tung University, 1001 Daxue Rd., Hsinchu 300093, Taiwan*
[3]*Center for Emergent Functional Matter Science, National Yang Ming Chiao Tung University, 1001 Daxue Rd., Hsinchu 300093, Taiwan*
[4] *Graduate School of Science and Technology, Gunma University, 1-5-1 Tenjin-cho, Kiryu, Gunma 376-0001, Japan*
[5] *Graduate School of Science and Engineering, Chiba University, 1-33, Yayoi-cho, Inage-ku, Chiba 263-8522, Japan*
[6] *Center for Frontier Science, Chiba University, 1-33, Yayoi-cho, Inage-ku, Chiba 263-8522, Japan*
[*]keisuke.tajima@riken.jp

The stability of the surface potential derived from spontaneous orientation polarization (SOP) in 2,2′,2″-(1,3,5-benzinetriyl)-tris(1-phenyl-1-H-benzimidazole) (TPBi) films was significantly improved by inserting an insulating layer at the electrode interface. The time of 20% potential loss from the initial value was extended from 1.3 days to 64 days in the dark at room temperature. Numerical simulations of the electrostatic potential in the films showed that the electrons accumulate at the surface region of the TPBi films in thermodynamic equilibrium, compensating for the internal electric field to decrease the surface potential. It was suggested that the insulating layer prevents electron injection from the electrode and stabilizes the surface potential.
Keywords: Spontaneous orientation polarization, Stability, Dipole moments, Organic semiconductor, Surface potential

1. Introduction

In many organic films prepared by vapor deposition, the formation of a large surface potential has been observed, a phenomenon referred to as spontaneous orientation polarization (SOP).[1-6] It has been hypothesized that the polar molecules have a small directional selectivity (up or down) of the molecular permanent dipole moment during the deposition, which induces the residual polarity in the films perpendicular to the film plane.[7] The surface potentials increase with the thickness of the organic layer to give a surprisingly large potential in the thick films; for example, the as-deposited tris(8-quinolinolato)aluminum (Alq_3) film with a thickness of 560 nm had a surface potential of 28 V.[8] This leads to the possible application of SOP to thin film electrets in the vibronic-based electret generators (EGs)[9] and the charge transport layers in organic light-emitting diodes (OLEDs). To enhance the surface potential change by SOP, various molecular designs have been proposed by considering the molecular dipole moment, molecular conformation, and the orientation control in the films.[3, 5, 10-11]

In addition to the magnitude, the stability of the SOP is also important for the applications. It has been observed that the surface potential of the films decays slowly at room temperature in the dark,
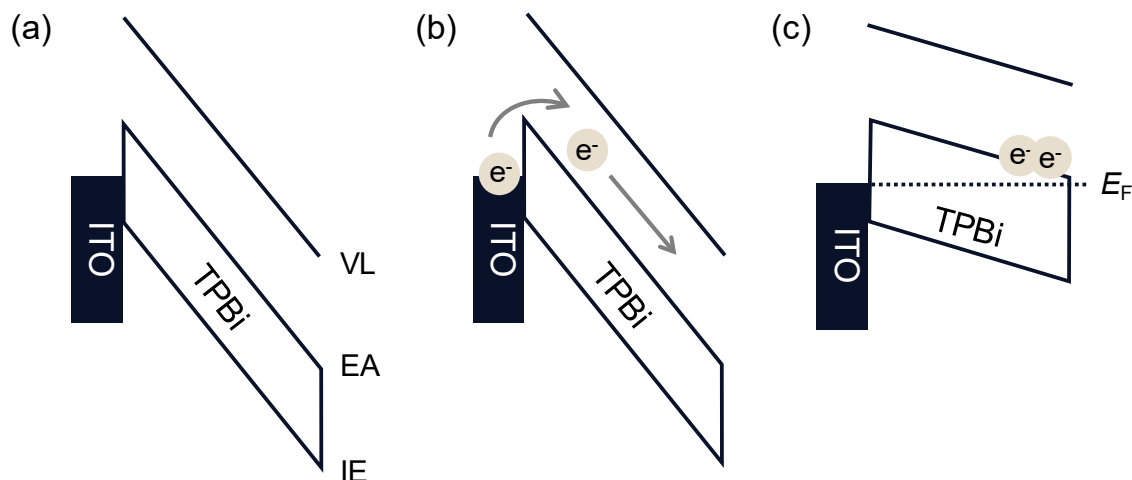
Fig. 1 The schematic illustration of the energy diagram of TPBi/indium tin oxide (ITO) (a) with SOP (in non-equilibrium), (b) with charge injection from ITO, and (c) with charge in TPBi (in equilibrium). VL, EA, IE and E_F represent vacuum level, electron affinity, ionization energy and Fermi level, respectively.

while higher temperature and light irradiation accelerate the decay.[8, 12-17] These decays may be related to electrostatic equilibration; the residual polarity in the organic film results in the large shift of the vacuum level (Fig. 1a), but this state is in principle a non-equilibrium state. At the thermodynamic equilibrium, the Fermi level of the system should align, and the accumulated charges in the organic film can screen the internal electric field to reduce the surface potential (Fig. 1c). The charge carriers can either be thermally injected from the electrodes (Fig. 1b) or generated in the organic layer by photo-induced charge separation assisted by the internal electric field. It has been shown that the potential decay due to the photogeneration of the charges can be avoided by designing the organic molecules with a wide bandgap.[9, 18] It has been reported that an organic overlayer deposited on the film surface can reduce the surface potential and the involvement of the charge injection has been speculated.[19] However, the effects of the charge injection from the electrode interface on the stability of SOP are still unclear.

In this study, the effect of charge injection on the decay of SOP in 2,2′,2″-(1,3,5-benzinetriyl)-tris(1-phenyl-1-*H*-benzimidazole) (TPBi) films was investigated. TPBi is a well-known electron transporting material in OLEDs and has a high SOP in the vacuum deposited films.[20-23] To suppress the charge injection from the electrode, an insulating layer of benzocyclobutene (BCB) was inserted at the interface between ITO and TPBi. Compared to the direct contact between ITO and TPBi, the wide bandgap of the BCB layer creates an injection barrier to slow down the charge injection from the ITO. Numerical simulation was performed to elucidate the charge distribution in the thin film at equilibrium.

2. Experimental

2.1. Sample Preparation

The ITO/glass substrates were ultrasonically cleaned with detergent solution, distilled water, acetone, and isopropanol for 20 min in succession. The substrates were then treated with UV/O$_3$ for 20 min. To form an insulating layer, a benzocyclobutene (BCB, 4.7 wt %, purchased from Dow Chemical) solution, which dissolved in mesitylene, was spin-coated on the cleaned ITO/glass substrates at 3000 rpm for 1 min. The BCB/ITO/glass substrates were heated up by two-step thermal annealing: (1) the substrates were heated up at 150 °C for 10 min to evaporate mesitylene, and (2) the temperature was raised to 250 °C for 3 h. The cross-linked reaction resulted in a three-dimensional network structure of a 22-nm-thick BCB layer. Both the prepared BCB/ITO/glass and ITO/glass substrates were immediately transferred to a vacuum chamber. TPBi (99.8 %, Luminescence Technology) was thermally deposited on both the substrates simultaneously at a stable deposition rate of 0.5 Å/s and the pressure of 2×10^{-4} Pa. After the deposition, the surface potential was measured by Kelvin probe. The whole process was carefully controlled in the dark condition to avoid the possible loss of the surface potential due to the light irradiation.

2.2. Kelvin Probe

The surface potential of the films was measured

using a home-made Kelvin probe system. Details of the system are given below. The sample was placed on the stage, which had a stainless-steel plate with a radius of 4.0 mm about 120 μm above the sample surface. During the measurement, the stainless-steel plate was caused to vibrate at a frequency of 85 Hz a piezoelectric actuator. The AC current in the stainless-steel plate is amplified by a preamplifier (CA5350, NF) and obtained by a lock-in amplifier (LI5640, NF). A DC voltage is applied to the sample and swept to obtain the current-voltage characteristics. The surface potential of the sample is estimated from the applied bias voltage, which gives the minimum AC current with respect to the work function of the stainless-steel plate (−4.32 eV).

2.3. Numerical calculations of Electrostatic Potentials

Numerical calculations of the electrostatic potential were performed based on the model reported by Oehzelt et al. using a custom Python program.[24] The 1D mesh size of the films is 0.5 nm. The initial E_F of TPBi is assumed to be halfway between ionization energy (IE) and electron affinity (EA). The density of TPBi was assumed to be 1.0 g/cm^3 to calculate the site density. The IE and EA values of TPBi are taken from the literature.[25]

3. Results and discussion

3.1. Stability of Spontaneous Orientation Polarization in the Dark

To investigate the effect of an insulating layer on the stability of SOP, the change in the surface potential of 200 nm thick TPBi films on ITO/glass and BCB/ITO/glass substrates was monitored by Kelvin probe for more than 200 days in the atmosphere under dark conditions. The initial values of the surface potentials for TPBi/ITO/glass and TPBi/BCB/ITO/glass are +17.22 V and +17.37 V, respectively, indicating that the orientation of the molecular permanent dipole moments in the TPBi film was not changed by the insertion of the BCB layer. The decay process of the relative surface potential was plotted in Fig. 2. The retention time of 20 % loss in TPBi/BCB/ITO/glass sample was 1542 h (64 days), which is 49 times longer than that in TPBi/ITO/glass (31.2 h, 1.3 days). More than 70 % of the initial surface potential remained in the TPBi/BCB/ITO/glass sample after 216 days. These results confirm that the insertion of the insulating layer slows down the change of the surface potential in the dark. It is speculated that the charge injection from the electrode to the SOP layer was suppressed by the insertion of the BCB layer.
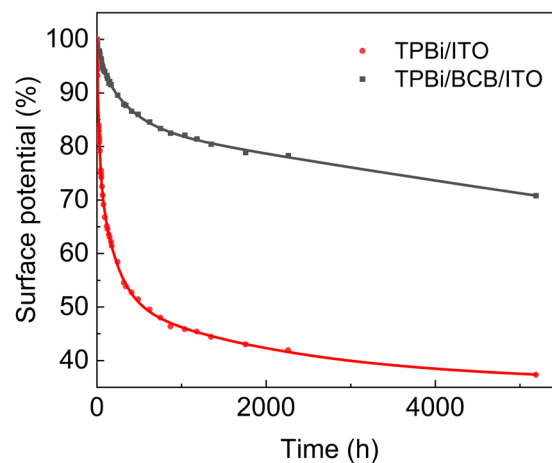
Fig. 2 Decay curves of the surface potential in TPBi/ITO/glass and TPBi/BCB/ITO/glass samples under the dark conditions. The lines are a guide for the eyes.

3.2. Numerical Simulation

The time-dependent SOP values in Fig. 2 suggest that just after the deposition of TPBi on an ITO electrode, the system is not in the thermodynamic equilibrium. Since the SOP decay rate changed with the insertion of an insulating layer between the electrode and TPBi, this time dependence may involve the number of the injected charges, implying the SOP decay corresponds to the system reaching the thermodynamic equilibrium. To discuss the effect of the injected charges on the SOP value, we calculated the electrostatic potential in the SOP layer under thermodynamic equilibrium conditions as an ultimate limit following the reported method.[24] This calculation solves the Poisson equation self-consistently with the given molecular orbital energy levels and the distributions, in which the Fermi level of the organic semiconductor aligns with the work function of the electrode. The charge carrier density in the semiconductor is calculated using the Gaussian shaped density of states (DOS) of the highest occupied molecular orbital (HOMO) and the lowest unoccupied molecular orbital (LUMO) and the Fermi-Dirac distribution. The input parameters are given in Table 1. To simulate SOP effect in the films, we included additional surface charges of ±2.2 mC/m^2 at the bottom and top surface of the TPBi layer, which corresponds to the SOP of +82.9 mV/nm.

Fig. 3a shows the electrostatic potentials in the TPBi layer at different thicknesses. The potentials in the films and at the surface are represented by the lines and the filled squares, respectively. In the thin film regime (< 30 nm), the surface potential increased monotonically with thickness, which agrees with the experimental results from the Kelvin
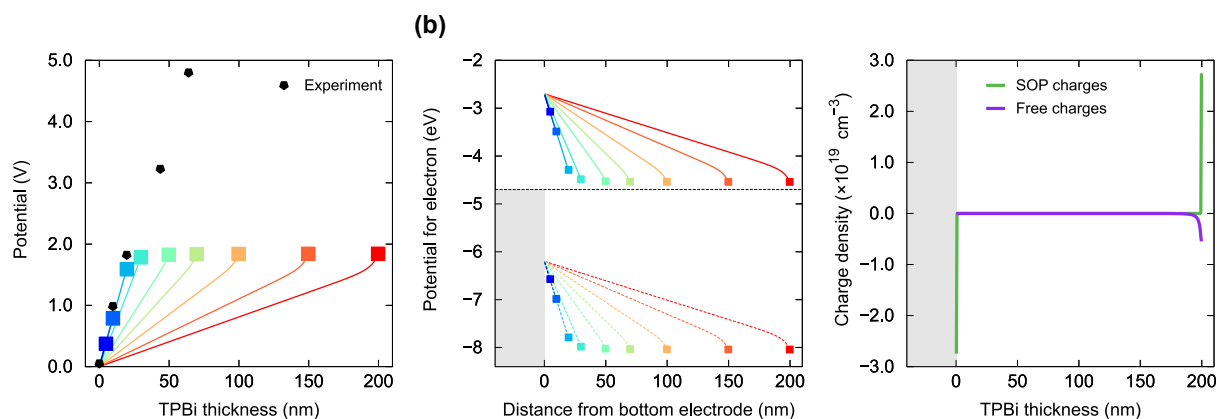
Fig. 3 (a) Electrostatic potential simulation results of the thickness dependence of the surface potentials for TPBi on ITO/glass substrate. (b) Energy diagram with different thicknesses of TPBi layer. (c) Charge density distribution in the 200 nm thick TPBi film on ITO. The negative and positive charge densities correspond to the electrons and hole densities, respectively.

Table 1. Parameters used for the electrostatic potential calculations. HOMO σ and LUMO σ represent the σ values for the gaussian shaped HOMO and LUMO bands, respectively.

Layer	E_F (eV)	Permittivity	Site density (cm^{-3})	IE (eV)	HOMO σ (meV)	EA (eV)	LUMO σ (meV)
ITO	−4.7	-	-	-	-	-	-
TPBi	−4.45	3.0	9.1×10^{20}	6.2	250	2.7	250

probe, plotted with the black pentagons. However, for the thicknesses above 30 nm, the calculated surface potentials saturated at about +1.8 V and remained unchanged up to 200 nm. This saturation of the potential can be understood from the calculated energy diagram shown in Fig. 3b. For thick TPBi layers, the HOMO (dashed lines) and LUMO (solid lines) are bent by the potential through SOP, moving the LUMO at the film surface close to E_F. Under equilibrium condition, this means that electrons accumulate at the film surface, and the density of states of the LUMO to accommodate the electrons at the surface determines the saturated energy diagram. Note that this saturated energy level behavior is sometimes referred to as Fermi level pinning, where gap states trap E_F and leave it unchanged. However, there were no additional gap states in our simulation, and we only used a Gaussian-shaped DOS, indicating that the pinning behavior is not due to gap states, but is due to the requrement of thermodynamic equilibrium. The charge carrier distribution in the TPBi layer is shown in Fig. 3c. Besides the fixed surface charges corresponding to the SOP (green lines), there are negative charges near the surface due to the injected free charges (purple line). This compensates for the surface potential due to the SOP.

When the system is in the thermodynamic equilibrium, the remaining SOP potential is about +1.8 V; however, we observed the initial potential as high as +17 V. This indicates that the system does not reach the thermal equilibrium in the beginning and the electron injection from ITO into TPBi is a slow process, which determines the slow decay of the surface potential in the dark. The insertion of the insulating layer between the electrode and TPBi made the process more inactive, resulting in the improved long-term stability of the SOP.

4. Conclusion

We have shown that the stability of SOP is greatly improved by inserting the insulating layer between the electrode and the organic layer. For the application of the organic films with SOP to vibronic-based EG, where the top electrode is absent and the films can be in non-equilibrium state, this is a simple but promising strategy to improve the device stability. In contrast, when applied to OLED, where the top metal electrode is present and the charge injection is necessary to operate the device, the organic films are in equilibrium and the surface potentials are screened by the accumulated charges. In this case, the numerical calculations can be useful to study the energy structure inside the films.

Acknowledgement

References

1. Noguchi, Y.; Brütting, W.; Ishii, H., Spontaneous orientation polarization in organic light-emitting diodes. *Jpn. J. Appl. Phys.* **2019,** *58* (SF), SF0801.

2. Noguchi, Y.; Tanaka, Y.; Ishii, H.; Brütting, W., Understanding spontaneous orientation polarization of amorphous organic semiconducting films and its application to devices. *Synth. Met.* **2022,** *288*, 117101.

3. Noguchi, Y.; Lim, H.; Isoshima, T.; Ito, E.; Hara, M.; Won Chin, W.; Wook Han, J.; Kinjo, H.; Ozawa, Y.; Nakayama, Y.; Ishii, H., Influence of the direction of spontaneous orientation polarization on the charge injection properties of organic light-emitting diodes. *Appl. Phys. Lett.* **2013,** *102* (20), 203306.

4. Noguchi, Y.; Miyazaki, Y.; Tanaka, Y.; Sato, N.; Nakayama, Y.; Schmidt, T. D.; Brütting, W.; Ishii, H., Charge accumulation at organic semiconductor interfaces due to a permanent dipole moment and its orientational order in bilayer devices. *J. Appl. Phys.* **2012,** *111* (11), 114508.

5. Tanaka, M.; Auffray, M.; Nakanotani, H.; Adachi, C., Spontaneous formation of metastable orientation with well-organized permanent dipole moment in organic glassy films. *Nature Mater.* **2022,** *21* (7), 819-825.

6. Osada, K.; Goushi, K.; Kaji, H.; Adachi, C.; Ishii, H.; Noguchi, Y., Observation of spontaneous orientation polarization in evaporated films of organic light-emitting diode materials. *Org. Electron.* **2018,** *58*, 313-317.

7. Friederich, P.; Rodin, V.; von Wrochem, F.; Wenzel, W., Built-In Potentials Induced by Molecular Order in Amorphous Organic Thin Films. *ACS Appl. Mater. Interfaces* **2018,** *10* (2), 1881-1887.

8. Ito, E.; Washizu, Y.; Hayashi, N.; Ishii, H.; Matsuie, N.; Tsuboi, K.; Ouchi, Y.; Harima, Y.; Yamashita, K.; Seki, K., Spontaneous buildup of giant surface potential by vacuum deposition of Alq$_3$ and its removal by visible light irradiation. *J. Appl. Phys.* **2002,** *92* (12), 7306-7310.

9. Tanaka, Y.; Matsuura, N.; Ishii, H., Self-Assembled Electret for Vibration-Based Power Generator. *Sci. Rep.* **2020,** *10* (1), 6648.

10. Wang, W.-C.; Nakano, K.; Hashizume, D.; Hsu, C.-S.; Tajima, K., Tuning Molecular Conformations to Enhance Spontaneous Orientation Polarization in Organic Thin Films. *ACS Appl. Mater. Interfaces* **2022,** *14* (16), 18773-18781.

11. Schmid, M.; Harms, K.; Degitz, C.; Morgenstern, T.; Hofmann, A.; Friederich, P.; Johannes, H.-H.; Wenzel, W.; Kowalsky, W.; Brütting, W., Optical and Electrical Measurements Reveal the Orientation Mechanism of Homoleptic Iridium-Carbene Complexes. *ACS Appl. Mater. Interfaces* **2020,** *12* (46), 51709-51718.

12. Sugi, K.; Ishii, H.; Kimura, Y.; Niwano, M.; Ito, E.; Washizu, Y.; Hayashi, N.; Ouchi, Y.; Seki, K., Characterization of light-erasable giant surface potential built up in evaporated Alq$_3$ thin films. *Thin Solid Films* **2004,** *464-465*, 412-415.

13. Ozasa, K.; Nemoto, S.; Isoshima, T.; Ito, E.; Maeda, M.; Hara, M., Photoinduced reduction and pattern preservation of giant surface potential on tris(8-hydroxyquinolinato) aluminum(III) thin films. *Appl. Phys. Lett.* **2008,** *93* (26), 263304.

14. Ozasa, K.; Ito, H.; Maeda, M.; Hara, M., Photoinduced evolution of surface-potential undulation observed on vacuum-deposited thin films of tris(8-hydroxyquinolinato) aluminum. *Appl. Phys. Lett.* **2011,** *98* (1), 013301.

15. Ozasa, K.; Nemoto, S.; Maeda, M.; Hara, M., Kelvin probe force microscope with near-field photoexcitation. *J. Appl. Phys.* **2010,** *107* (10), 103501.

16. Yoshizaki, K.; Manaka, T.; Iwamoto, M., Large surface potential of Alq$_3$ film and its decay. *J. Appl. Phys.* **2004,** *97* (2), 023703.

17. Kajimoto, N.; Manaka, T.; Iwamoto, M., Decay process of a large surface potential of Alq$_3$ films by heating. *J. Appl. Phys.* **2006,** *100* (5), 053707.

18. Wang, W.-C.; Nakano, K.; Tanaka, Y.; Kurihara, K.; Ishii, H.; Hashizume, D.; Hsu, C.-S.; Tajima, K., Improved Photostability of Spontaneous Orientation Polarization with 1,3,5,7-tetrakis(1-phenyl-1H-benzo[d]imidazol-2-yl)adamantane in Thin Films. *Submitted*.

19. Ito, E.; Isoshima, T.; Ozasa, K.; Hara, M., Influence of Organic Overlayer on Giant

Surface Potential of Alq$_3$ Film. *Molecular Crystals and Liquid Crystals* **2006,** *462* (1), 111-116.

20. Tao, Y.; Yang, C.; Qin, J., Organic host materials for phosphorescent organic light-emitting diodes. *Chem. Soc. Rev.* **2011,** *40* (5), 2943-2970.

21. Kajjam, A. B.; Dubey, D. K.; Kumar Yadav, R. A.; Jou, J. H.; Sivakumar, V., Tetraphenylimidazole-based luminophores for explosive chemosensors and OLEDs: experimental and theoretical investigation. *Materials Today Chemistry* **2019,** *14*, 100201.

22. Park, M.-H.; Park, J.; Lee, J.; So, H. S.; Kim, H.; Jeong, S.-H.; Han, T.-H.; Wolf, C.; Lee, H.; Yoo, S.; Lee, T.-W., Efficient Perovskite Light-Emitting Diodes Using Polycrystalline Core–Shell-Mimicked Nanograins. *Adv. Funct. Mater.* **2019,** *29* (22), 1902017.

23. Kim, J. Y.; Kim, W. Y.; Cheah, K. W., Quantitative Analysis of Charge Distribution in Bi-Emissive layer White Organic Light-Emitting Diodes with Two Fluorescent Dopants. *Sci. Rep.* **2018,** *8* (1), 3172.

24. Oehzelt, M.; Koch, N.; Heimel, G., Organic semiconductor density of states controls the energy level alignment at electrode interfaces. *Nature Communications* **2014,** *5* (1), 4174.

25. Anthopoulos, T. D.; Markham, J. P. J.; Namdas, E. B.; Samuel, I. D. W.; Lo, S.-C.; Burn, P. L., Highly efficient single-layer dendrimer light-emitting diodes with balanced charge transport. *Appl. Phys. Lett.* **2003,** *82* (26), 4824-4826.

Magnetic-Pneumatic Hybrid Soft Actuator

Kosei Ito and Fujio Tsumori*

*Department of Aeronautics and Astronautics, Kyushu University,
744 Motooka, Nishi-ku, Fukuoka 819-0395, Japan
tsumori @aero.kyushu-u.ac.jp

In this study, we developed a new actuator that can be driven by both magnetic and pneumatic and conducted driving experiments using the fabricated actuator. Soft actuators are widely used as a means of biomimicry. However, many existing actuators that use a single drive source have limited degrees of freedom and deformation capabilities. Recently, hybrid actuators that can be driven by multiple sources have gained attention due to their ability to produce movements that are not achievable by a single drive source. In this study, we fabricated a simple actuator that combines a cylindrical pillar made of silicone material containing magnetic particles with a hollow structure for pneumatic deformation. Three types of actuators with varying diameters and positions of the hollow structure were fabricated, and the drive of each actuator was measured. The pneumatic extensible actuator allows the actuator tip to be manipulated on a fan-shaped two-dimensional plane. The pneumatic bending actuator could manipulate the actuator tip in three dimensions. The actuator with a larger diameter hollow structure could be deformed differently in the same magnetic field by changing the stiffness of the actuator depending on the air pressure. Furthermore, by modifying the hollow structure and the external shape of the actuator, more unique movements can be achieved, and it is expected to be applied to bio-mimicry such as tentacle movement and cilia structure.

Keywords: Soft actuator, Magnetic, Pneumatic, Hybrid actuator, Manipulation, Bio-mimicry

1. Introduction

Soft actuators are made of flexible and lightweight materials, such as silicone rubber, and can be driven by various methods, including pneumatic or hydraulic fluid pressure [1–4], and smart materials that respond to external stimuli like electricity [5,6], magnetic fields [7–28], temperature [29–31], or light [32]. These drive methods enable softer and more delicate movements than conventional rigid actuators that use metal parts, and they are frequently used in biomimicry to replicate human body functions, such as the heart [33] and tongue [34], or natural movements like those of a caterpillar [11,35] or the tentacles of an octopus [36].

Recently, researchers have been developing hybrid-drive soft actuators that combine multiple drive sources, allowing for greater manipulation freedom and larger deformations that are impossible with a single drive source [37,38]. However, the combination of drive sources complicates deformation control and requires a more expensive setup for the drive, limiting their practical applications. To address this issue, we fabricated a simple actuator that can be driven by both a magnetic field and pneumatic pressure by adding a hollow structure for pneumatic deformation to a cylindrical pillar made of silicone material containing magnetic particles.

The driving principles of magnetic field and pneumatic pressure are explained as follows. To drive an actuator using a magnetic field, the actuator containing magnetic particles is magnetized, which is a process of applying a strong magnetic field to the particles to leave residual magnetization. When an external magnetic field is applied to a magnetized actuator, the magnetic moment acts in the direction of the external magnetic field and the direction of the remanent magnetization, causing the actuator to deform (Fig. 1). Pneumatic actuation deforms the

actuator by increasing the internal pressure like a balloon. In the cylindrical balloon fabricated in this study, pneumatic deformation causes elongation when the film thickness is uniform and bending when the film thickness is anisotropic (Fig. 2). A drive was also developed to change the stiffness of the actuator by depressurizing it and concaving its cross-section.

In this study, we fabricated three types of actuators: one that undergoes elongation deformation when the hollow structure is pressurized, one that undergoes bending deformation when pressurized, and one whose stiffness is changed by depressurization. Driving experiments were conducted using these actuators in combination with magnetic field driving, and the resulting deformation was measured to investigate the driving characteristics.
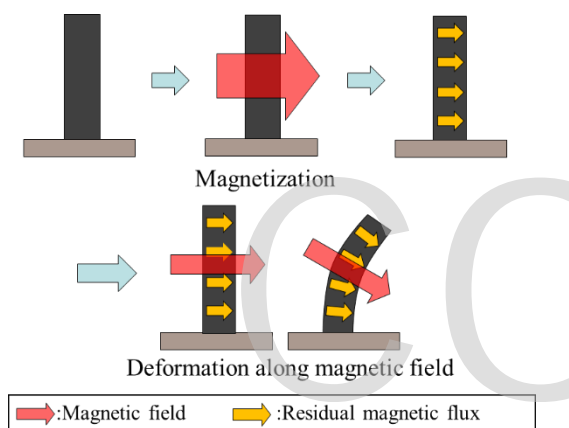
Fig. 1.   Schematic illustration of a magnetically driven soft actuator.
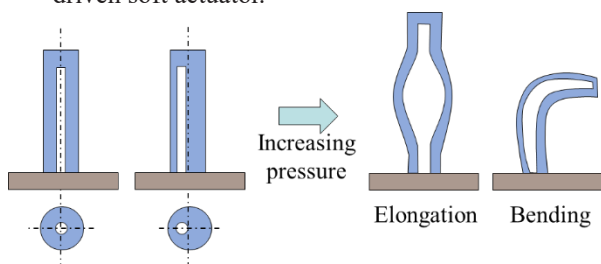
Fig. 2.   Schematic illustration of a pneumatic driven soft actuator with a central and eccentric hollow cavity.

2. Materials and driving system

2.1. Materials

This section provides information about the materials and methods used to fabricate the magnetic field/pneumatic hybrid actuator. The Ecoflex 00-30 (Smooth-On) was chosen as the two-component silicone resin material due to its high flexibility and durability. SF-500 (DOWA F-Tec), with an average particle diameter of 1.42 μm, was selected as the magnetic particle for the actuator.

Strontium ferrite was used to make the particles, which is a hard-magnetic material commonly used as a permanent magnet material.

To make the actuator, a mold was created by combining three parts: a plastic tube with an inner diameter of 4.0 mm and a length of 20 mm, a metal pin with a diameter of 0.80 mm and a length of 22 mm, and a part to fix the metal pin. The fixed parts were made of PLA (Poly-Lactic Acid) resin using a 3D printer (Original Prusa i3 Mk3, Prusa Research). For the actuator used in section 3.3, which deforms the cross-section by depressurizing, a thick metal pin with a diameter of 2 mm was used.

2.2. Fabrication

The fabrication process for the actuator is presented in Fig. 3. Firstly, magnetic particles (20 mass%) were added to silicone rubber. The mixture was then stirred and deaerated using a stirring and deaeration device (Kakuhunter, Shasin Kagaku CO., LTD.) to achieve a uniform dispersion of the magnetic particles, resulting in the production of magnetic elastomer. The magnetic particle-dispersed elastomer was then injected into a mold using a syringe, and a fixing component was inserted to secure the position of a metal pin at the top. The sample was then placed in a vacuum chamber for 1.2 ks (20 min) to remove air bubbles. The silicone was cured at 50 °C for 3.6 ks (1 h). The fixing component at the top was then removed, and the cured sample was slid up slightly while still attached to the metal pin. Additional magnetic particle-dispersed elastomer was injected from the top, and the top hole was closed by placing the sample in a vacuum chamber for 600 s (10 min) to fill it with silicone. The silicone was then cured at 50 °C for 1.8 ks (30 min). Finally, the sample was removed from the mold and connected to an air supply connector (Mini Tube Connector, ARAM Corporation) for inflation. The gaps at the connection were filled with instant adhesive (CA-522, CEMEDINE CO., LTD.).

2.3. Driving System

A system was constructed to enable the application of both magnetic field and pneumatic pressure concurrently. To generate a uniform parallel magnetic field of 50 mT at the center of the system, permanent magnets were placed diagonally as illustrated in Fig. 4. Air pressure was regulated by a syringe that was connected to the actuator from underneath the stage.
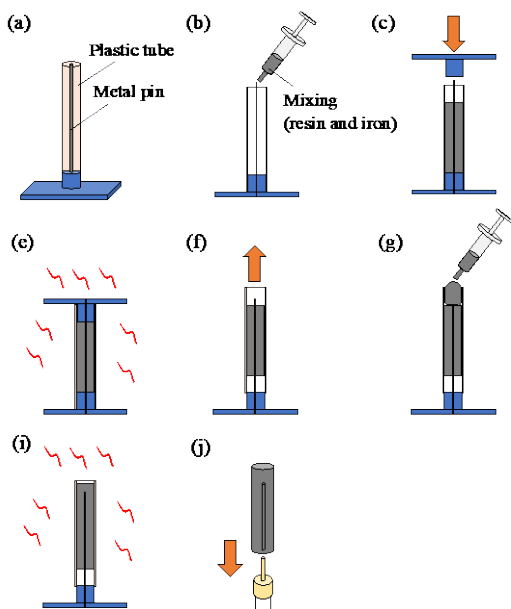
Fig. 3. Fabrication process for actuators that can be driven by both magnetic and pneumatic fields.
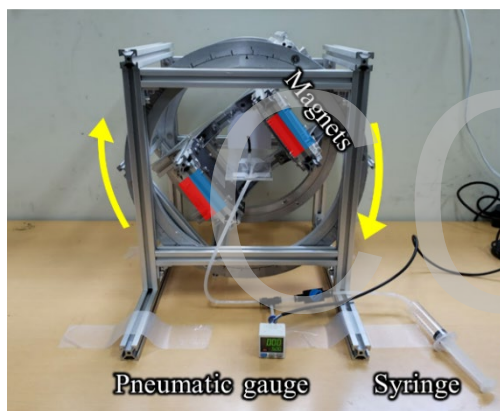
Fig. 4. Systems for magnetic and pneumatic drive.

3. Experimental

3.1. Pneumatic extension actuator

Snapshots (a) and measured displacements of a pneumatic extension actuator (b) are shown in Fig. 5. The internal pressure was fixed at 0, 10, 25, and 30 kPa, the angle of the parallel magnetic field was rotated between 0 and 360 degrees, and displacements were measured every 30 degrees.

The magnetic field drive only allows movement on a circular arc, while the pneumatic drive only allows deformation by extending and retracting in the longitudinal direction. By combining magnetic and pneumatic drive, we were able to extend the operation range to a two-dimensional plane.

The actuator is tilted to the left (negative side of the x-axis) as a whole, which is because the actuator could not be fixed in a strictly symmetrical manner or due to a fabrication error. In addition, when 30

kPa was applied, the actuator was greatly extended, which may have caused it to fall outside the range of the uniform parallel magnetic field of the device. To accurately apply a uniform parallel magnetic field even after stretching under pressure, the actuator must be made smaller.
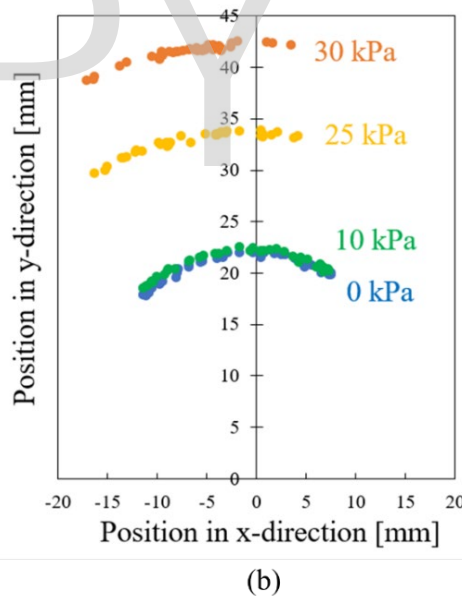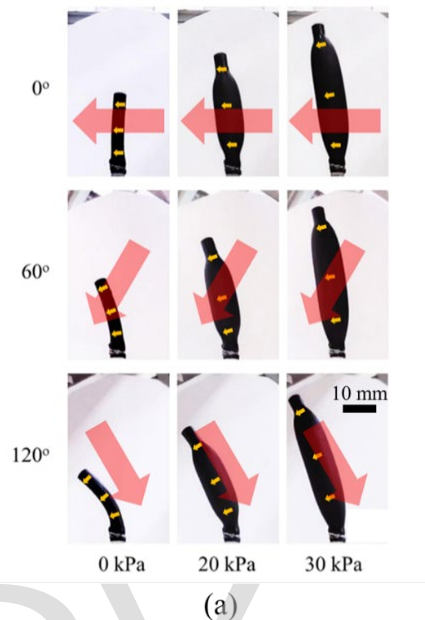
Fig. 5. Snapshots and measured displacements of a pneumatic extension actuator.

3.2. Pneumatic bending actuator

We fabricated an actuator that bends when pressurized by displacing the center of the hollow structure by 0.5 mm from the axis. When this actuator is pressurized, it deforms as shown in Fig. 6(a). The top line in Fig.6(a) shows the side view, and the following lines show the front view. This actuator begins to expand at 15 kPa and

subsequently expands by the amount of air injected without any change in air pressure. Thus, we divided the expanding phase into three stages labeled as (1), (2), and (3) at 15 kPa. Magnetization was applied perpendicular to the direction in which pneumatic pressure causes bend deformation. The actuator was set to bend in the z-axis direction, fixed at 0 kPa and three stages of expansion at 15 kPa, and driven by the application of a magnetic field.

Figure 6(b) show snapshots taken from the front and a plot of the actuator tip, respectively. The actuator was bent in the forward direction by the pneumatic drive, and then the tip was deformed in a circular motion by the magnetic drive. The pneumatic bending actuator, in combination with

the magnetic field, was able to manipulate the actuator tip in three dimensions.

3.3. Stiffness change actuator

We developed an actuator with a larger hollow diameter compared to the ones used in sections 3.1 and 3.2, which utilizes deformation of the cross section induced by depressurization. The internal pressure was set at -20, 0, and 8 kPa, and the angle of the parallel magnetic field was rotated between 0 and 360 degrees, with the displacement being measured every 10 degrees. During depressurization, the actuator was externally pressed on the side to assist the cross-section in bending concavely in the desired direction.

Figure 7 displays a snapshot of the actuator and the measured tip displacement. By collapsing the hollow portion of the actuator under reduced

Fig. 6. Snapshots and measured displacements of a pneumatic bending actuator. The top line of (a) shows the side view, and the following lines show the front view.
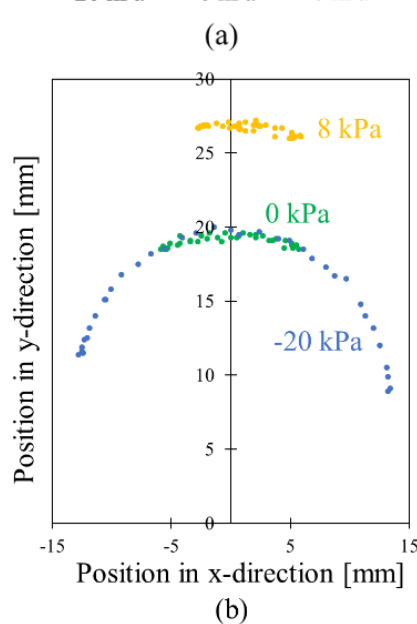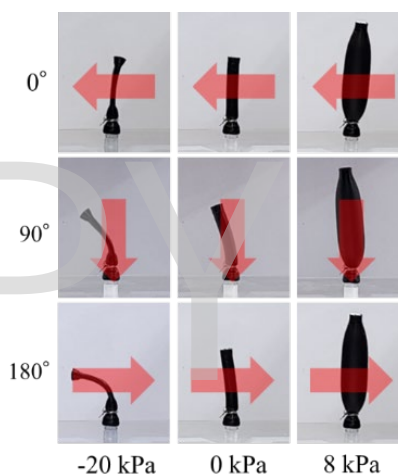
Fig. 7. Snapshots and measured displacements of an actuator using stiffness change actuator.

pressure, the moment of inertia of area was reduced, increasing the deformation caused by the magnetic field. The actuator could also be elongated when pressurized.

4. Conclusion

We have developed an actuator that is capable of being powered by both air pressure and a magnetic field. By altering the diameter and location of the hollow structure, we have produced three distinct types of actuators. The pneumatic extensional actuator can be manipulated in a fan-shaped two-dimensional plane, while the pneumatic bending actuator can be driven in a circular motion in addition to the forward bending. The actuator with a larger hollow structure was able to achieve unique deformations by adjusting the stiffness through negative pressure. Our actuator design has the potential to be further developed for biomimetic applications, such as mimicking the movements of biological tentacles and cilia structures.

References

1. R. F. Shepherd, F. Ilievski, W. Choi, S. A. Morin, A. A. Stokes, A. D. Mazzeo, X. Chen, M. Wang, and G. M. Whitesides, *Proc. Natl. Acad. Sci. U S A,* **108** (2011) 20400.
2. P. Ohta, L. Valle, J. King, K. Low, J. Yi, C. G. Atkeson, and Y. L. Park, *Soft Robotics*, **5** (2018) 204.
3. Y. S. Narang, J. J. Vlassak, and R. D. Howe, *Adv. Funct. Mater.*, **28** (2018) 1707136.
4. K. Becker, C. Teeple, N. Charles, Y. Jung, D. Baum, J. C. Weaver, L. Mahadevan, and R. Wood, *Proc. Natl. Acad. Sci. U S A*, **119** (2022) e2209819119.
5. R. Kornbluh, R. Pelrine, J. Eckerle, and J. Joseph, *Proc. IEEE ICRA*, **3** (1998) 2147.
6. J. Bernat and J. Kołota, *Energies*, **14** (2021) 5633.
7. H. Shinoda and F. Tsumori, *Proc. IEEE-MEMS*, (2020) 497.
8. F. Tsumori and J. Brunne, *Proc. IEEE-MEMS*, (2011) 1245.
9. T. Murakami and F. Tsumori, *Jpn. J. Appl. Phys.*, **61** (2022) SD1014.
10. H. Shinoda and F. Tsumori, *Jpn. J. Appl. Phys.*, **57** (2018) 06HJ05.
11. K. Maeda, H. Shinoda, and F. Tsumori, *Jpn. J. Appl. Phys.*, **59** (2020) SIIL04.
12. H. Shinoda, S. Azukizawa, K. Maeda, and F. Tsumori, *J. Electrochem. Soc.*, **166** (2019) B3235.
13. S. Azukizawa, H. Shinoda, K. Tokumaru, and F. Tsumori, *J. Photopolym. Sci. Technol.*, **31** (2018) 139.
14. F. Tsumori, A. Saijou, T. Osada, and H. Miura, *Jpn. J. Appl. Phys.*, **54** (2015) 06FP12.
15. M. Furusawa, K. Maeda, S. Azukizawa, H. Shinoda, and F. Tsumori, *J. Photopolym. Sci. Technol.*, **32** (2019) 309.
16. R. Marume, F. Tsumori, K. Kudo, T. Osada, and K. Shinagawa, *Jpn. J. Appl. Phys.,* **56** (2017) 06GN15.
17. S. Azukizawa, F. Tsumori, H. Shinoda, K. Tokumaru, K. Kudo, and K. Shinagawa, *Proc. MicroTAS*, (2020) 623.
18. F. Tsumori, R. Marume, A. Saijou, K. Kudo, T. Osada, and H. Miura, *Jpn. J. Appl. Phys.*, **55** (2016) 06GP19.
19. F. Tsumori and K. Tokumaru, *Proc. MicroTAS*, (2020) 396.
20. S. Shigetomi and F. Tsumori, *J. Photopolym. Sci. Technol.*, **34** (2021) 375.
21. S. Gaysornkaew and F. Tsumori, *Jpn. J. Appl. Phys.*, **60** (2021) SCCL02.
22. H. Shinoda, S. Azukizawa, and F. Tsumori, in *22nd International Conference on Miniaturized Systems for Chemistry and Life Sciences, MicroTAS 2018*, (2018) 679.
23. S. Shigetomi, H. Takahashi, and F. Tsumori, *J. Photopolym. Sci. Technol.*, **33** (2020) 193.
24. K. Ninomiya, S. Gaysornkaew, and F. Tsumori, *Proc. IEEE-MEMS*, (2022) 235.
25. S. Gaysornkaew, D. V. Vargas, and F. Tsumori, *IEEE CYBCONF*, (2021) 061.
26. H. Shinoda, S. Azukizawa, K. Maeda, and F. Tsumori, *ECS Trans.*, **88** (2018) 89.
27. F. Tsumori, H. Kawanishi, K. Kudo, T. Osada, and H. Miura, *Jpn. J. Appl. Phys.*, **55** (2016) 06GP18.
28. F. Tsumori, N. Miyano, A. Fukui, K. Sagawa, and H. Kotera, *Proc. COMPLAS*, (2007) 354.
29. K. Takashima, J. Rossiter, and T. Mukai, Sens. actuators. A Phys., **164** (2010) 116.
30. A. Miriyev, K. Stack, and H. Lipson, *Nat. Commun.*, **8** (2017) 596.
31. T. Noguchi and F. Tsumori, *Jpn. J. Appl. Phys.*, **59** (2020) SIIL08.
32. M. Pilz da Cunha, S. Ambergen, M. G. Debije, E. F. G. A. Homburg, J. M. J. den Toonder, and A. P. H. J. Schenning, *Adv. Sci.*, **7** (2020) 1902842.

33. E. T. Roche, M. A. Horvath, I. Wamala, A. Alazmani, S. E. Song, W. Whyte, Z. Machaidze, C. J. Payne, J. C. Weaver, G. Fishbein, J. Kuebler, N. v. Vasilyev, D. J. Mooney, F. A. Pigula, and C. J. Walsh, *Sci. Transl. Med.*, **9** (2017) eaaf3925.

34. N. Endo, Y. Kizaki, and N. Kamamichi, *J. Robot. Mechatron*., **32** (2020) 894.

35. P. Karipoth, A. Christou, A. Pullanchiyodan, and R. Dahiya, *Adv. Intell. Syst*., **4** (2022) 2100092.

36. B. Mazzolai, A. Mondini, F. Tramacere, G. Riccomi, A. Sadeghi, G. Giordano, E. del Dottore, M. Scaccia, M. Zampato, and S. Carminati, *Adv. Intell. Syst*., **1** (2019) 1900041.

37. J. E. Lee, Y. Sun, Y.-C. Sun, I. R. Manchester, and H. E. Naguib, *Appl. Mater. Today*, **29** (2022) 101681.

38. B. Han, Z. C. Ma, Y. L. Zhang, L. Zhu, H. Fan, B. Bai, Q. D. Chen, G. Z. Yang, and H. B. Sun, *Adv. Funct. Mater.*, **32** (2022) 2110997 .

Developing a Laparoscope Lens with Super Water-Repellent Antifouling Function using Biomimetic Materials

Atsushi Sekiguchi[1,2]*, Hiroko Minami[2], Masaaki Yasuda[1], and Yoshihiko Hirai[1]

[1] Osaka Metropolitan University, Department of Physics and Electronics
1-1 Gakuen-cho, Naka-ku, Sakai, Osaka 599-8531, Japan
[2] Litho Tech Japan corporation
2-6-6 Namiki, Kawaguchi, Saitama 332-0034, Japan
*n21175e@omu.ac.jp

Laparoscopes are now widely used in clinical settings. Laparoscopes are particularly useful in detecting cancers and excising affected areas. During laparoscopic operations, however, the spatter of blood and bodily fluids resulting from the excision of the affected area can fog the objective lens. Condensation on the lens caused by temperature differences between the instrument interior and exterior can also obscure vision. Any obstruction of the field of view during the surgical procedure must be addressed by cleaning the lens at the tip; however, doing so prolongs the time required for the procedure, makes it more invasive, and increases patient burdens. Drawing on biomimicry principles, we developed a laparoscope lens with super water-repellent and antifouling properties. This paper reports our results.

Keywords: Laparoscope, Minimally Invasive, Biomimetics, Nanoimprint

1. Introduction

Many surgical procedures are now performed using laparoscopes [1]. In many cases, less burdensome laparoscopic surgery has supplanted once predominant open abdominal surgery, which tends to increase patient burdens. As shown in Figure 1, laparoscopic surgery involves puncturing several small holes into the body wall to allow the insertion of laparoscopes, with each hole measuring 5 mm to 10 mm. This surgery has spread rapidly since it is minimally invasive and contributes to the patient' rapid recovery and early reintegration into society [2-16]. For surgeons, however, laparoscopic surgery poses numerous new risks and restrictions not seen with conventional open abdominal surgery. One such issue is the fogging and fouling of the camera lens at the tip of the laparoscope.

A laparoscope is used by inserting a trocar into the abdomen and using this trocar as a guide to insert and advance the laparoscope into the body. To obtain a wide view of the surgical field, the abdominal cavity is inflated with carbon dioxide or other gas using an abdominal wall lift and an insufflator to create space between the abdominal wall and the organs. Typically, bodily fluids and blood will not adhere to the objective lens at the tip of the laparoscope if the laparoscope once inserted is left as it is. However, once an electrocauterizer or other tool is manipulated to excise the affected area, the high temperature generated by the electrocauterizer can cause bodily fluids and blood to vaporize and adhere to the surface of the objective lens. In addition, condensation on the lens caused by temperature differences between the instrument interior and exterior can also obscure vision. Any obstruction of the field of view caused by fogging or fouling of the objective lens with blood, etc. during the surgical procedure must be addressed by cleaning the lens [17,18]. This has generated demand for laparoscopic camera objective lenses that offer antifogging and antifouling properties. Previously, we developed a biliary stent offering antifouling properties, which

Laparoscope monitoring screen

On average, five to six entry ports are formed in the abdomen

Liver

Lymph node

Forceps, etc.

Stomach

Artery

A small incision (of approx. 4 cm) may be made.

Holes measure approx. 5 mm to 1 cm.

Scope

Inside the abdomen

The abdomen is inflated with carbon dioxide gas for surgery.

Laparoscope

Stomach

Abdominal cavity

Caudal

Carbon dioxide gas
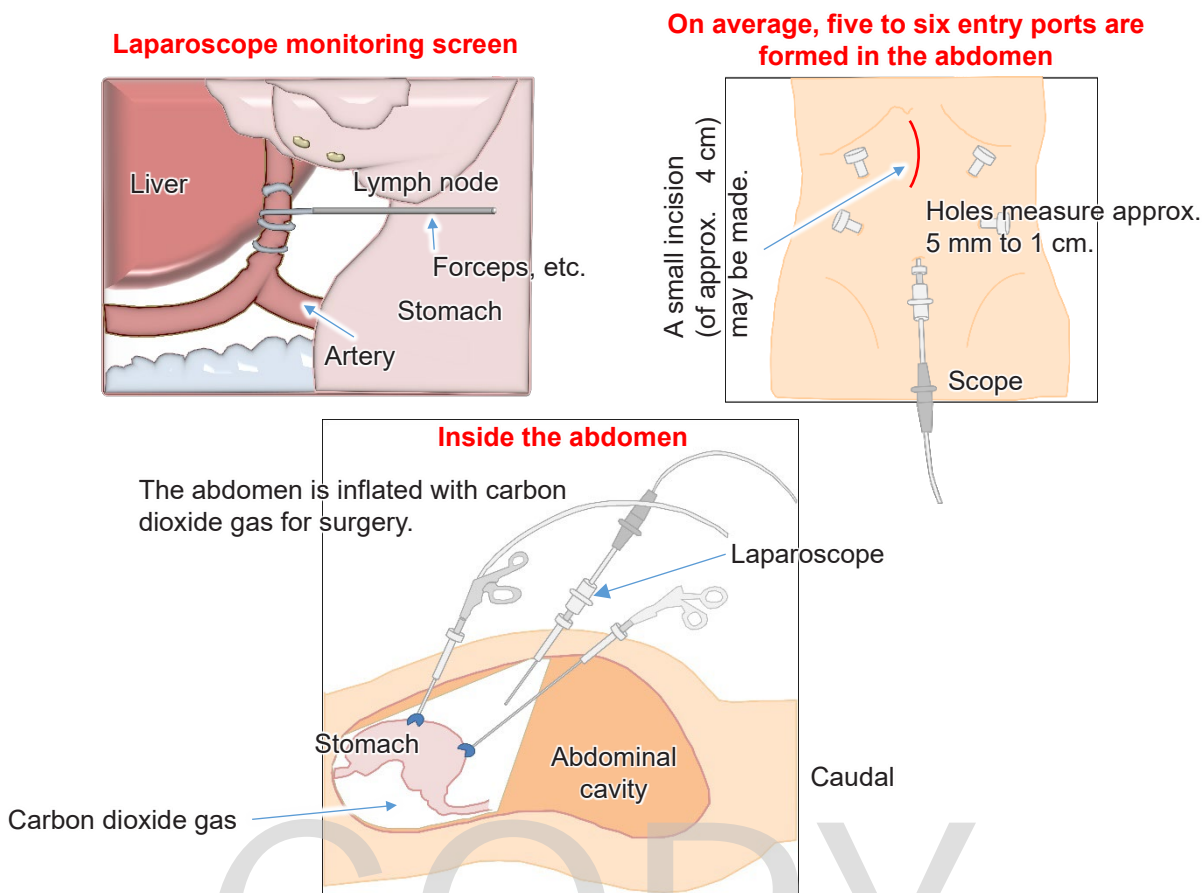
Fig . 1   Schematic illustration of laparoscopic surgery.

we realized by producing a biomimetic structure mimicking the structure of a snail shell and transferring it onto a resin surface [19-25].   This biomimetic structure is well-known for its oil-repelling effects in water (nanoscale ultrahydrophilic properties).   Our current paper reports on the development of an objective lens for laparoscopic cameras with antifogging and antifouling properties based on a super water-repellent mechanism that applies the same biomimicry principles.

2.   Biomimetics and super water-repellent structures

From antiquity, lotus leaves have been known to repel water.   This effect is attributed to the nanostructure on the surface of these leaves, called a double roughness structure (Fig. 2 (a) and Fig. 2 (b)).   The field of technologies based on imitating unique functions observed in nature for industrial applications is known as biomimetics [26-28]. Numerous reports describe industrial applications of the structure observed on lotus leaves.   In this study, we drew on nanoimprint technology to develop a substrate with super water-repellent

properties and apply it to laparoscopic camera lenses (Fig. 3).

3.   Examination of the water repellency of photocurable and thermosetting resins

First, we coated substrates with three types of base resins, which we then cured by irradiation or heating and assessed the water repellency of the surface by measuring contact angles.   Next, we formed a 200 nm dotted pattern on the resin surface using nanoimprint technology [29-32].   We then reassessed the water repellency of the surface to determine whether the nanopattern enhanced water repellency.

The resins tested were as follows:
① Photocurable acrylic resin
    (PAK-01 manufactured
    by Toyo Gosei Co., Ltd.)
② Thermosetting epoxy resin
    (SU-8-3005 manufactured
    by Nippon Kayaku Co., Ltd.)
③ Photocurable acrylic resin
    (AR-1 manufactured
    by Litho Tech Japan Corporation)
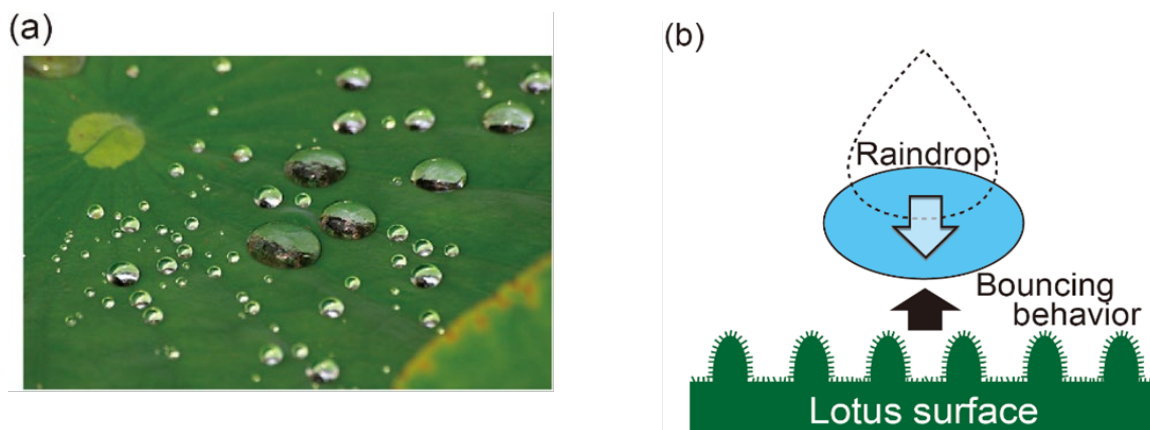
Fig. 2   (a) Water repellency of lotus leaves and (b) underlying mechanism.
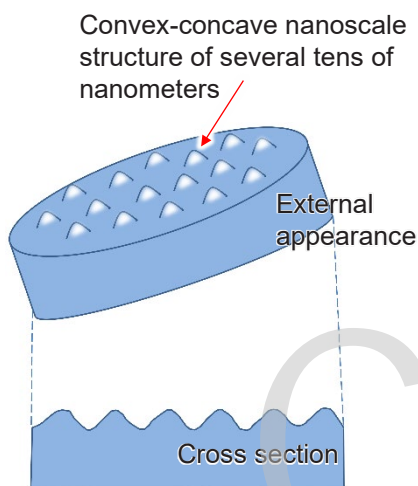
Fig. 3   Schematic view of super water-repellent laparoscope lens incorporating lotus leaf structure.
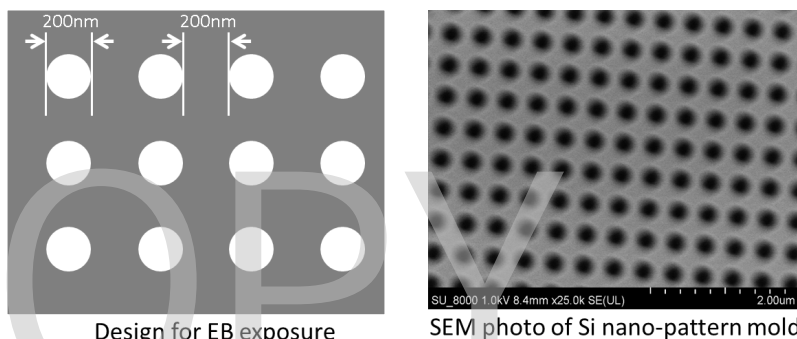
Fig. 4   Mold design and SEM image of Si mold.

Of the above, ① and ② are commercially available products, while ③ is an original resin with the following composition:

PMMA
    (acrylic polymer)   77.8
Dipentaerythritol hexaacrylate
    (multifunctional acrylic monomer)   20.7
1-Hydroxycyclohexyl phenyl ketone
    (photoinitiator)   1.5
                          (weight ratio)

The above ingredients were dissolved in PGMEA and adjusted to prepare a 5% solution.

The mold pattern used to imprint a nanopattern was prepared by producing a 200 nm hole pattern (hole depth: 200 nm; pitch: 400 nm) on Si material using electron beam lithography (Fig. 4) [33].

When transferred, the mold creates a dotted pattern.   The nanoimprinting equipment used was the LTNIP-5000, manufactured by Litho Tech Japan Corporation.

3.1.   PAK-01 (UV curable acrylic resin)
A coat of PAK-01 resin (Toyo Gosei Co., Ltd.) [34] was applied to a quartz substrate and nanoimprinted using the mold with the 200 nm hole pattern.

Transfer conditions:
 PAB: None
 Transfer pressure: 1,000 N
 Filling time: 5 minutes
 Photocuring: 1 minute @10 mW/cm^2
 Exposure wavelength: 365 nm

Figure 5 shows the water repellency of PAK-01 and the results of 200 nm patterning.   The cured PAK-01 coating is hydrophilic.   The contact angle was modest.   Imprinting the 200 nm pattern slightly increased the contact angle.

175

Water repellency of PAK-01

CA＝54.2°

CA＝67.2°

Without 200 nm pattern

With 200 nm pattern

(a) Water repellency of cured coating

Photo of external appearance of 200 nm pattern and SEM image of PAK-01
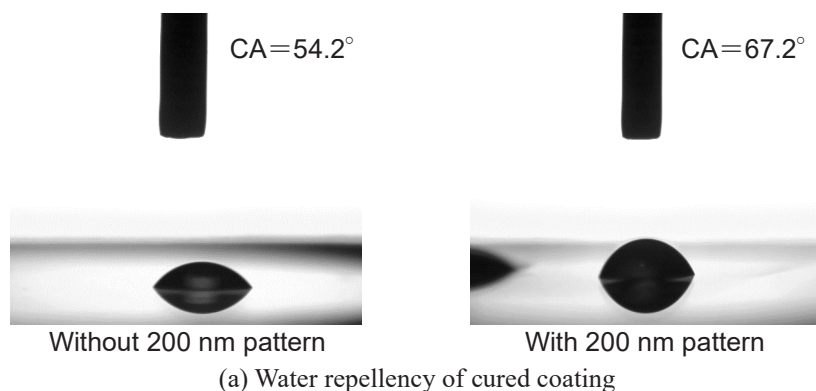
Photo of external appearance

SEM image

(b) Results of 200 nm patterning
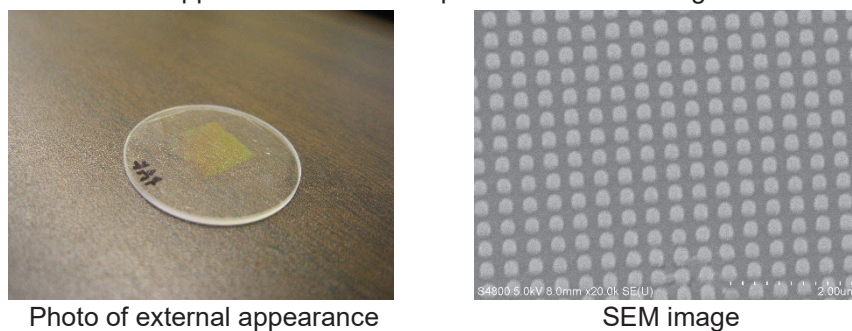
Fig. 5   Water repellency of PAK-01 with and without 200 nm pattern and 200 nm patterning results.

Water repellency of SU-8

CA＝113.3°

CA＝137.3°

Without 200 nm pattern

With 200 nm pattern

(a) Water repellency of cured coating

Photo of external appearance of 200 nm pattern and SEM image of SU-8
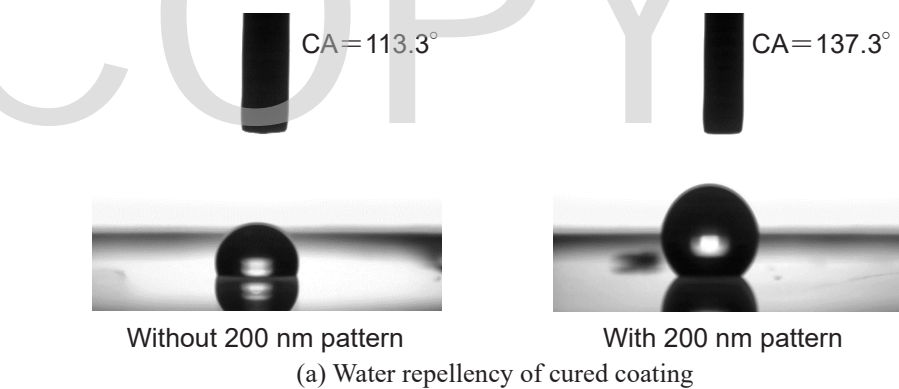
Photo of external appearance

SEM image

(b) Results of 200 nm patterning
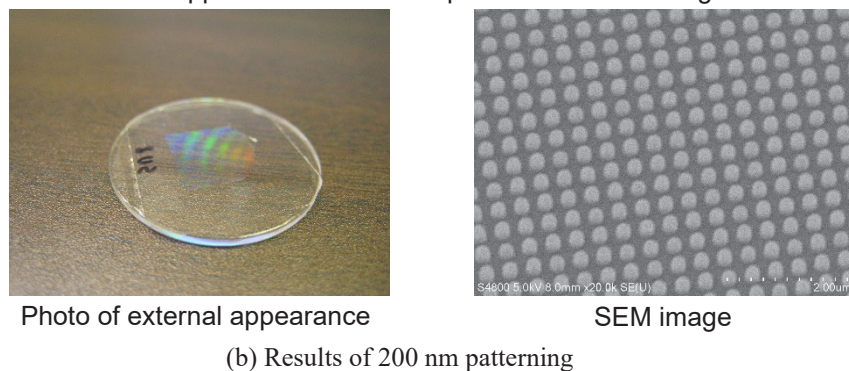
Fig. 6   Water repellency of SU-08 with and without 200 nm pattern and 200 nm patterning results.

3.2. SU-8 (thermosetting epoxy resin)

We applied a coat of SU-8 (Nippon Kayaku Co., Ltd.) [35, 36] to a quartz substrate and nanoimprinted using the 200 nm hole pattern mold. There is a pattern, and it shows the water repellency of a hardened film at the time without a pattern to Fig. 6 (a).

Also, it shows an outward appearance when a pattern is possible and SEM observation result to Fig. 6 (b).

Transfer conditions:
  PAB: 2 minutes @65°C
  Transfer pressure: 3,000 N
  Filling time: 5 minutes
  Photocuring: 1 minute @10 mW/cm^2
  Heat curing condition: 10 minutes @65°C

The cured SU-8 coating is hydrophobic. The contact angle for the coating surface without pattern was 111.3°. The contact angle significantly improved to 137.3° after 200 nm patterning.

3.3. AR-1 (photocurable acrylic resin)

We prepared this photocurable acrylic resin using dipentaerythritol hexaacrylate (Tokyo Chemical Industry Co., Ltd.) as the monomer and adding 1.5% 1-hydroxycyclohexyl phenyl ketone (Tokyo Chemical Industry Co., Ltd.) as the polymerization initiator. This resin was applied to a quartz substrate and nanoimprinted using the 200 nm hole pattern mold. There is a pattern, and it shows the water repellency of a hardened film at the time without a pattern to Fig. 7 (a).

Also, it shows an outward appearance when a pattern is possible and SEM observation result to Fig. 7 (b).

Transfer conditions:
  PAB: None
  Transfer pressure: 1,000 N
  Filling time: 5 minutes
  Photocuring: 10 minutes @10 mW/cm^2
  Exposure wavelength: 365 nm

Since the resin material failed to cure properly, the patterning could not be adequately performed. No further study was made of this resin type.

Water repellency of F-based resin

CA＝113.6°   CA＝112.3°

Without 200 nm pattern   With 200 nm pattern

(a) Water repellency of cured coating
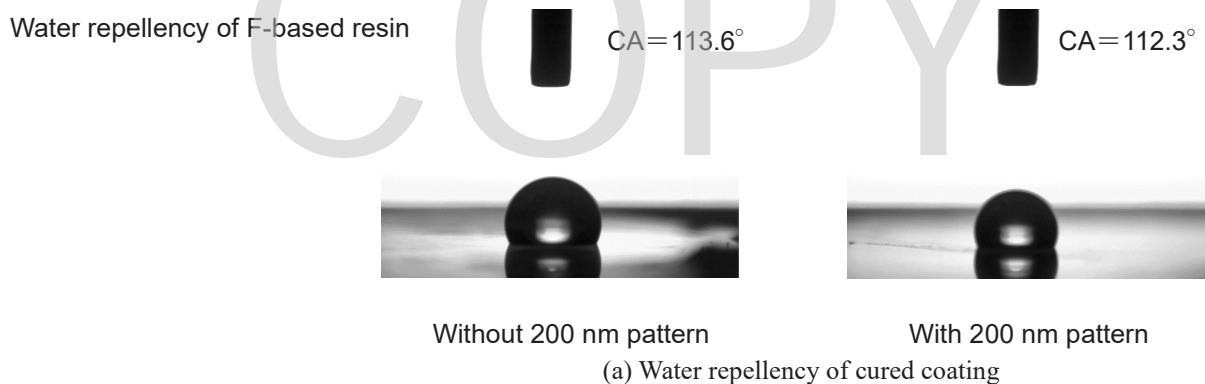
Photo of external appearance of 200 nm pattern and SEM image of F-based resin

Failed patterning?

Photo of external appearance   SEM image

(b) Results of 200 nm patterning
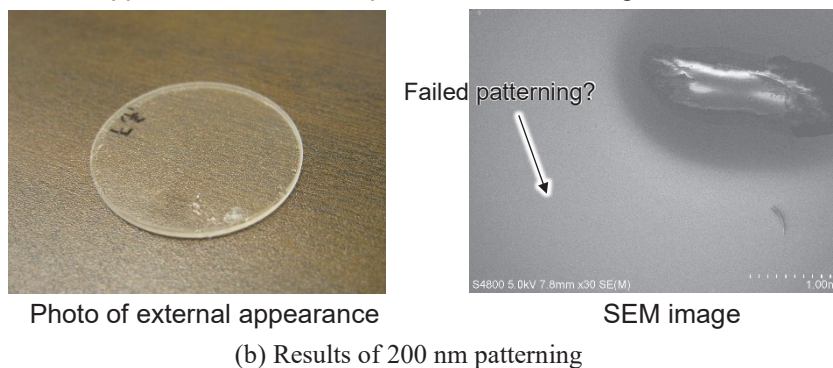
Fig. 7   Water repellency of AR-1 with and without 200 nm pattern and 200 nm patterning results.

F-1   HO—⬡—C(CF₃)₂—⬡—OH

2,2-Bis(4-hydroxyphenyl)hexafluoropropane

F-2   H₂N—⬡—⬡—NH₂

2,2'-Bis(trifluoromethyl)benzidine
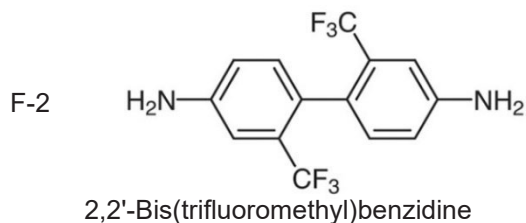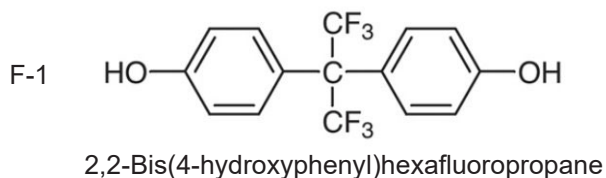
Fig. 8   Structures of F additives.
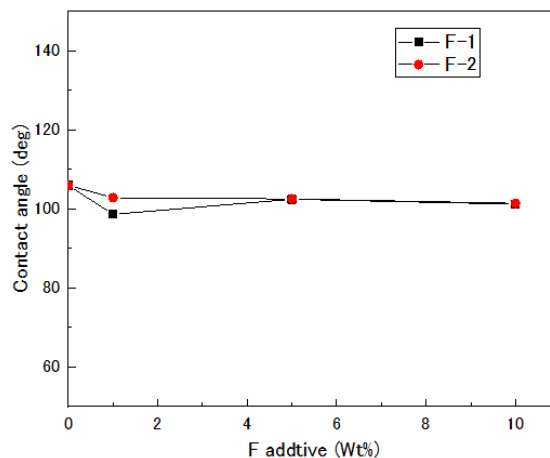
Fig. 9   Effect of F additives on PAK-01.
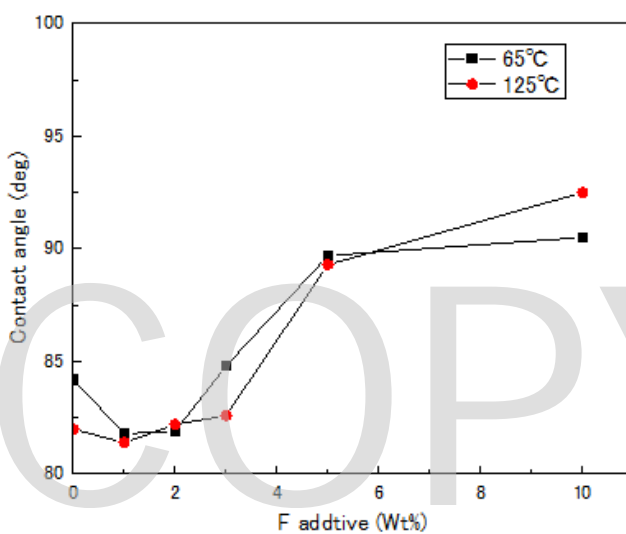
Fig. 10   Effect of F-1 additive on SU-8.
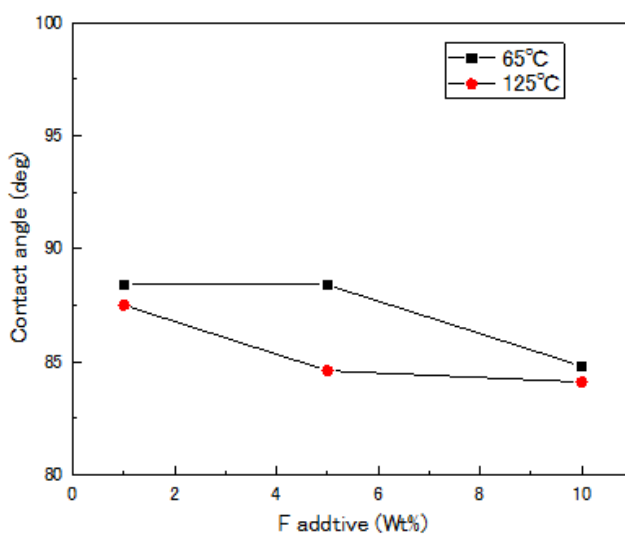
Fig. 11   Effect of F-2 additive on SU-8.

4.   Effects of F additives

Of the three resin types described above, F additives were mixed into the two resins, excluding AR-1, to examine the changes in contact angles for surfaces without the nanoimprinted pattern.   It shows the structural formula of the add-in material

to Fig. 8.

Photocurable acrylic resin
(PAK-01 manufactured
by Toyo Gosei Co., Ltd.)
Thermosetting epoxy resin
(SU-8-3005 manufactured
by Nippon Kayaku Co., Ltd.)

The F additives used were as follows:
F-1: 2,2-Bis(4-hydroxyphenyl)hexafluoropropane
(Tokyo Chemical Industry Co., Ltd.)
F-2: 2,2'-Bis(trifluoromethyl)benzidine
(Tokyo Chemical Industry Co., Ltd.)

4.1. Effect of F additives on PAK-01

Quartz substrates were spin-coated with PAK-01 + F-1 and PAK-01 + F-2 and allowed to stand for two minutes in a vacuum before exposure to UV irradiation (365 nm) for 70 seconds. The amount of F additives was varied from 0% to 10% relative to the resin by weight.

Figure 9 shows the relationship between the amount of F additives and contact angles.

Figure 9 shows the effect of F additives on PAK-01. No improvement in contact angle is evident, even when the amount of F-1 and F-2 additives is increased.

4.2. Effect of F additives on SU-8

Quartz substrates were spin-coated with SU-8 + F-1 and SU-8 + F-2 and subjected to photo and thermal imprinting. This entailed two minutes of UV irradiation, followed by PEB at 65°C, 95°C, and 125°C.

Figure 10 and Figure 11 shows the relationship between the amount of F additives and contact angles.

We found that mixing F-1 additive into SU-8 at increasing concentrations improved contact angle. In contrast, adding F-2 additive failed to improve contact angle, even when the amount of F-2 additive mixed into the resin was increased.

5. Examination of the water repellency of patterned F additive-added resin material

Based on the study up to this point, we found it was possible to achieve super water-repellency by mixing F-1 additive into SU-8 at a weight ratio of 10%. We believe that the application of nanopatterning could enhance the super water-repellency even further.

Figure 12 illustrates the water repellency
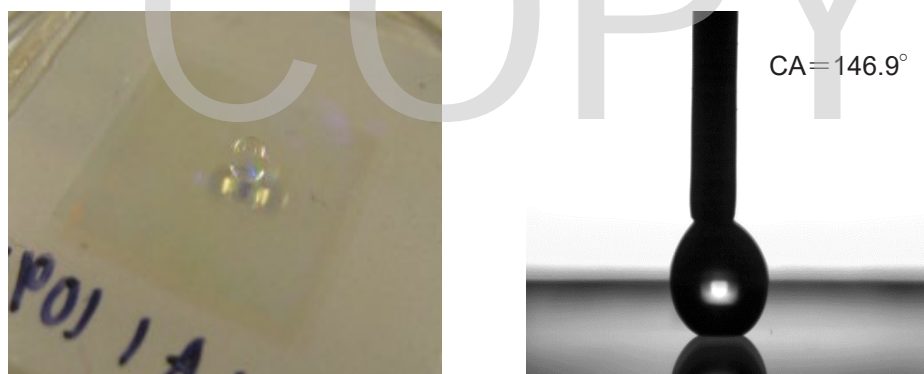
(a) Measuring the contact angle
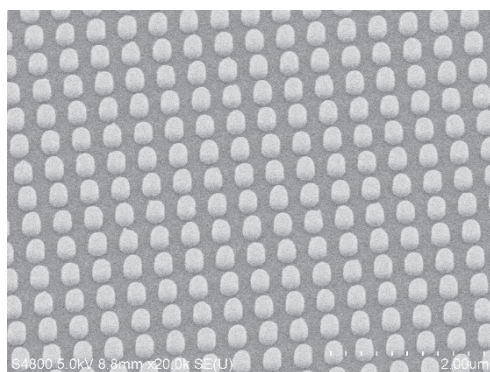
(b) SEM image of 200 nm pattern

Fig. 12   Water repellency of patterned section of SU-8 + 10 % F-1 and 200 nm patterning results.

Before tilting the lens

After tilting the lens

(a) Sliding liquid droplet

(b) Measuring the angle of the sliding liquid droplet
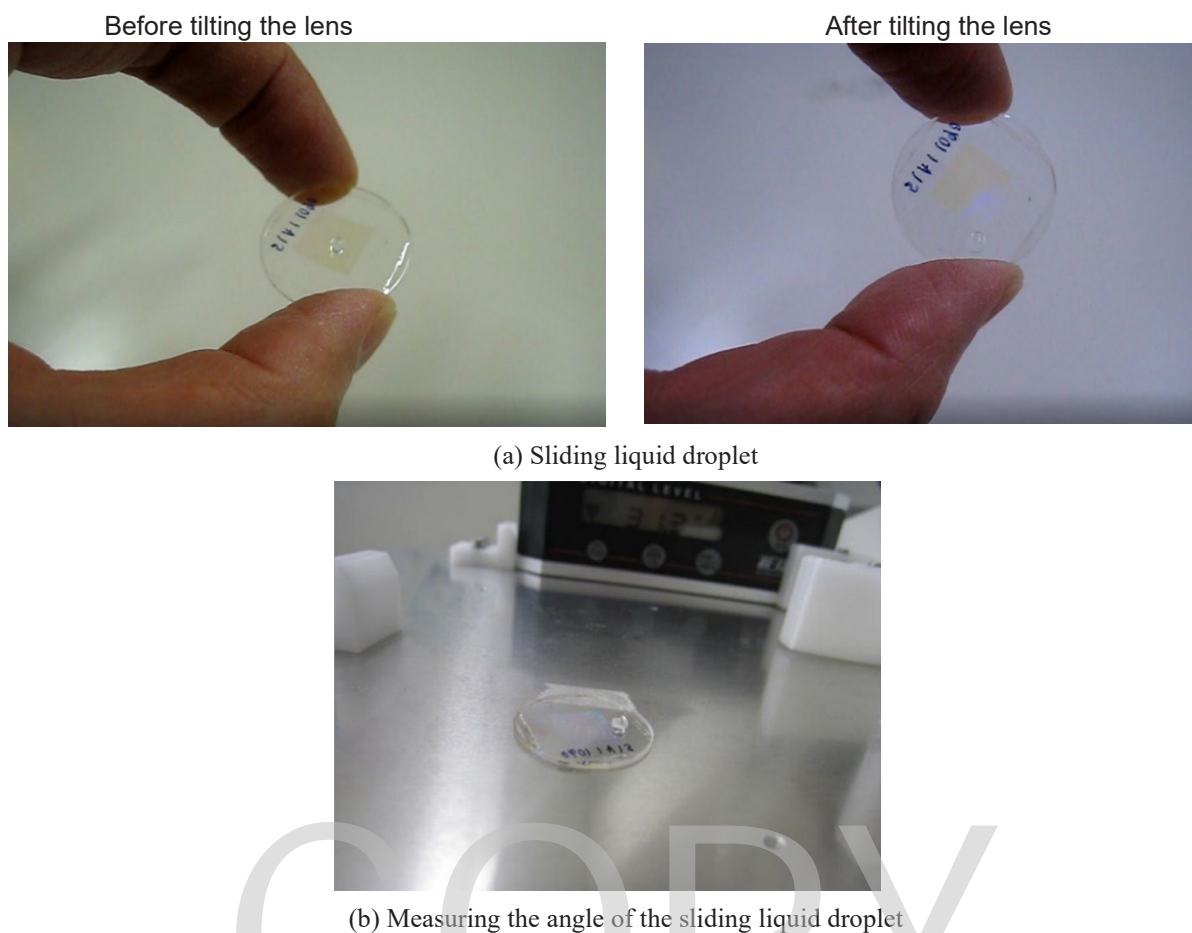
Fig. 13   Sliding angle measurement on a patterned section of SU-8 + 10 % F-1.

With nano-structure

Without nano-structure

Fig. 14   Assessment of self-cleaning effect.

measured on a 200 nm patterned section of SU-8 added with 10 % F-1 additive, along with an SEM image of the section.

The contact angle obtained was 146.9°.   Figure 13 shows how we measured the sliding angle.   The sliding angle obtained was 31.1°.

6.   Self-cleaning effect

We explored whether the self-cleaning effect could be achieved on an untreated substrate and the

present substrate. The substrates were first wetted with water, after which oil droplets were placed on each. The substrate surfaces were then rinsed with water to assess the self-cleaning effect. (Fig. 14)

The results showed that oil could be effectively removed from the 200 nm patterned substrate under running water, proving the high self-cleaning effect.

7. Summary

We achieved a contact angle (CA) of 146.9° and a sliding angle (SA) of 31.3° for a substrate surface coated with a material composed of SU-8 +10 % F-1 and imprinted with a 200 nm pillar pattern. A self-cleaning test confirmed the effectiveness of the surface created. The results confirmed that we could apply this material to laparoscopic camera lenses.

Acknowledgements

References

1. D. Hirata, A. Teramoto, M. Iwatate, S. Hattori, and W. Sano, *Colon cancer perspective 2019*, **Vol. 4 No. 3** (197) 27.
2. U. Ginger, M. Ouaissi, S-F H Schmitz, S. Krähenbühl, and L. Krähenbühlet, *Br J Surg.*, **98** (2011) 391.
3. SI Berríos-Torres,CA Umscheid, DW Bratzler, B. Leas, EC Stone, RR Kelz, CE Reinke, S. Morgan, JS Solomkin, JE Mazuski, EP Dellinger, KM F Itani, EF Berbari, J. Segreti, J. Parvizi, J. Blanchard, G. Allen, JAJW Kluytmans, R. Donlan, and WP Schecter, *JAMA Surg.*, **152** (2017) 784.
4. F. Motoi, S. Egawa, T. Rikiyama, Y. Katayose, and M. Unno, *Br J Surg.*, **99** (2012) 524.
5. MK Diener, CM Seiler, I. Rossion, J. Kleeff, M. Glanemann, G. Butturini, A. Tomazic, CJ Bruns, ORC Busch, S. Farkas, O. Belyaev, JP Neoptolemos, C. Halloran, T. Keck, M. Niedergethmann, K. Gellert, H. Witzigmann, O. Kollmar, P. Langer, U. Steger, J. Neudecker, F. Berrevoet, S. Ganzera, MM Heiss, SP Luntz, T. Bruckner, M. Kieser, and M. W. Büchler, *Lancet*, **377(9776)** (2011) 1514.
6. NA Hamilton, MR Porembka, FM Johnston, F. Gao, SM Strasberg, DC Linehan, and WG Hawkins, *Ann Surg.*, **255(6)** (2012) 1037.
7. M. Kawai, S. Hirono, K. Okada, M. Sho, Y. Nakajima, H. Eguchi, H. Nagano, H. Ikoma, R. Morimura, Y. Takeda, S. Nakahira, K. Suzumura, J. Fujimoto, and H. Yamaue, *Ann Surg.*, **264(1)** (2016) 180.
8. M. Kawai, S. Hirono, K. Okada, S. Satoi, H. Yanagimoto, M. Kon, Y. Murakami, N. Kondo, M. Sho, T. Akahori, H. Toyama, T. Fukumoto, T. Fujii, I. Matsumoto, H. Eguchi, H. Ikoma, Y. Takeda, J. Fujimoto, and H. Yamaue, *Langenbecks Arch Surg.*, **402(8)** (2017) 1197.
9. I. Karabicak, S. Satoi, H. Yanagimoto, T. Yamamoto, S. Yamaki, H. Kosaka, S. Hirooka, M. Kotsuka, T. Michiura, K. Inoue, Y. Matsui, and M. Kon, *Pancreatology*, **17(3)** (2017) 497.
10. A. Nakao and H. Takagi, *Hepato-Gastroenterol*, **40** (1993) 426.
11. A. Nakao, *Dig Surg.*, **33(4)** (2016) 308.
12. S. Hirono and H. Yamaue, *J Hepatobiliary Pancreat Sci.*, **22** (2015) E4.
13. S. Hirono, M. Kawai, K. Okada, M. Miyazawa, A. Shimizu, Y. Kitahata, M. Ueno, T. Shimokawa, A. Nakao, and H. Yamaue, *Ann Gastroenterol Surg.*, **1(3)** (2017) 208.
14. A. Kakita, M. Yoshida, and T. Takahashi, *J Hepatobiliary Pancreat Surg.*, **8** (2001) 230.
15. A. Kleespies, M. Rentsch, H. Seeliger, M. Albertsmeier, and K-W Jauch, C J Bruns, *Br J Surg.*, **96** (2009) 741.
16. T. Fujii, H. Sugimoto, S. Yamada, M. Kanda, M. Suenaga, H. Takami, M. Hattori, Y. Inokawa, S. Nomoto, M. Fujiwara, and Y. Kodera, *J Gastrointest Surg.*, **18** (2014) 1108.
17. T. Utsumi, Y. Sano, M Iwatate, H. Snakawa, A. Teramoto, D. Hirata, S. Hattori, W. Sano, N. Hasuike, K. Ichikawa and T. Fujimori, *World Gastrointest Oncol 2018 April 15*, **10(4)**, 96-102.
18. Y. Sano, H. Chiu, X. Li, S. Khomvilai, P. Pisespongsa, J. Co, T. Kawamura, N. Kobayashi, S. Tanaka, D. Hewett, Y. Takeuchi, K. Imai, T. Utsumi, A. Teramoto, D. Hirata, M. Iwatate, R. Singh, S. Ng, S. Ho, P. Chiu, and H. Tajiri, *Digestive Endoscopy 2019*, **31** (2019) 227.
19. A. Sekiguchi, T. Nishino, M. Aikawa, Y. Matsumoto, H. Minami, K. Tokumaru, F. Tsumori, and H. Tanigawa, *J. Pohotopolym. Sci. Technol.*, **32** (2019) 373.
20. A. Sekiuchi, T. Nishino, H. Tanigawa, H.Minami, Y. Matsumoto, and H. Mayama, *J. Pohotopolym. Sci. Technol.*, **33** (2020) 205.
21. A. Sekiguchi, M. Yamamoto, T. Kumagai, Y. Mori, H. Minami, M. Aikawa, and H. Horibe, *J. Pohotopolym. Sci. Technol.*, **34** (2021) 401.

22. M. Yamamoto, Y. Mori, T. Kumagai, A. Sekiguchi, Hi, Minami, and H. Horibe, *J. Pohotopolym. Sci. Technol.*, **34** (2021) 385.

23. A. Sekiguchi, *C & I commun Vol46*, No.4 2020 1.

24. A. Sekiguchi, and H. Minami, *J. Photopolym. Sci. Technol.*, **35** (2022) 241.

25. M. Yamamoto, T. Hamasaki, A. Sekiguchi, H. Minami, M. Aikawa, and H. Horibe, *J. Photopolym. Sci. Technol.*, **35** (2022) 233.

26. M. Shimomura, "Biomimetics, National Science Museum16", *Tokai University Press*, **2** (2016).

27. R. N. Wenzel, *Ind. Eng. Chem.*, **28** (1936) 988.

28. Y. C. Jung and B. Bhushan, *J. Microsc.*, **229** (2008) 127.

29. A. Sekiguchi, Y. Kono, and Y. Hirai, *J. Photopolym. Sci. Technol.*, **18** (2005) 543.

30. M. Komuro, J. Taniguchi, S. Inoue, N. Kimura, Y. Tokano, H. Hiroshima, and S. Matsui, *Jpn. J. Appl. Phys.*, **39** (2000) 7075.

31. H. Hiroshima1, S. Inoue, N. Kasahara, J. Taniguchi, I. Miyamoto, and M. Komuro, *Jpn. J. Appl. Phys.*, **41** (2002) 4173.

32. Y. Hirai, S. Yoshida, A. Okamoto, Y. Tanaka, M. Endo, S. Irie, H. Nakagawa, and M. Sasago, *J. Photopolym. Sci. Technol.*, **14** (2001) 457.

33. M. Shinji, O. Yukinori, and Y. Hiroshi, *Jpn. J. Appl. Phys.*, **70(4)** (2001) 411.

34. N. Sakai and T. Hirasawa, *kobunshi*, **66** (2009) 88.

35. A. Sekiguchi, Y. Kono, and Y. Hirai, *J. Photopolym. Sci. Technol.*, **18** (2005) 543.

36. A. Sekiguchi, Y. Kono, S. Mori, N. Honda, and Y. Hirai, *Proc. SPIE*, **6151** (2006) 61512H.

Nanoimprint Lithography and Microinjection Molding Using Gas-Permeable Hybrid Mold for Antibacterial Nanostructures

Sayaka Miura[1], Rio Yamagishi[1], Naoto Sugino[2], Yoshiyuki Yokoyama[3], Riku Miyazaki[1], Kaori Yasuda[1], Mano Ando[1], Yuna Hachikubo[1], Tsugumi Murashita[1], Takao Kameda[2], Yuki Kawano[3], and Satoshi Takei[1*]

[1] *Department of Pharmaceutical Engineering,*
Toyama Prefectural University, Imizu, Toyama 939-0398, Japan
[2] *Futuristic Technology Department, Sanko Gosei, Nanto, Toyama 939-1852, Japan*
[3] *Toyama Industrial Technology Research and Development Center,*
Takaoka, Toyama 933-0981, Japan
*takeis@pu-toyama.ac.jp

Biomimetic antibacterial nanostructures with a height of approximately 310 nm and a bottom diameter of approximately 240 nm were fabricated by microinjection molding for practical mass production in the fields of biology, electronic engineering, and life science. The gas-permeable hybrid mold fabricated by nanoimprint lithography was used as the mold for microinjection molding to improve the incomplete filling and molding defects caused by gas entrainment in cavities during microinjection molding. One same mold could be used repeatedly without cleaning for 200 injection molding cycles. Antibacterial activity evaluation showed that that the antibacterial activity of the fabricated biomimetic antibacterial nanostructures was 15% greater than that of a flat surface. This work establishes the advanced processing technology of high-resolution nanostructures by microinjection molding with the gas-permeable hybrid mold.
Keywords: Nanoimprint lithography, Microinjection molding, Gas-permeable mold, Antibacterial structures, Advanced processing technology

1. Introduction

In recent years, the COVID-19 pandemic and antibiotic resistance have become challenges for public health agencies worldwide, increasing the demand for antibacterial materials that prevent bacterial infections by inhibiting primary bacterial adhesion and killing bacteria [1,2]. Antibacterial materials include catechin; chitosan; and metal compounds, such as silver, copper, and titanium dioxide [3-5]. In contrast to common antibacterial materials, such as biocides, paints, and abrasives containing toxic and rare metal species, the above materials are considered environmentally friendly because they do not release contaminants into the environment [6]. In particular, silver nanoparticles have been introduced for biomedical applications due to their numerous advantages, such as good antibacterial activity, excellent biocompatibility, and satisfactory stability [7]. These advantages are due to the higher surface area than volume of silver nanoparticles that allows for sustained contact with bacteria and more potent antibacterial activity [8]. However, the widespread use of silver nanoparticles has raised concerns that silver nanoparticle-resistant bacteria may develop due to long-term exposure to silver nanoparticles [9]. Moreover, reports of the adverse effects of silver nanoparticles on higher organisms, including humans [10], have warranted caution against their widespread use [11].

Against this background, several studies have explored physical alternatives to killing bacteria chemically through the contact antibacterial mechanism [12,13]. A schematic of how nanostructures kill bacteria is shown in Fig. 1.

Developing a surface expressing physical antibacterial activity by fabricating nanostructures without using chemical antibacterial materials that affect the environment and human body is of high priority [14]. Recent studies from a biomimetic perspective have focused on the physical antibacterial activity of the nanostructures in the wings of insects, such as dragonflies and cicadas, that penetrate bacterial cell walls [15,16]. Biomimetically engineered nanostructures on black silicon have also demonstrated antibacterial activity against a variety of bacterial species [17].
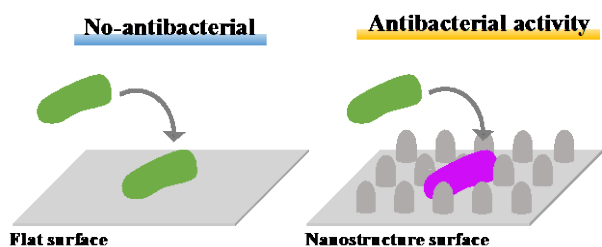
Fig. 1.   Ways in which nanostructures can kill bacteria.

Bright et al. reported that nanostructured titanium alloy fabricated via a hydrothermal etching process executed antibacterial activity against Staphylococcus aureus and Pseudomonas aeruginosa [18]. Dickson et al. synthesized nanopillared surfaces on poly (methyl methacrylate) through nanoimprint lithography. They found that the nanopillared surfaces were effective in killing *Escherichia coli*, a Gram-negative bacterium, and increased the killing rate of attached bacteria by 16%–141% [19]. In addition, nanostructure–cell interactions have been observed to behave differently with different sizes and shapes and many studies have shown that nanostructures with high aspect ratios have effective antibacterial activity [20].

Thus, the motivation of our study is to explore the use of versatile microinjection molding utilizing a gas-permeable hybrid mold with a nanoimprinted surface for defect reduction to fabricate biomimetic nanostructures that express antibacterial activity through a physical approach. Our previous studies demonstrated that the application of gas-permeable molds with porous molecule design improves microstructural defects [21-23]. Microinjection molding is used for practical large-scale production in many fields due to its short cycle time and relatively low cost per part [24,25]. This method is a novel technology given that only a few previous studies have used it to create nanostructured antibacterial materials. For preventing the

incomplete filling of nanostructures and defects due to the entrainment of gases in cavities during the microinjection molding of biomimetic antibacterial nanostructures [26,27], a gas-permeable hybrid mold fabricated by nanoimprint lithography [28,29] was used and evaluated.

2. Experimental

2.1. Fabrication of the gas-permeable surface material in the gas-permeable hybrid mold

The gas-permeable surface material was bonded to the gas-permeable substrate described below to form the gas-permeable hybrid mold. The chemical structures of the prepared gas-permeable surface material in the gas-permeable hybrid mold and the mechanism of the cross-linking reaction under ultraviolet (UV) irradiation is shown in Fig. 2. A sol–gel copolymer (Fig. 2, a) with four components, namely, 40 wt% 3-(acryloyloxy) propyl trimethoxysilane, 35 wt% methyltrimethoxysilane, 15 wt% tetraethyl titanate, and 10 wt% tetraethoxysilane, was synthesized by using sol–gel polymerization [30-32]. The 87 wt% sol–gel copolymer was added with 2,4,6,8-tetramethyl-2,4,6,8-tetravinylcyclotetrasiloxane (T2523: Tokyo Chemical Industry) (Fig. 2, b) as a cross-linking agent. Then, 3 wt% 2-hydroxy-2-methyl-1 phenilpropanone (Omnirad 1173: Toyotsu Chemiplas) (Fig. 2, c) was added as a UV-radical polymerization initiator to the sol–gel copolymer and cross-linking agent. The mixture was next mixed with a roller stirrer (MR-5: AS ONE) for 8 h. The structure of the gas-permeable surface material is shown in Fig. 2, d. Reticulated chains and ring structures formed a porous structure and conferred the surface material with gas permeability.

2.2. FT-IR spectroscopy of the gas-permeable surface material

The structural changes of the gas-permeable surface material caused by the UV cross-linking reaction were confirmed before and after UV irradiation by Fourier transform infra-red spectroscopy (FT-IR). Measurements were performed by using an FT-IR system (Spectrum Two: Perkin Elmer). Recording was performed with a resolution of 4 cm^{-1}, the number of integrations of 10, and a frequency range of 400–4000 cm^{-1}. The measurement was performed on the materials prepared through surface irradiation with UV light (25 mW/cm^2) (LC8: Hamamatsu Photonics) for 0, 30, or 60 s.
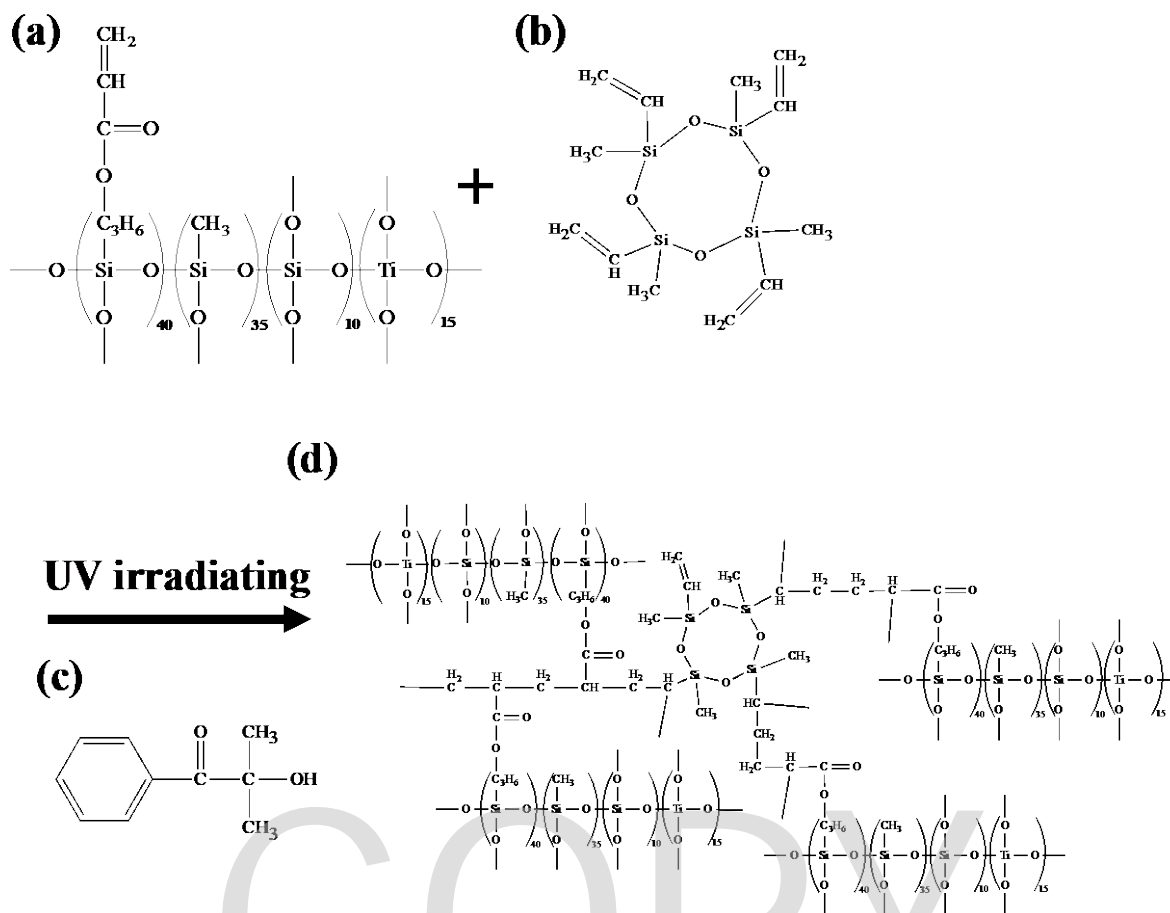
Fig. 2. Chemical structure and reaction of gas-permeable surface material: (a) sol–gel copolymer, (b) cross-linking agent, (c) UV-radical polymerization initiator, and (d) gas-permeable surface material.

2.3. Fabrication of the gas-permeable substrate in the gas-permeable hybrid mold

The metal photoengraving composite processes for the fabrication of the gas-permeable substrate in the gas-permeable hybrid mold was performed by using a metal photoengraving composite processing machine (LUMEX Avance-25: Matsuura Machinery) [33,34]. The laser fabrication chamber was filled with nitrogen gas to prevent oxidation during the melting of the materials. Standard maraging steel powders with an average particle size of 20–30 μm were baked and hardened under irradiation with a 400 W Yb fiber laser and the shape was cut. This series of operations was repeated to produce the gas-permeable substrate. The gas-permeable substrate was ultrasonically cleaned with acetone for 20 min in an ultrasonic cleaner (US-101: SND), then vacuum-dried at 180 ℃ for 20 min in a vacuum dryer (AVO-250SB: AS ONE) to remove the lubricants and other oils used in the metal photoengraving composite processes.

2.4. Nanoimprint Lithography of the Gas-permeable Surface Material in the Gas-permeable Hybrid Mold

The fabrication method for the gas-permeable hybrid mold spliced with the gas-permeable surface material and gas-permeable substrate is shown in Fig. 3, a. This quartz master mold had a nanostructure with a height of 309 nm and bottom diameter of 236 nm. The quartz master mold was treated with a mold release agent (DURASURF DS-831TH: Harves) to release it from the gas-permeable surface material. The gas-permeable surface material was placed on the gas-permeable substrate and pressed with the quartz master mold. UV irradiation for the polymerization of the gas-permeable surface material was then performed by using a UV light (25 mW/cm²) (LC8: Hamamatsu Photonics) for 60 s. The quartz master mold was released from the surface of the gas-permeable surface material in the gas-permeable hybrid mold. The surface with the inverted nanostructures was fabricated in the gas-permeable hybrid mold for the next step of microinjection molding.
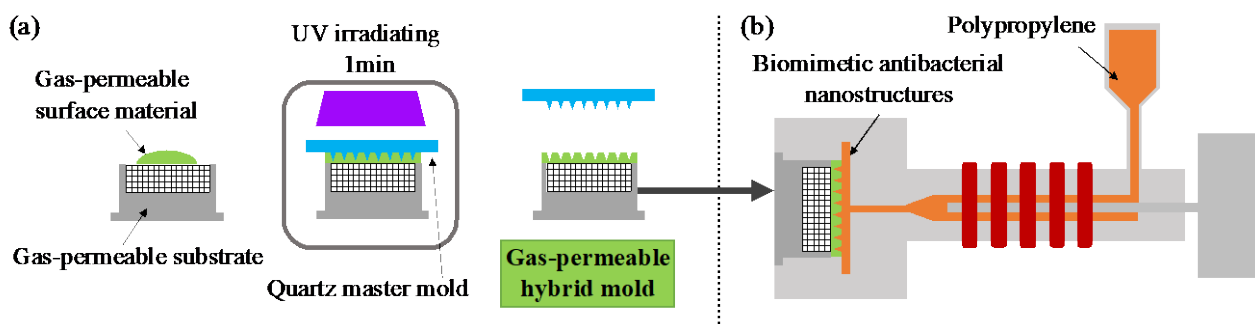
Fig. 3.　(a) Fabrication of gas-permeable hybrid mold by nanoimprint lithography and (b) fabrication of biomimetic antibacterial nanostructures by microinjection molding.

2.5. Microinjection molding utilizing the gas-permeable hybrid mold with nanostructures

The microinjection molding of the above inverted nanostructures from the gas-permeable hybrid mold into polypropylene (PP) (NOVATEC-PP BC03B: Japan Polypropylene) is shown in Fig. 3, b. A microinjection molding machine (Model GL150: Sodick) with a screw preplasticating system was used. The fabricated gas-permeable hybrid mold was placed on a flat plate for shrinkage measurement and 400 injection molding cycles were performed. The basic parameters of the microinjection molding conditions included filling speed (17.5 mm/s), melt temperature (220 ℃), molding temperature (30 ℃), holding pressure (20 MPa), holding pressure time (10 s), and cooling time (20 s).

2.6. Evaluation of antibacterial activity

Antibacterial activity was evaluated by using the PP-derived biomimetic antibacterial nanostructures (approximate height of 300 nm and bottom diameter of 220 nm) with an area of 20 mm × 20 mm molded by microinjection molding. The method for antibacterial activity evaluation is presented in Fig. 4. The antibacterial activities against *E. coli* of the biomimetic antibacterial nanostructures derived from PP and a flat surface were compared. *E. coli* JM109 was cultured in NB medium at 37 ℃ for 16 h. The bacterial suspension was centrifuged at 5000 g for 10 min. Then, its supernatant was discarded. Next, 1 mL of 1/500 nutrient broth (NB) medium was added and the suspension was pipetted. The suspension was diluted 200-fold with 1/500 NB medium to prepare a bacterial suspension for seeding. The bacterial suspension was placed on the biomimetic antibacterial nanostructures or the flat surface and the droplet was covered with polyethylene film. Samples were incubated at 37 ℃ with a relative humidity of 95%. After 24 h of incubation, each surface was rinsed with

Mueller–Hinton Broth (08931: Kyokuto Pharmaceutical Industrial) to harvest the bacteria. The number of viable bacterial cells in the harvested solutions was measured by using Microbial Viability Assay Kit-WST (M439: Dojindo).
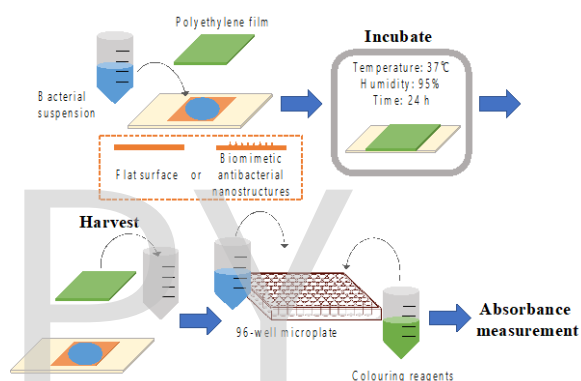
Fig. 4.　Methods for antibacterial activity evaluation.

3. Results
3.1. FT-IR spectroscopic analysis of the gas-permeable surface material

The dependence of the FT-IR spectra of the gas-permeable surface material on UV irradiation time is shown in Fig. 5. We used the 1720 cm^{-1} band assigned to C=O stretching to normalize the obtained infra-red spectra. The main spectral region of interest for the copolymerization reaction of vinyl groups in the gas-permeable surface material was the C=C stretching vibration from 1680 cm^{-1} to 1620 cm^{-1}, the C=C stretching vibrations of α,β-unsaturated carbonyl compounds from 1640 cm^{-1} to 1590 cm^{-1}, and the C–H stretching vibration from 3000 cm^{-1} to 2840 cm^{-1}.

The spectrum of the gas-permeable surface material presented some typical peaks at 1635 and 1619 cm^{-1} (C=C bond). The absorption maximum of C=C in the gas-permeable surface material decreased through the copolymerization of vinyl
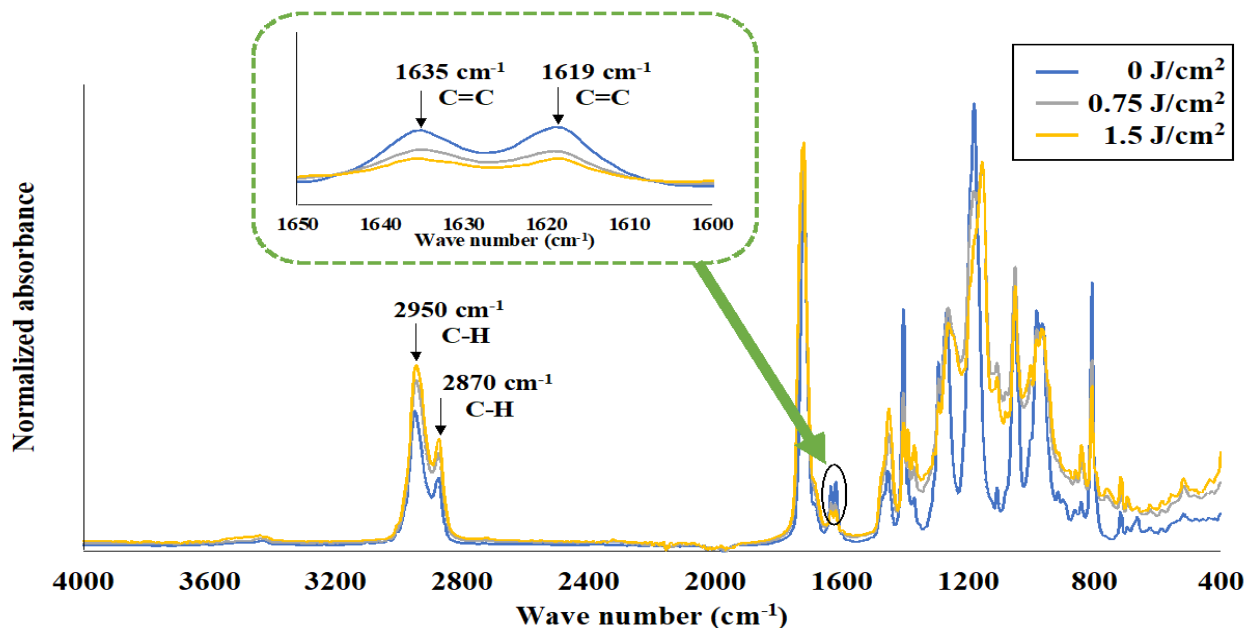
Fig. 5.   FT-IR spectra before and after UV irradiation of gas-permeable surface material (0.75 and 1.5 J/cm^2).

groups under UV irradiation. In particular, the peak of 1635 cm^{-1} showed a reduction of 45% at 0.75 J/cm^2 and 64% at 1.5 J/cm^2. In addition, the absorption maximum of C–H (2950 and 2870 cm^{-1}) increased under UV irradiation. These changes indicated that the gas-permeable surface material was synthesized.

The physical distance between molecules was considered to be responsible for gas permeability given that approximately 36% of the C=C bonds remained at 1.5 J/cm^2. Thus, FT-IR confirmed the polymerization of the gas-permeable surface material.

3.2. Fabrication of biomimetic antibacterial nanostructures by microinjection molding using the nanoimprinted surface of the gas-permeable hybrid mold

The scanning probe microscope images of (a) the quartz master mold; (b) the gas-permeable hybrid mold fabricated via nanoimprint lithography; and (c) the biomimetic antibacterial nanostructures derived from PP at the fifth, 50th, 200th, and 400th injection molding processes using one gas-permeable hybrid mold without cleaning for up to 400 times are shown in Fig. 6. The result of microinjection molding directly from a quartz master mold without a gas-permeable hybrid mold is provided as the reference in Fig. 6. This material showed molding defects. The surface of the gas-permeable surface material fabricated in the gas-

permeable hybrid mold transferred from the quartz master mold was inverted clearly and the biomimetic antibacterial nanostructures synthesized by using the fabricated gas-permeable hybrid mold were also well molded. Furthermore, no significant difference in molding defects was found between the 5th and 200th cycle of injection molding. Although some molding defects were observed at the 400th cycle, they were not considered to be a problem for the antibacterial materials. PP, a typical general-purpose plastic, was filled into the tip of the nanostructure in the gas-permeable hybrid mold and the use of the gas-permeable hybrid mold improved molding defects compared with that of the conventional quartz master mold. In the future, we will optimize the microinjection molding conditions, study the gas-permeable surface material, and aim to create biomimetic antibacterial nanostructures by performing microinjection molding for more than 200 times with the same mold without cleaning.

3.3. Evaluation of antibacterial activities on the fabricated biomimetic antibacterial nanostructures

The results of the antibacterial activity evaluation of the biomimetic materials are shown in Fig. 7. They were normalized against the results of the control samples tested under the same conditions. The number of viable bacteria on the biomimetic antibacterial nanostructures derived from PP had obviously reduced compared with that on the flat
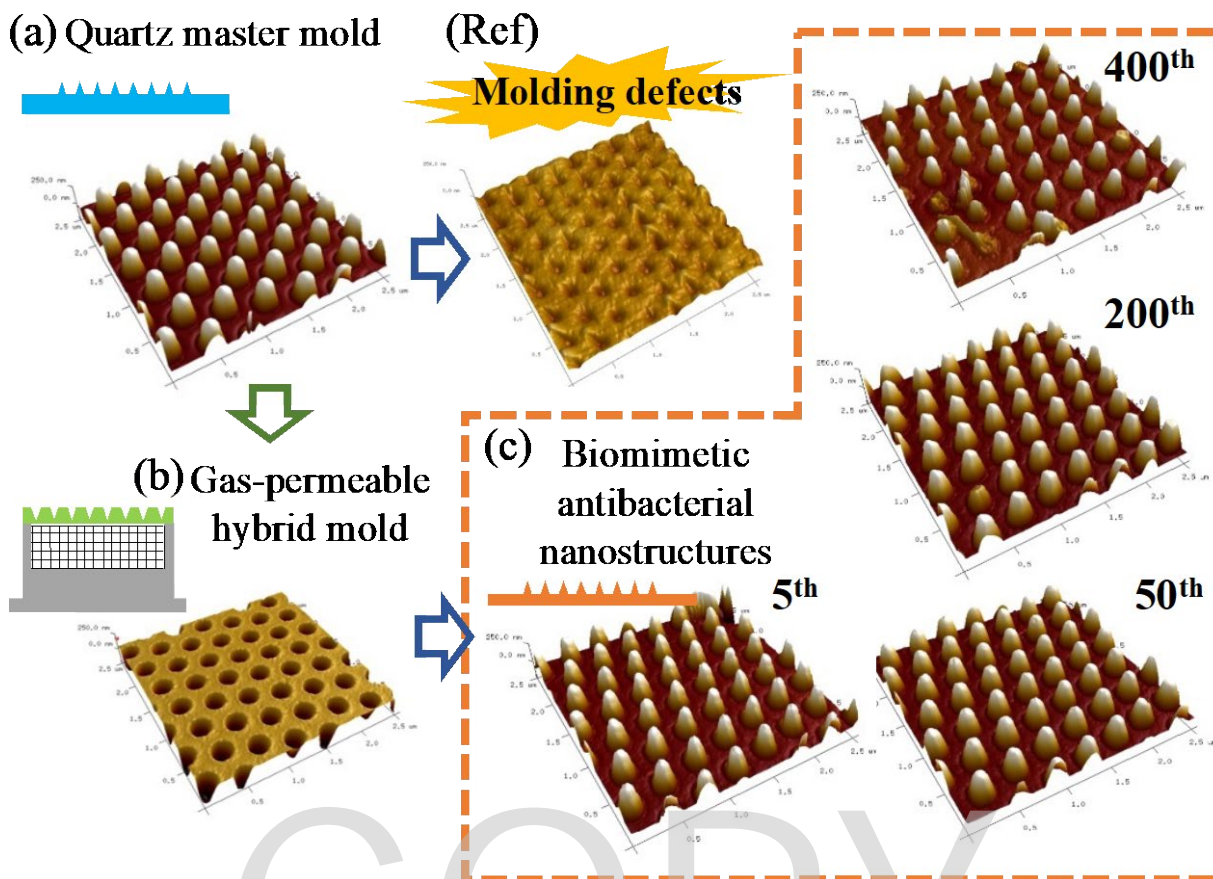
Fig. 6.   Scanning probe microscope images: (a) quartz master mold; (b) gas-permeable hybrid mold prepared through nanoimprint lithography; (c) biomimetic antibacterial nanostructures fabricated by microinjection molding at the fifth, 50th, 200th, and 400th cycles; and (Ref) molding defects created by microinjection molding.

surface. Furthermore, the ratio of the number of viable bacteria on the biomimetic antibacterial nanostructures had reduced by approximately 15% compared with that on the flat surface. The microinjection-molded biomimetic antibacterial nanostructures were speculated to exhibit antibacterial activity due to the tensile force exerted on the cell membranes of *E. coli* in the voids of the nanostructures. This tensile force caused the membranes to break and intracellular fluid to leak out.

Antibacterial materials developed through physical processes are expected to have medical applications as biomaterials, such as materials for the surfaces of dental devices [35]. In particular, the PP used in this work's injection molding process is a biocompatible resin [36] that may provide a solution to the challenges of orthopedic implants, such as infections caused by bacterial biofilm formation. In the future, we will study the differences in antibacterial activity due to variations in the height and pitch of the nanostructures and investigate the structure with the optimal antibacterial activity.
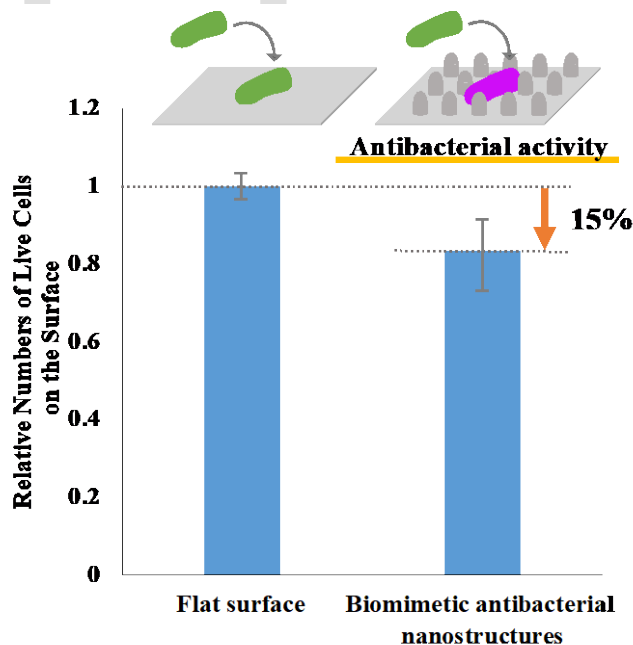
Fig. 7.   Results of antibacterial activity evaluation.

4. Conclusion

We investigated a fabrication method for biomimetic nanostructures with antibacterial activity by using the two microfabrication processes of nanoimprint lithography and microinjection molding with a gas-permeable hybrid mold. The molding defects caused by gas impermeability during microinjection molding were solved by using the gas-permeable hybrid mold. The evaluation of antibacterial activity using *E. coli* demonstrated that the nanostructures expressed approximately 15% more antibacterial activity than the flat surface. This work shows the advanced processing technology of microstructures and has the potential to contribute to research on the creation of antibacterial materials through physical approaches.

Acknowledgement

References

1. S. N. Riduan and Y. Zhang, *Acc. Chem. Res.*, **54** (2021) 4508.
2. Y. K. Jo, J. H. Seo, B. H. Choi, B. J. Kim, H. H. Shin, B. H. Hwang, and H. J. Cha, *ACS Appl. Mater. Inter.*, **6** (2014) 20242.
3. N. Gugala, J. Lemire, K. Chatfield-Reed, Y. Yan, G. Chua, and R. J. Turner, *Genes*, **9** (2018) 344.
4. J. A. Lemire, L. Kalan, A. Bradu, and R. J. Turner. Antimicrob, *Agents Chemother.*, **59** (2015) 4031.
5. M. Veerapandian, S. Sadhasivam, J. Choi, and K. Yun, *Chem. Eng. J.*, **209** (2012) 558.
6. M. Yasuyuki, K. Kunihiro, S. Kurissery, N. Kanavillil, Y. Sato, and Y. Kikuchi, *Biofouling*, **26** (2010) 851.
7. M. A. Massa, C. Covarrubias, M. Bittner, I. A. Fuentevilla, P. Capetillo, A. Von Marttens, and J. C. Carvajal, *Mater. Sci. Eng. R Rep.*, **C 45** (2014) 146.
8. D. M. Eby, H. R. Luckarift, and G. R. Johnson, *ACS Appl. Mater. Inter.*, **1** (2009) 1553.
9. C. Gunawan, W. Y. Teoh, C. P. Marquis, and R. Amal, *Small*, **9** (2013) 3554.
10. B. S. Atiyeh, M. Costagliola, S. N. Hayek, and S. A. Dibo, *Burns*, **33** (2007) 139.
11. C. Marambio-Jones and E. M. Hoek, *J Nanopart Res.*, **12** (2010) 1531.
12. A. Tripathy, P. Sen, B. Su, and W. H. Briscoe. *Adv. Colloid Interface Sci.*, **248** (2017) 85.
13. E. P. Ivanova, J. Hasan, H. K. Webb, G. Gervinskas, S. Juodkazis, V. K. Truong, A. H. F. Wu, R. N. Lamb, V. A. Baulin, G. S. Watson, J. A. Watson, D. E. Mainwaring, and R. J. Crawford, *Nat. Commun.*, **4** (2013) 2838.
14. R. Jiang, Y. Yi, L. Hao, Y. Chen, L. Tian, H. Dou, J. Zhao, W. Ming, and L. Ren, *ACS Appl. Mater. Inter.*, **13** (2021) 60865.
15. E. Stratakis, J. Bonse, J. Heitz, J. S iegel, G. D. Tsibidis, E. Skoulas, A. Papadopoulos, A. Mimidis, A.-C.Joel, P. Comanns, J. Krüger, C. Florian, Y. Fuentes-Edfuf, J. Solis, and W. Baumgartner, *Mater. Sci. Eng. R Rep.*, **141** (2020) 100562.
16. N. Rawat, M. Benčina, E. Gongadze, I. Junkar, and A. Iglič, *ACS Omega*, **7** (2022) 47070.
17. D. Chopra, K. Gulati, and S. Ivanovski, *Materials Today Advances*, **12** (2021) 100176.
18. R. Bright, D. Fernandes, J. Wood, D. Palms, A. Burzava, N. Ninan, T. Brown, D. Barker, and K. Vasilev, *Materials Today Bio*, **13** (2022) 100176.
19. M. N. Dickson, E. I. Liang, L. A. Rodriguez, N. Vollereaux, and A. F. Yee, *Biointerphases*, **10** (2015) 021010.
20. K. Modaresifar, S. Azizian, M. Ganjian, L. E. Fratila-Apachitei, and A. A. Zadpoor, *Acta Biomater.*, **83** (2019) 29.
21. S. Miura, R. Yamagishi, R. Miyazaki, K. Yasuda, Y. Kawano, Y. Yokoyama, N. Sugino, T. Kameda, and S. Takei, *Gels*, **8** (2022) 785.
22. S. Murayama, I. Motono, K. Mizui, K. Kondoh, M. Hanabata, and S. Takei, *J. Nanomater.*, **5180460** (2019).
23. S. Takei, *Macromol Mater Eng.*, **305** (2020) 1900853.
24. J. C. Vasco and A. S. Pouzada, *Int. J. Adv. Manuf. Technol.*, **69** (2013) 2293.
25. S. Zhou, X. Lei, J. Mei, A. N. Hrymak, M. R. Kamal, and H. Zou, *J. Appl. Polym. Sci.*, **138** (2021) 49817.

26. C. Yang, X. H. Yin, and G. M. Cheng, *J Micromech Microeng.*, **23** (2013) 093001.

27. C. Weng, Q. Tang, J. Li, L. Nie, and Z. Zhai, *Nanomaterials*, **12** (2022) 1751.

28. B. Nowduri, A. Britz-Grell, M. Saumer, and D. Decker, *Nanotechnology*, **34** (2023) 165301.

29. M. Muehlberger, *Nanomanufacturing*, **2** (2022) 17.

30. R. B. Figueira, *In Handbook of Greener Synthesis of Nanomaterials and Compounds*, **Elsevier** (2021) 459.

31. Y. B. Makarychev, N. A. Gladkikh, G. V. Redkina, O. Y. Grafov, A. D. Aliev, and Y. I. Kuznetsov, *Materials*, **15** (2022) 2418.

32. R. Yamagishi, S. Miura, K. Yasuda, N. Sugino, T. Kameda, Y. Kawano, Y. Yokoyama, and S. Takei, *Appl. Phys. Express*, **15** (2022) 046502.

33. S. Sarafan, P. Wanjara, J. Gholipour, F. Bernier, M. Osman, F. Sikan, M. Molavi-Zarandi, J. Soost, and M. Brochu, *J. Manuf. Mater. Process.*, **5** (2021) 107.

34. K. L. M. Avegnon, D. C. Schmitter, S. Meisman, H. Hadidi, B. Vieille, and M. P. Sealy, *Procedia CIRP*, **108** (2022) 704.

35. D. P. Linklater, V. A. Baulin, S. Juodkazis, R. J. Crawford, P. Stoodley, and E. P. Ivanova, *Nat. Rev. Microbiol.*, **19** (2021) 8.

36. M. Kelly, K. Macdougall, O. Olabisi, and N. McGuire, *International urogynecology journal*, **28** (2017) 171.

Soft Motion of Dielectric Driven Balloon Actuator

Yoshinobu Nishira, Kosei Ito, and Fujio Tsumori*

*Department of Aeronautics and Astronautics, Kyushu University,
744 Motooka, Nishi-ku, Fukuoka 819-0395, Japan
tsumori @aero.kyushu-u.ac.jp

This study presents the development of a balloon-type dielectric elastomer actuator (DEA) that utilizes the Maxwell stress generated by applying voltage between electrodes. DEAs have been recognized for their superior responsiveness, durability, and energy efficiency, making them a promising candidate for applications such as artificial muscles. We fabricated two types of DEA using a latex balloon as the elastic material and carbon grease as the electrode to generate inflating and squashed deformations. We conducted experiments to measure and analyze the two types of deformation while varying the size or inner pressure of the balloon and the voltage magnitude. We found that the voltage magnitude affected the magnitude of the deformation in the actuator with inflating deformation, but not in the actuator with squashed deformation. Additionally, we estimated the applied Maxwell stress in the actuator. The developed actuators were capable of producing movements that imitate the behavior of organisms, such as the pufferfish.
Key words: Soft actuator, DEA, Balloon, Maxwell stress

1. Introduction

Soft actuators have gained significant attention due to their flexibility and ability to generate a variety of movements such as crawling [1, 2], jumping [1, 3], grasping [3, 4], and bending [5]. Compared to conventional rigid actuators, soft actuators can move delicately, resulting in low noise levels and high adaptability to the surrounding environment. With their lightweight and soft bodies, soft actuators are expected to find applications in the medical and aerospace fields. They can be driven by various inputs, including pneumatic [2, 4, 5], magnetic [6-15], thermal [16, 17], and electrical [18-31] methods. In this study, we focus on electrically-driven soft actuators and have developed dielectric elastomer actuators (DEAs) due to their superior responsibility, durability, and energy efficiency [29].

DEAs are typically composed of a thin film possessing dielectric properties, sandwiched between two deformable electrodes as shown in Fig. 1. When a high voltage is applied between the electrodes, the resulting attractive force, known as the Maxwell stress, causes the dielectric film to deform elastically, becoming thinner while extending in the planar direction.
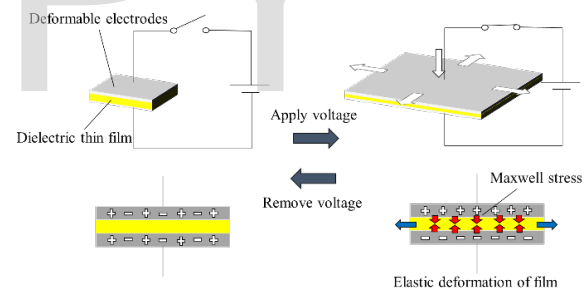
Fig. 1. Principle of DEA operation

In this study, we experimentally analyze the deformation of a balloon-type DEA. While previous studies have developed DEAs generating bending [25] and stretching [26] deformations, our actuator produces inflating and squashed deformations using natural rubber latex balloons as the material. The actuators are fabricated by placing an electrode inside a latex balloon and subsequently inflating it. We measure the resulting deformations when a high voltage is applied, and estimate the applied Maxwell stress to the actuator based on the results.

2. Developed Balloon-type DEA

This section describes the materials and methods used to fabricate and actuate the balloon type DEA.

The actuator was fabricated using a latex balloon made from natural rubber (Pioneer Balloon) and antistatic grease (Sunhayato, GE-L201) as the electrode. High voltages were applied to the actuators using an AC/DC high voltage generator (Advanced Energy Industries, TREK 610E).

Two types of actuators were fabricated in this study: inflated and squashed. To fabricate the actuator with inflating deformation, carbon grease was applied to the inside and outside of a latex balloon that was then inflated as shown in Fig. 2. For the actuator with squashed deformation, the carbon grease was coated only inside the balloon, and the balloon was placed on a metal substrate and connected to a high voltage generator. Schematic setups of the both actuators are shown in Figs. 3 and 4, respectively. In both cases, the Maxwell stress between the carbon grease inside and outside the balloon resulted in the desired deformation.

To measure the deformation, we varied the size

Fig. 2. Actuator creation process
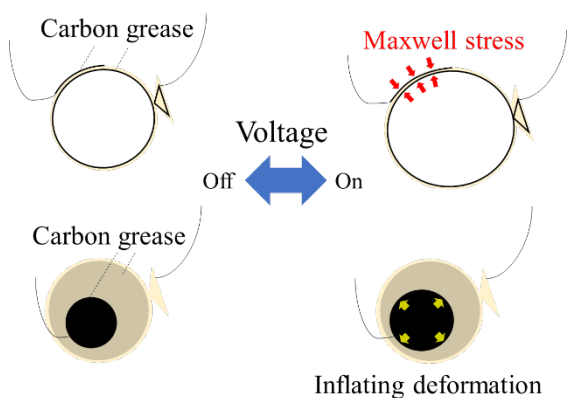
Fig. 3. Structure of the actuator with inflating deformation
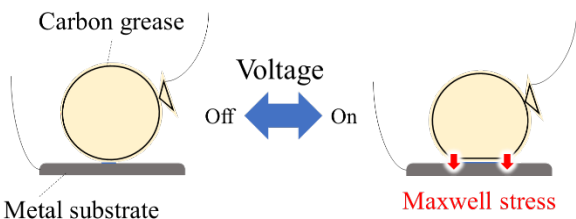
Fig. 4. Structure of the actuator with squashed deformation

(or inner pressure) of the balloon and the magnitude of the voltage applied to the actuator. The measurements and analyses of the deformation were performed using a video. The video images were processed by an image processing software (ImageJ) and a markerless pose estimation software based on a machine learning system with deep neural networks (DeepLabCut). The Maxwell stress applied to the actuator was estimated based on the deformation results and discussed in the following section.

3. Experiment
3.1. Actuator with inflating deformation

The actuator with inflating deformation was operated at different voltages while varying the diameter of the balloons. The actuated balloons are shown in Figure 5. The voltage range applied was from 0 to 5 kV. Once the voltage was initiated, the carbon grease on the surface of the actuator expanded in area, resulting in a noticeable deformation that increased slightly as the voltage was increased. The relationship between the deformation and the voltage is shown in Fig. 6. As the voltage increased, the Maxwell stress also increased, resulting in a corresponding increase in the deformation. At high voltages, the actuator sometimes experienced a dielectric breakdown as the short diameter decreased. This breakdown could be attributed to the Maxwell stress further thinning the dielectric film, which was already reduced due
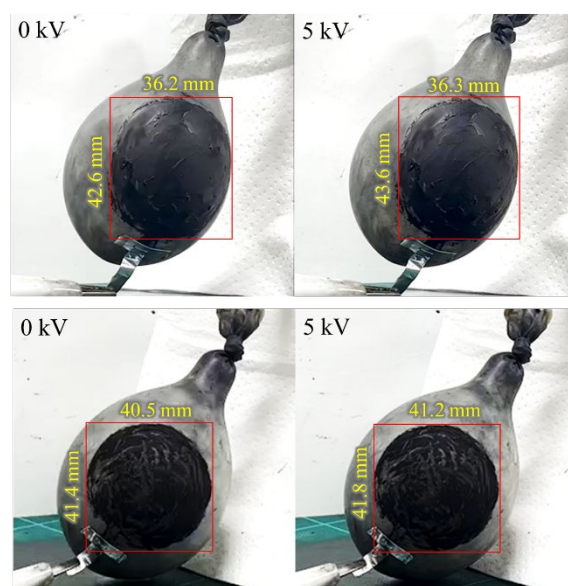
Fig. 5. Deformation of the actuator with inflating deformation. The diameter of the balloon was 50 mm (upper), and 55 mm (lower)
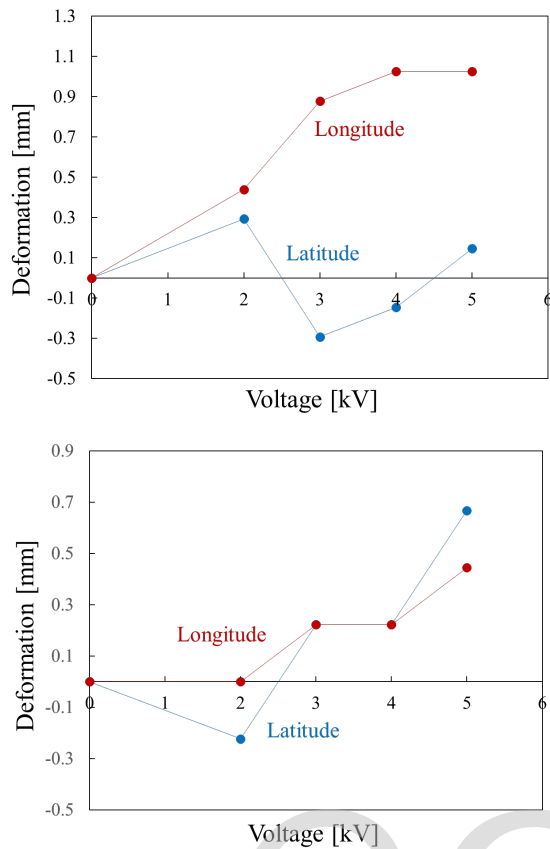
Fig. 6. Deformation of the actuators. The diameter of the balloon was 50 mm (upper), and 55 mm (lower)

to the balloon's enlargement. meter of the balloon increased due to the occurrence of electrical breakdown. This dielectric breakdown can be considered to have been caused by the Maxwell stress further thinning the film thickness, which was reduced by the balloon's enlargement.

3.2. Actuator with squashed deformation
3.2.1. Characteristics of balloons

Prior to performing the experiment of the actuator with squashed deformation, we conducted an experiment to measure the deformation properties of the latex balloons. This experiment involved applying a vertical force to a balloon placed on an electrical balance and measuring the load. The deformation was measured for each internal pressure of the balloon, and the results are shown in Fig. 7. As shown, the deformation decreases as the internal pressure of the balloon increases.

When a vertical load is applied to a balloon, the force F is given by the following equation:

$$F = \frac{\pi D^2}{4} \Delta p \qquad (1)$$

where D is the contact diameter, and Δp is the
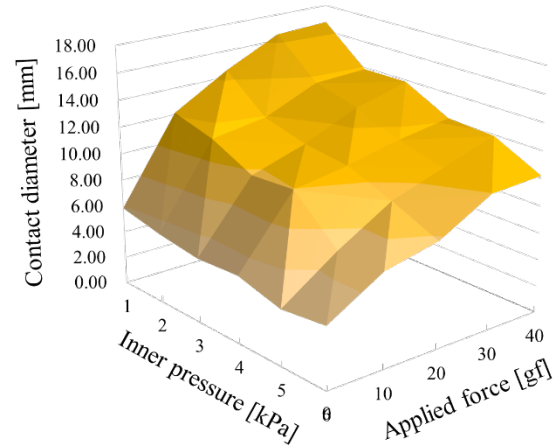
Fig. 7. Change of contact diameter of the balloon on the substrate

pressure difference between inside and outside of a balloon. The relationship between the vertical force to a balloon and the contact diameter determined this theoretical equation, and qualitatively similar as the experimental results.

3.2.2. Deformation measurement

The results of applying voltages of 0-5 kV while varying the internal pressure of the balloon are shown in Fig. 8. The measured contact diameter between the metal substrate and the balloon for each case is shown in Fig. 9. The deformation was smaller at 1 kV. The deformation would not reach the peak value because the Maxwell stress was too small. For voltages of 2 kV and above, there was little difference in the size of the deformation due to voltage, indicating that the deformation of this actuator was independent of the applied voltage. The reason for the lack of deformation at an internal pressure of 6 kPa would be due to nonlinear deformation of the natural rubber. The rubber would be stiffer just before reaching an internal pressure of 6 kPa.

The contact diameter results obtained and the perpendicular force applied when a voltage is applied were estimated using equation (1). Figure 10 shows the case of the applied voltage of 5 kV. The vertical force was decreasing where the internal pressure of the balloon exceeds 4 kV. This is considered to be due to the nonlinearity of rubber elasticity.

4. Conclusion

We produced balloon type DEA that cause inflating and squashed deformation. We created two types of actuators that differed in the inner pressure
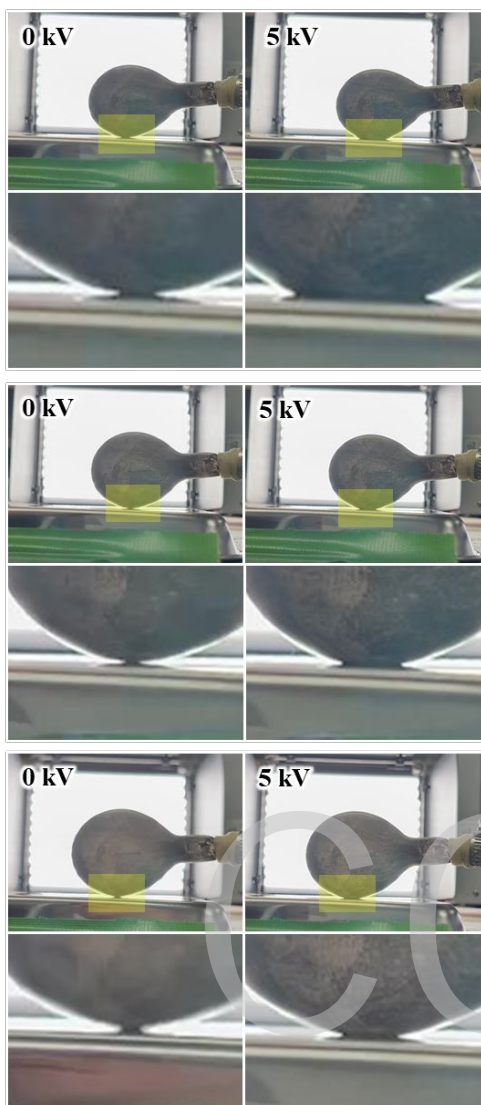
Fig. 8. Deformation of the actuator with squashed deformation. Inner pressure 1 kPa (upper), 3 kPa (center), and 5 kPa (lower).
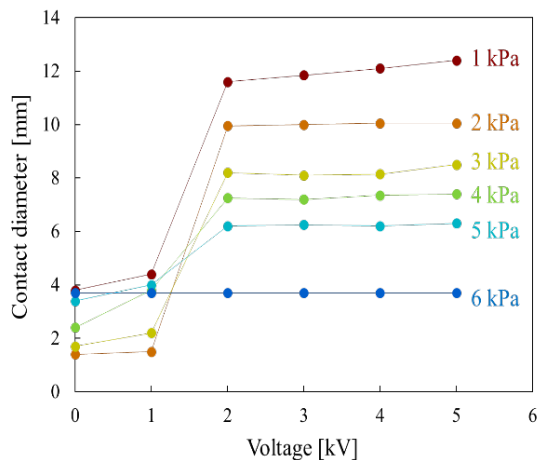
Fig. 9. The result of applying voltage to the actuator with squashed deformation
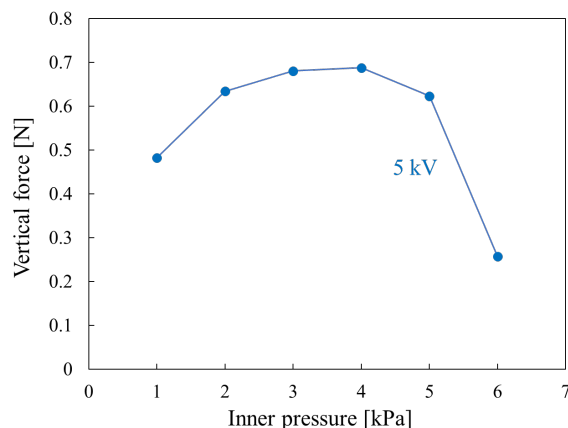
Fig. 10. Maxwell stress estimates

of the balloon and applied voltage, and we measured the deformation for each type. In the actuator with inflating deformations, we observed a slight variation in the amount of deformation with increasing voltage. For the actuator with squashed deformation, we noted a negligible difference in deformation magnitude despite applying varying voltage levels. Also, the value of Maxwell stress could be estimated by comparing the deformation when a vertical load was applied with that when a voltage was applied. These actuators could produce movements that mimic organisms such as pufferfish.

Acknowledgements

References

1. W. Huang, W. Shang, Y. Huang, H. Long, and X. Wu, *IEEE Robot. Autom. Lett.*, **7** (2022) 9287.
2. R. F. Shepherd, F. Ilievski, W. Choi, S. A. Morin, A. A. Stokes, A. D. Mazzeo, X. Chen, M. Wang, and G. M. Whitesides, *Proc. Natl. Acad. Sci. U S A,* **108** (2011) 20400.
3. C. Tawk, R. Mutlu, and G. Alici, *Front. Robot. AI*, **8** (2022) 799230.
4. R. Deimel and O. Brock, *IEEE Int. Conf. Robot. Autom.,* (2013) 2047.
5. H. M. Elmoughni, A. F. Yilmaz, K. Ozlem, F. Khalilbayli, L. Cappello, A. T. Atalay, G. Ince, and O. Atalay, *Actuators*, **10** (2021) 3390.
6. W. Zhang, Y. D. J. Zhao, T. Zhang, X, Zhang, W. Song, L. Wang, and T. Li, *Small*, (2023)
7. Z. Wu, Q. Wang, J. Huang, Y. Yue, D. Chen, Y. Shi, and B. Su, *Compos. Sci. Technol.*, **217** (2022) 109129.
8. F. Tsumori, A. Saijou, T. Osada, and H. Miura, *Jpn J Appl Phys*, **54** (2015) 6.

9. H. Shinoda, S. Azukizawa, K. Maeda, and F. Tsumori, *J. Electrochem. Soc.*, **166** (2019) B3235.

10. F. Tsumori, R. Marume, A. Saijou, K. Kudo, T. Osada, and H. Miura, *Jpn. J. Appl. Phys.*, **55** (2016) 06GP19.

11. R. Marume, F. Tsumori, K. Kudo, T. Osada, and K. Shinagawa, *Jpn. J. Appl. Phys.,* **56** (2017) 06GN15.

12. S. Azukizawa, H. Shinoda, K. Tokumaru, and F. Tsumori, *J. Photopolym. Sci. Technol.*, **31** (2018) 139.

13. F. Tsumori, N. Miyano, and H. Kotera, *J. Jpn. Soc. Powder Powder Metal.*, **56** (2009) 133.

14. F. Tsumori, H. Kawanishi, K. Kudo, T. Osada, and H. Miura, *Jpn. J. Appl. Phys.*, **55** (2016) 06GP18.

15. F. Tsumori and J. Brunne, in *Proceedings of the IEEE International Conference on Micro Electro Mechanical Systems (MEMS)* (2011).

16. T. H. Ware, M. E. McConney, J. J. Wie, V. P. Tondiglia, and T. J. White, "Voxelated liquid crystal elastomers," *Science*, **347** (2015) 982.

17. Y. Yang, Z. Pei, Z. Li, Y. Wei, and Y. Ji, *J. Am. Chem. Soc.*, **38** (2016) 2118.

18. T. G. La and G. K. Lau, *Appl. Phys. Lett.*, **102** (2013) 192905.

19. J. Ashby, S. Rosset, E. F. M. Henke, and I. A. Anderson, *Front. Robot. AI*, **8** (2022) 792831.

20. P. White, S. Latscha, and M. Yim, *Actuators*, **3** (2014) 245.

21. Y. Liu, B. Liu, T. Yin, Y. Xiang, H. Zhou, and S. Qu, *Smart Mater Struct*, **29** (2020) 15008.

22. D. Gonzalez, J. Garcia, and B. Newell, *Sens. Actuator A Phys.*, **297** (2019) 111565.

23. J. Bernat and J. Kołota, *Energies,* **14** (2021) 5633.

24. A. Wiranata, Y. Ishii, N. Hosoya, and S. Maeda, *Adv Eng Mater*, **23** (2021) 2001181.

25. F. A. Mohd Ghazali, C. K. Mah, A. AbuZaiter, P. S. Chee, and M. S. Mohamed Ali, "Soft dielectric elastomer actuator micropump," *Sens. Actuators A Phys.*, **263** (2017) 276.

26. Y. Zhu N. Liu, Z. Chen, H. He, Z. Wang, Z. Gu, Y. Chen, J. Mao, Y. Luo, and Y. He, *ACS Mater. Lett.*, **5** (2023) 704.

27. M. Molberg, Y. Leterrier, C. J. G. Plummer, C. Walder, C. Lowe, D. M. Opris, F. A. Nuesch, S. Bauer, and J. A. E. Manson, *J. Appl. Phys.*, **106** (2009) 054112.

28. R. Pelrine, R. Kornbluh, Q. Pei, and J. Joseph, "High-speed electrically actuated elastomers with strain greater than 100%," *Science*, **287** (2000) 836.

29. N. Koike and T. Hayakawa, *ROBOMECH J.*, **8** (2021) 2055.

30. H. Zhao, A. M. Hussain, M. Duduta, D. M. Vogt, R. J. Wood, and D. R. Clarke, "Compact Dielectric Elastomer Linear Actuators," *Adv. Funct. Mater.*, **28** (2018) 1804328.

31. J. Shintake, V. Cacucciolo, H. Shea, and D. Floreano, *Soft Robot.*, **5** (2018) 46.

Amylopectin-based Eco-friendly Photoresist Material in Water-developable Lithography Processes for Surface Micropatterns on Polymer Substrates

Yuna Hachikubo[1], Sayaka Miura[1], Rio Yamagishi[1], Mano Ando[1], Makoto Kobayashi[2], Takayuki Ota[2], Toru Amano[2], and Satoshi Takei[1*]

[1]*Department of Pharmaceutical Engineering, Toyama Prefectural University, Imizu, Toyama 939-0398, Japan*

[2] *Gunei Chemical Industry, Takasaki, Gunma 370-0032, Japan*

*takeis@pu-toyama.ac.jp

Photoresist materials are also used in semiconductor manufacturing and have excellent properties for fine processing. In recent years, lithography technology has enabled microscopic processing. Among them, photoresist materials, which are also used in semiconductor manufacturing, are attracting attention for their potential to contribute to the development of biosensors, bioelectronics, and biotechnology in the life science field. However, photoresist materials use organic compounds in the casting solvent and developing solution, which raises concerns about environmental protection and health and safety. Therefore, it has been difficult to apply them to the life science field. In this study, we used amylose and amylopectin sugar chains to create a photoresist material that can be developed in water without using organic compounds. This material is characterized by its ability to be applied and developed with water and processed without the use of organic compounds. The photoresist patterns were fabricated and surface shapes were observed, achieving a fine fabrication of approximately 8 μm.

Keywords: Photoresist, Water-developable lithography, Water soluble polymer, Bio-electronics, Biomedical application

1. Introduction

In recent years, demand for semiconductors has increased and computer chip components such as logic and memory have continued to shrink in size. This miniaturization has been made possible by the development of lithography technology [1,2]. Photoresist materials, also used in semiconductor manufacturing, are essential for lithography and are becoming increasingly miniaturized [3]. Current resist materials use organic compounds as casting solvents and on occasion as developers. Therefore, the use of organic solvents in the lithography process is a concern from the standpoint of environmental conservation. In addition, the disposal of organic solvents is a factor that increases costs for semiconductor device manufacturers and other

companies that use photoresist materials [4]. A typical organic formulation consists of about 70 wt% organic solvent. This organic solvent has adverse effects on the human body and the environment when handling resist formulations. For example, during the coating and baking processes, the organic solvent evaporates and most of it is released into the atmosphere. In addition, the edge bead removal and backside cleaning processes use more organic solvents than the organic solvents in the resist formulation, resulting in a large amount of organic waste. For these reasons, health hazards, environmental impact, and waste disposal costs must be considered when using resist formulations [5].

There are two possible ways to minimize the environmental impact of organic solvents in resist

processing. The first method is to deposit a resist film on the substrate from the vapor or solid phase and dry develop it to completely remove the cast solvent [6]. The other is to replace the developing solution with water [5].

Out of the two methods, our laboratory is working for replacing organic solvent with water. The lithography processes include developing with organic solvents or water. In conventional lithography, resist materials are immersed in an alkaline developing solution of trimethylphenylammonium hydroxide (TMAH) [4] dissolved in pure water. Other methods include the use of organic solvents such as cyclohexanone and 2-heptanone.

Replacing developing solution with water could contribute to the development of biosensors [7,8], bioelectronics [9], and biotechnology [10,11]. It is also an effective alternative to alkaline developers, organic solvents, and solvents that pose significant safety, health, and environmental concerns [12]. Water-soluble photoresist materials reported to date include those using poly (vinyl alcohol) [13], polyvinylpyrrolidone [14], and water-soluble polymer materials containing pendant sugars [15]. There are negative [16] and positive [17, 18] types of resist, and we used the negative type, which cross-links where it is exposed to light and becomes insoluble in water.

In our previous studies, this photosensitive material was made by modifying the hydroxyl group of each dextrin with acrylate, a photosensitive group, while maintaining water solubility. This material was applied by spin-coating [19] on a silicon wafer, exposed with a mask contact exposure system, and developed with water to evaluate sensitivity, etching resistance, and coating strength. In the microfabrication evaluation, it was found that the performance varied depending on the bonding mode. Furthermore, it was shown that indigestible dextrin can function as a water-soluble micro-patterning material. Since it does not require organic solvents or highly toxic strong alkaline developer, it is effective as a patterning material with low environmental impact [20].

This paper describes new water-soluble resist materials, amylopectin-based eco-friendly photoresist material, which is a mixture of amylose-based and amylopectin-based photosensitive polymers as a water-soluble resist. Hereafter, amylopectin-based eco-friendly photoresist will be abbreviated as amylopectin resists.

2. Experimental

2.1. Amylopectin resist materials

Amylopectin resist materials that can be applied with water and developed with water were prepared. Scheme 1 shows the chemical reaction equation for amylopectin resists. (e) The amylopectin resist polymers with UV-sensitive acrylic groups were formed through the reaction of 50 mol% (a) 2-isocyanatoethyl acrylate (Resonac) and 50 mol% (b) 1,1- (bisacryloyloxymethyl) ethyl isocyanate (Resonac) with the hydroxyl group of (c) amylose and (d) amylopectin.

The reacted amylopectin polymers with UV-sensitive acrylic groups as shown in (e) had the weight-average molecular weight of 36000, and the range of polydispersity was 2.9 related to the standard polystyrene, in terms of the gel permeation chromatography (GPC) conditions described below.

The weight average molecular weight and polydisperse range were determined using a GPC system (HLC-8320GPC EcoSEC, Tosoh). Three separation columns of SuperAW3000 (TSK-GEL, Tosoh) and double-serially linked SuperAW-H (TSK-GEL, Tosoh) were used, and *N,N*-dimethylformamide was selected. The column temperature was maintained at 40 ºC. The solvent flow rate was set at 0.6 ml/min. The solution was filtered through an ultrahigh-molecular-weight membrane filter with an average pore size of 250 nm (Whatman Lab). Thereafter the weight average molecular weight and polydispersity range were measured.

2.2. Film thickness of amylopectin resist materials

A spin-coating and developing system (CLEAN TRACK ACT 8,Tokyo Electron) was used to evaluate the thickness uniformity of the spin-coated amylopectin resist materials.

The aqueous solution of amylopectin resist materials on an 8-inch silicon wafer spin-coated with underlayer material that complements the plasma etching resistance (transfer characteristics to the substrate to be processed) of negative water developable resist materials for lithography. The spin-coated conditions were 1500 rpm for 60 s following spin coating at 500 rpm for 15 s on the Si wafer after pre-wet process at 1000 rpm for 15 s by pure water to improve the surface roughness, thickness uniformity, and coating defect of amylopectin resist materials.

(a)

(b)

(c)

(d)

(e)
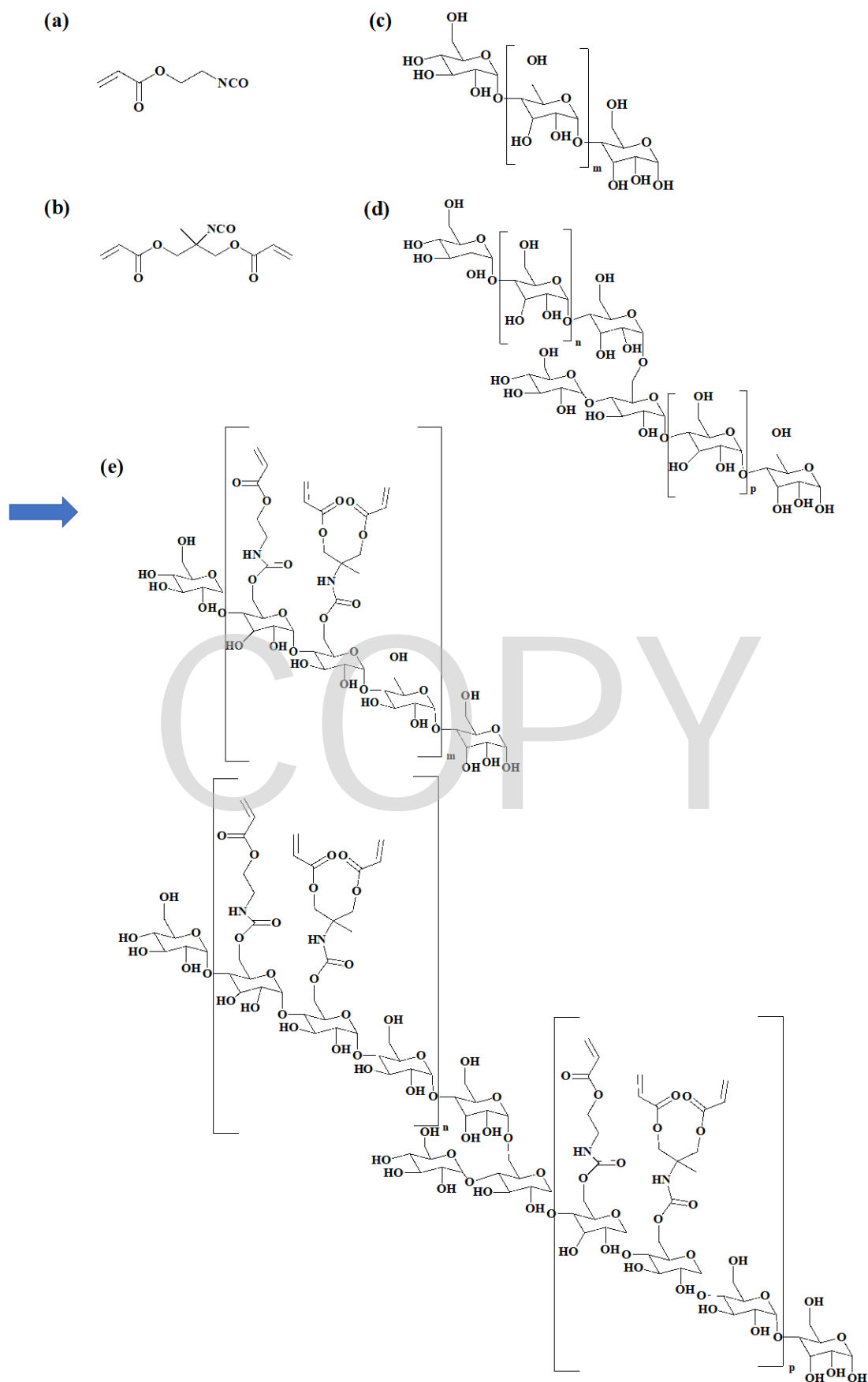
Scheme 1.   Chemical reaction equation for amylopectin resists**:** (a) 2-isocyanatoethyl acrylate, (b) 1,1- (bisacryloyloxymethyl) ethyl isocyanate, (c) amylose, (d) amylopectin, and (e) amylopectin resist polymers.

2.3. Changes in the structure of amylopectin resist materials

The structural changes of the synthesized water-soluble resist materials before and after UV cross-linking by UV were confirmed using an attenuated total reflection Fourier transform infrared spectroscopy (ATR-FTIR) of the infrared absorption spectrum (FT-IR). The measurements were performed using an FT-IR (Spectrum Two: Perkin Elmer).

In order to measure the thickness of the film, the film was thickened by the casting method, and two types of UV irradiation were made: one with 17 J/cm^2 exposure and the other without exposure. In order to normalize the infrared spectra obtained, we used the 1714 cm^{-1} band, assigned to ester.
The frequency range was set to 1600-1680 cm^{-1} in order to compare non-covalent alkenes (vinyl groups) at 1634 cm^{-1} before and after UV irradiation.

2.4. Exposure sensitivity

The sensitivity of the amylopectin resist was confirmed by measuring the thickness of the amylopectin resist film with varying intensity of UV irradiation, respectively. Aqueous solution of amylopectin resist materials was dropped onto hydrophobic surface-treated silicon wafers and spin-coated. The spin-coated conditions were 2500 rpm for 60 s following spin coating at 300 rpm for 10 s. The resist film thickness of the amylopectin resist materials was measured in advance using a non-contact thin-film measurement system (F20-UV, Fimetrics). Then 10 samples were prepared by varying the exposure dose from 0-160 mJ/cm^2 and dissolved in aqueous solution without alkali development (27°C, 60 s). Again, the resist film thickness of the amylopectin resist materials was measured and the non-dissolving resist film thickness was calculated.

2.5. Preparation of water developable amylopectin resists

The substrate was treated to improve hydrophilicity, which is considered to enable microfabrication, and the effect of the treatment was confirmed by measuring the contact angle between the substrate and water. Micro-patterns were fabricated on the substrate with amylopectin resist and observed. The plastic polystyrene slide substrates (Kenis, Japan) were hydrophilically treated for 2 min using UV ozone treatment equipment (LT0Z-180, Litho Tech Japan), to improve the adhesion between the amylopectin resist materials and the plastic polystyrene slide substrates. Then 200 µL of aqueous solution of amylopectin resist materials were measured with a pipettor and dropped.

The substrate was spin-coated (10 s at 0 rpm, 5 s at 500 rpm, and 25 s at 1500 rpm) and then baked for 30 s on a hot plate at 75°C. UV irradiation was performed with an exposure of 590 mJ/cm^2 followed by 1 min development in water at 25°C.

Figure 1 presented the water- developable lithography processes using amylopectin resist materials. The contact angle for water on the 4 types of substrates was measured using a dynamic contact angle meter (DropMaster500Z, Kyowa Interface Science) to evaluate the film's water repellency. The contact angle for water was calculated using the θ/2 analysis method. The measurement time after dropping was 1.0 s. The four substrates are untreated plastic, untreated glass, ozone-treated plastic and ozone-treated glass substrates.
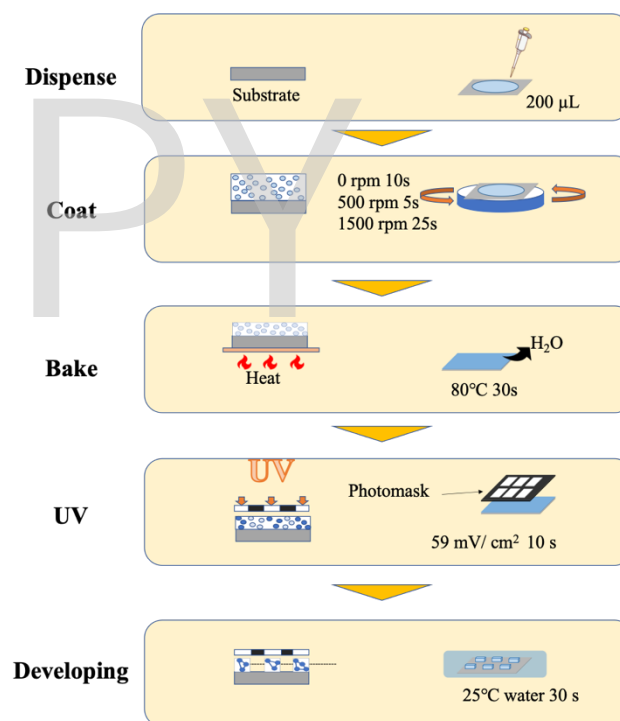
Fig. 1. Water- developable lithography processes.

3. Results and discussion

3.1. Film thickness uniformity

The thickness of the film of amylopectin resist materials without organic solvents was measured and the results are shown in Fig. 2. There is a correlation between the number of spin-coating rotations and film thickness uniformity, which is affected by the viscosity of the resist solution. In the case of amylopectin resist materials, spin coating conditions

with a main rotation speed of 2500 rpm or more were found to be preferable for obtaining good in-plane uniformity of application. From the results in Fig. 2, the average thickness of the resist was measured to be 165 nm ± 7 nm thickness uniformity.

Amano et al. reported the following results. Spin-coating of water-soluble resist materials generated from dextrin manufactured by San-ei Sucrochemical was performed to check uniformity, and a flat film of ±10 nm was formed with a rotation speed of more than 2000 rpm. This variation in film thickness is thought to be due to wetting of the silicon wafer by the moisture coating [3]. The above shows that the amylopectin resist materials have a better uniformity, as the result of ±7 nm is obtained.

In addition, Bajpai et al. found that spin-coating of existing photoresist materials under optimized conditions resulted in a film thickness of 2.17 ± 0.0332 μm [21]. In other words, amylopectin resist materials have a larger variation in average thickness from place to place compared to existing photoresist materials. However, when compared by thickness alone, the amylopectin resist materials have smaller fluctuations in value and is considered less problematic for patterning.
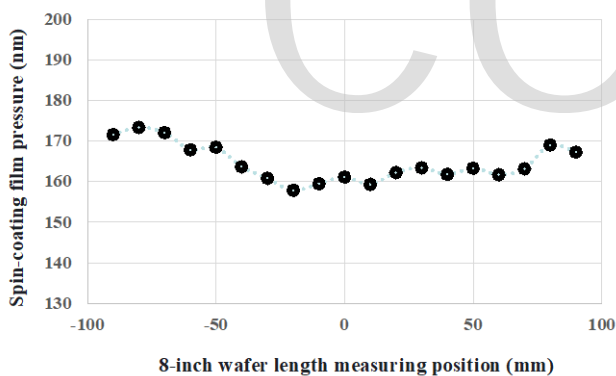
Fig. 2.   Film thickness uniformity of amylopectin resist materials.

3.2. FT-IR spectroscopic analysis

The FT-IR spectra before and after light irradiation are shown in Fig. 3. Scheme 2 suggests that the double bonds in (c) amylose and (d) amylopectin are broken and (a) 2-isocyanatoethyl acrylate and (b)1,1-(bisacryloyloxymethyl) ethyl isocyanate are joined, so the absorption at 1634 cm^{-1} of the vinyl group was compared before and after light irradiation. In the present reaction, the double bond reacts and the bond is broken, so the non-covalent alkene spectrum (1634 cm-^{1}) is reduced. This result suggests that the

vinyl groups of the material may be polymerized by light. The reason why the double bond does not become 0 is thought to be because of the effect of steric hindrance, and therefore, the reaction was not complete even when the light was applied.   In other words,   Fig. 3   suggested that the vinyl groups of the material may have been polymerized by light, and the polymerization was confirmed to cause the film to become thicker as it was no longer soluble in the aqueous solution.
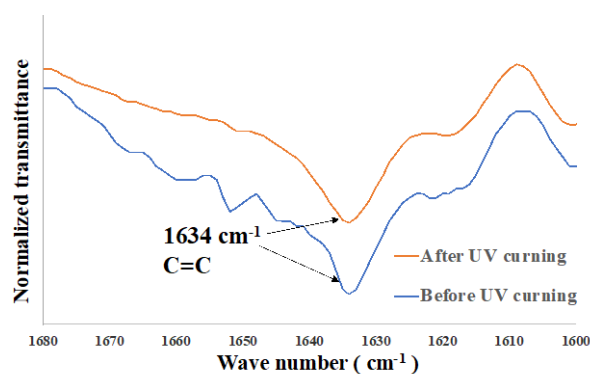
Fig. 3.   FT-IR spectroscopy of amylopectin resist materials.

3.3. Sensitivity curve

Figure 4 shows the sensitivity curve of amylopectin resist materials without organic solvents.   There is little change in film thickness when exposure is up to 60 mJ/cm^2, and it increases sharply from 60 to 120 mJ/cm^2. After 120 mJ/cm^2, it can be seen that the film thickness does not change even if exposure is continued. In other words, at 120 mJ/cm^2, almost all reaction points are considered to have reacted.
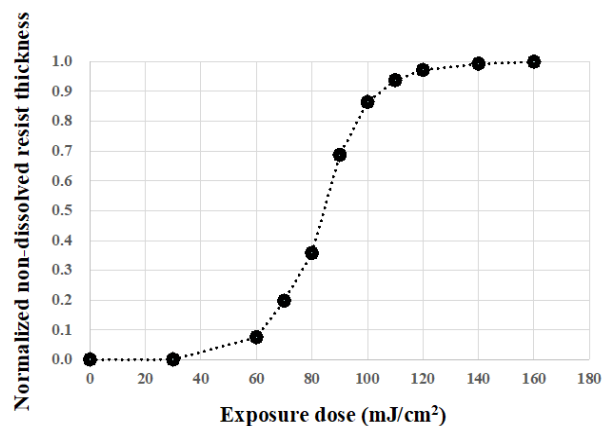
Fig. 4.   Sensitivity curve of amylopectin resist materials.

In a recent study, it was reported that water-soluble resist materials with cross-linking agents added to the main backbone, the dextrin require exposures of 900 mJ/ cm^2 or higher [22]. This material is considered less sensitive because the cross-linking agent chemically modified on the main backbone has only one acrylate group per molecule, resulting in a slow progression rate of the cross-linking reaction. Conversely, in the amylopectin resist materials used in this study, 1,1-(bisacryloyloxymethyl) ethyl isocyanate, chemically modified as the main frame, has two acrylate groups in one molecule, which is considered to have a faster cross-linking reaction, resulting in superior sensitivity.

3.4. Microfabrication results

Figure 4 shows that the reaction started at 30 mJ/cm^2 and that more than 95% of the reaction occurred at 120 mJ/cm^2. Since it was found that the reaction does not change at higher levels, the exposure was set at 590 mJ/cm^2 for this study.

The results of the observation of its surface topography are shown in Fig. 5 (a) is an oval pattern, (b$_1$) is a line pattern, (b$_2$) is an expanded image of (b$_1$), (c) is a polyline pattern, (d$_1$) is a square pattern, and (d$_2$) is an expanded image of (d$_1$). In the (a) oval pattern, the curves are nicely patterned, but the thinner the line is, the more the lines stick together, and microfabrication is not achieved. Similarly, (b) the finer the line pattern, the more lines are attached
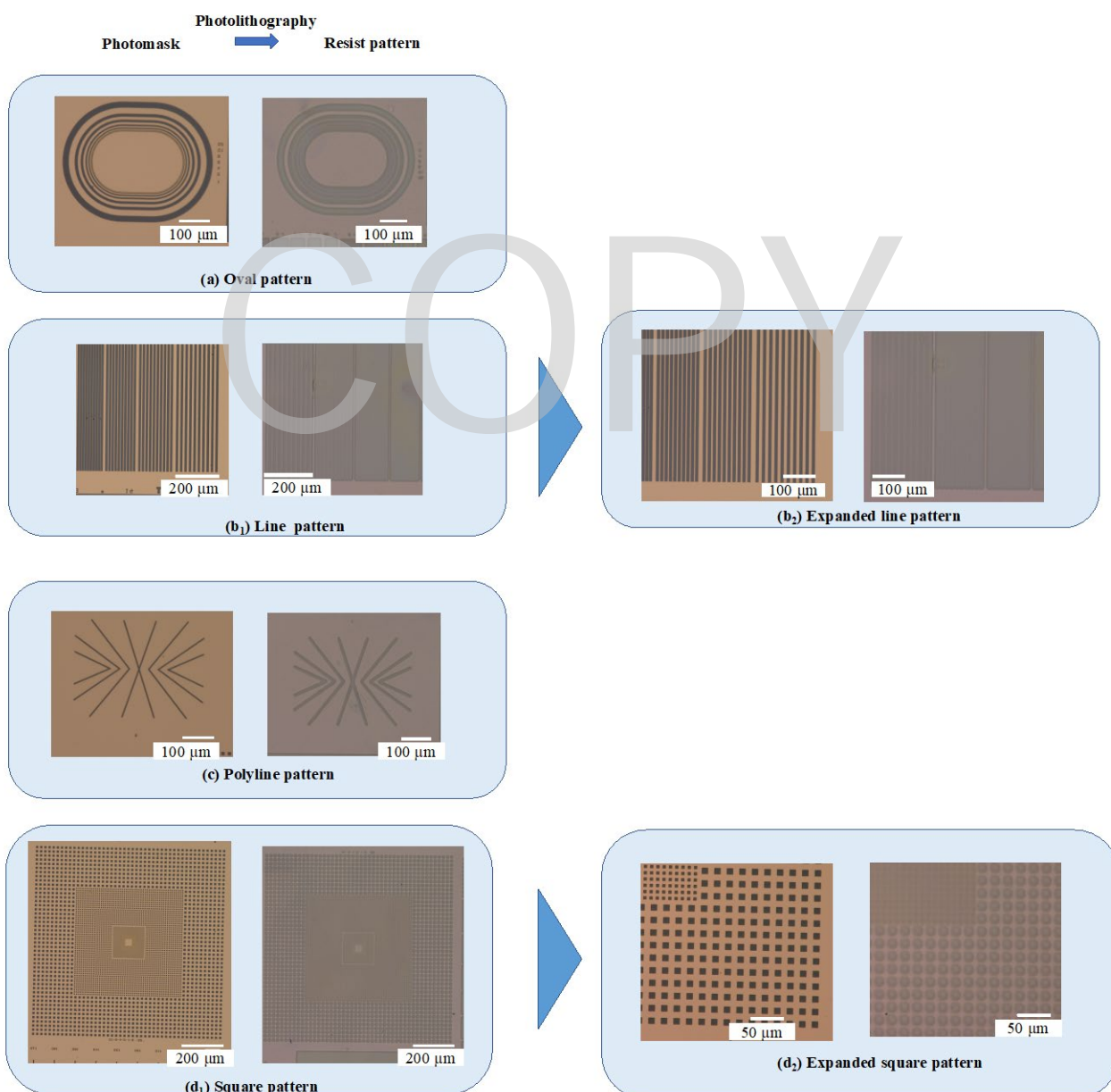
Fig. 5. Observation of surface topography of amylopectin resist materials: (a) oval pattern, (b$_1$) line pattern, (b$_2$) expanded image of (b$_1$), (c) polyline pattern, (d$_1$) square pattern, and (d$_2$) expanded image of (d$_1$).

to each other and not out of the middle. (c) polyline pattern shows the finest processing among (a)-(d). Compared with (b), the pattern with lines separated from each other can be processed more finely than the pattern with straight lines. The large dots on the outside of the (d) square pattern are also processed nicely, but there is a problem with the microfabrication because the dots are not coming off the inside when the spacing between them is narrower.

The results of microfabrication of water-soluble resists to date were compared. In the previous study, fremicrofabrication evaluation was performed with water-soluble resist materials containing cross-linking agents added to pullulan with acrylic acid-denatured polysaccharide chains and the dextrin [22]. The water-soluble resist materials with a cross-linking agent added to dextrin, which gave the best microfabrication results, was compared with the amylopectin resist materials. The water-soluble resist materials with cross-linking agents added to the dextrin were able to process about 10 μm. As can be seen from Fig. 5. (c), amylopectin resist materials were able to process approximately 8 μm. In essence, it can be said that amylopectin resist materials were capable of microfabrication.

Another possible reason for the good microfabrication results is the hydrophilic treatment to the plastic substrate. In this case, the hydrophilic treatment was performed by UV ozone surface treatment. Hydrophilic treatment of the substrate is believed to be effective in the material from sticking to the substrate when developing and preventing the pattern from flowing because the water-soluble resist materials is hydrophilic. The contact angles to water on four different substrates (untreated plastic, untreated glass, ozone-treated plastic and ozone-treated glass substrates) were measured, and the results are shown in the Fig. 6. The plastic substrate is more hydrophilic than the glass substrate, since the contact angle of water was much smaller for the plastic substrate after ozone treatment. For this reason, the experiment was conducted this time with ozone treatment on the surface of the plastic substrate. This may have made it more difficult for the pattern to peel off from the substrate and improved the developability, enabling microfabrication.
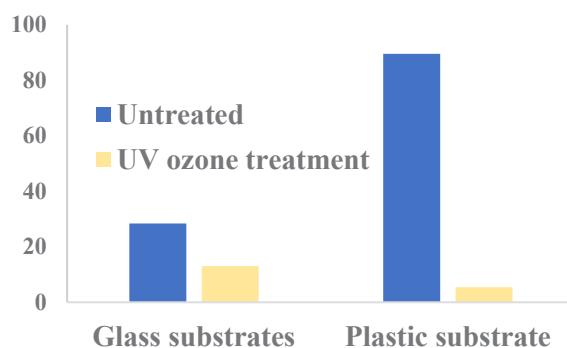
Fig. 6. Difference of water contact angle by substrate.

4. Conclusion

The effectiveness of water-soluble resist materials consisting of amylopectin resists without organic solvents for nanopatterning was investigated.

The amylopectin resists were prepared by converting the hydroxyl groups of amylose and amylopectin into photosensitive groups, and irradiated with 590 mJ/cm^2 and developed with water. It was found that this material can be microfabricated. The amylopectin material was available as resist materials that enables microfabrication and has a low environmental impact for alternative applications of biosensors, bioelectronics, and biotechnology in the life science field.

References

1. C. Luo, C. Xu, L. Lv, H. Li, X. Huang, and W. Liu, *RSC Adv.*, **10** (2020) 8385.
2. S. Okazaki, *Microelectron. Eng.*, **133** (2015) 23.
3. T. Amano, D. Hirata, Y. Hasegawa, and S. Takei, *J. Photopolym. Sci. Technol.*, **33** (2020) 445.
4. Y. Wang, Z. Zhang, C. Jiang, and T. Xu, *Ind.Eng. Chem. Res*, **52** (2013) 18356.
5. Q. Lin, T. Steinhäusler, L. Simpson, M.Wilder, D. R. Medeiros, C. G. Willson, J. Havard, and J. M. Fréchet, *Chem. Mater.*, **9** (1997) 1725.
6. A. Yoshikawa, O. Ochi, and Y. Mizushima, *Appl. Phys. Lett.*, **36** (1980) 107.
7. R. Bruch, A. Kling, G. A. Urban, and C. Dincer, *J. Visualized Exp.*, (2017).
8. B. Li, G. Pan, A. Suhail, K. Islam, N. Avent, and P. Davey, *Carbon*, **118** (2017) 43.
9. J. Ju, N. Hu, D. M. Cairns, H. Liu, and B. P. Timko, *Proc. Natl. Acad. Sci.,* **117** (2020) 15482.
10. A. Revzin, R. J. Russell, V. K. Yadavalli, W. G. Koh, C. Deister, D. D. Hile, B. B. Mellott, and M. V. Pishko, *Langmuir*, **17** (2001) 5440.
11. D. Falconnet, G. Csucs, H. M. Grandin, and M. Textor, *Biomaterials*, **27** (2006) 3044.
12. S. Takei, A. Oshima, T. Ichikawa, A. Sekiguchi, M. Kashiwakura, T. Kozawa, S. Tagawa, G. T. Oyama, S. Ito, and H. Miyasaka, *Microelectron. Eng.*, **122** (2014) 70.
13. J. M. Havard, S. Y. Shim, J. M. Fréchet, Q. Lin, D. R. Medeiros, C. G. Willson, and J. D. Byers, *Chem. Mater.*, **11** (1999) 719.
14. J. Swei, and J. B. Talbot, *J. Appl. Polym. Sci.*, **102** (2006) 1637.
15. J. M. Havard, N. Vladimirov, J. M. Fréchet, S. Yamada, C. G. Willson, and J. D. Byers, *Macromolecules*, **32** (1999) 86.
16. J. H. Pai, Y. Wang, G. T. A. Salazar, C. E. Sims, M. Bachman, G. P. Li, and N. L. Allbritton, *Anal. Chem.*, **79** (2007) 8774.
17. C. A. Mack, *J. Electrochem. Soc.*, **134** (1987) 148.
18. D. N. Khanna, and W. H. Mueller, *SPE Transactions*, **29** (1989) 954.
19. Q. Liu, Y. Yan, L. Meng, Z. Zhang, and Zhou, P., *Coatings*, **12** (2022) 1253.
20. T. Amano, M. Kobayasi, and S. Takei, *J. Photopolym. Sci. Technol.,* **34** (2021) 187.
21. A. Bajpai, K. Rangra, and D. Bansal, *J. Electron. Mater.*, **50** (2021) 7143.
22. T. Amano, M. Kobayasi, and S. Takei, *J. Photopolym. Sci. Technol.,* **34** (2021) 181.

JOURNAL OF PHOTOPOLYMER SCIENCE AND TECHNOLOGY